ACCURACY ASSESSMENT OF PHOTOGRAMMETRIC DIGITAL ELEVATION MODELS GENERATED FOR THE SCHULTZ FIRE BURN AREA

By Danna K. Muise

A Thesis

Submitted in Partial Fulfillment

of the Requirements for the degree of

Master of Science

in Applied Geospatial Sciences

Northern Arizona University

August 2014

Approved:

Erik Schiefer, Ph.D., Chair

Ruihong Huang, Ph.D.

Mark Manone, M.A.

Abstract

ACCURACY ASSESSMENT OF PHOTOGRAMMETRIC DIGITAL ELEVATION MODELS GENERATED FOR THE SCHULTZ FIRE BURN AREA

Danna K. Muise

This paper evaluates the accuracy of two digital photogrammetric software programs (ERDAS Imagine LPS and PCI Geomatica OrthoEngine) with respect to high-resolution terrain modeling in a complex topographic setting affected by fire and flooding. The site investigated is the 2010 Schultz Fire burn area, situated on the eastern edge of the San Francisco Peaks approximately 10 km northeast of Flagstaff, Arizona. Here, the fire coupled with monsoon rains typical of northern Arizona drastically altered the terrain of the steep mountainous slopes and residential areas below the burn area. To quantify these changes, high resolution (1 m and 3 m) digital elevation models (DEMs) were generated of the burn area using color stereoscopic aerial photographs taken at a scale of approximately 1:12000.

Using a combination of pre-marked and post-marked ground control points (GCPs), I first used ERDAS Imagine LPS to generate a 3 m DEM covering 8365 ha of the affected area. This data was then compared to a reference DEM (USGS 10 m) to evaluate the accuracy of the resultant DEM. Findings were then divided into blunders (errors) and bias (slight differences) and further analyzed to determine if different factors (elevation, slope, aspect and burn severity) affected the accuracy of the DEM. Results indicated that both blunders and bias increased with an increase in slope, elevation and

burn severity. It was also found that southern facing slopes contained the highest amount of bias while northern facing slopes contained the highest proportion of blunders.

Further investigations compared a 1 m DEM generated using ERDAS Imagine LPS with a 1 m DEM generated using PCI Geomatica OrthoEngine for a specific region of the burn area. This area was limited to the overlap of two images due to OrthoEngine requiring at least three GCPs to be located in the overlap of the imagery. Results indicated that although LPS produced a less accurate DEM, it was much more flexible than OrthoEngine. It was also determined that the most amount of difference between the DEMs occurred in unburned areas of the fire while the least amount of difference occurred in areas that were highly burned.

Acknowledgments

First and foremost, I wish to express my sincerest gratitude to Dr. Erik Schiefer, my advisor and committee chair, for his patience, motivation, enthusiasm and expertise. I am forever indebted to him for all the help and encouragement he has provided while working on this thesis, as well as throughout my entire graduate career. Additionally, I would like to thank my other committee members, Dr. Ray Huang and Mark Manone, for their valuable knowledge and contributions to this research.

I would also like to thank the following individual or group, for helping make this thesis a reality: the Rocky Mountain Research Station for providing funding as well as the aerial imagery used for this project; Matt Kaplinski and the guys in geology for letting me borrow the DGPS equipment and download my points for post-processing; Pam Foti for allowing me to use her backyard to set up the base station for my expanded area point collection; Ke-Sheng Bao for continually keeping my computer and software up to date; the NAU School of Nursing for allowing me to keep a flexible work schedule while working on this thesis; my fellow graduate students, especially Ashley York, Patrick Cassidy and Kevin Kent for sharing the joys and agonies of graduate school; Annie Lutes for keeping me company all those late nights spent writing in the GIS lab; and finally, Vai Shinde and Melissa Sukernick for their immeasurable friendship and constant reassurance that I would make it through this alive.

Last, but definitely not least, I would like to thank my family: my mom for her unwavering love and encouragement; my dad for his support and willingness to provide assistance whenever it was needed; and finally, my sister for providing a welcome escape from writing.

Table of Contents

Abstract ii

Acknowledgments iv

Table of Contents v

List of Tables vii

List of Figures viii

List of Appendices xi

i. Preface 1

1. Introduction 2

1.1 Literature Review 2

1.1.1 Photogrammetry 2

1.1.2 Comparing Different Systems 6

1.1.3 Comparing Different Programs 8

2. Automatic Terrain Extraction of the Schultz Burn Area 12

2.1 Abstract 12

2.2 Introduction 12

2.2.1 Study Area 13

2.2.2 Schultz Fire and Flooding 16

2.3 Methods 19

2.3.1 Aerial Photography and Ground Control 19

2.3.2 Initial Study Area Procedure 21

2.3.3 Extended Study Area 32

2.4 Results 38

2.5 Discussion 52

2.6 Conclusion 55

3. Comparing Schultz Burn Area Terrain Data Derived From Two Photogrammetric Software Programs 57

3.1 Abstract 57

3.2 Introduction 57

3.2.1 Software Programs 58

3.2.2 Study Area 59

3.3 Methods 61

3.3.1 ERDAS LPS 61
3.3.2 PCI OrthoEngine 67
3.4 Results 71
3.5 Discussion 82
3.6 Conclusion 84
4. Conclusions 85
5. Literature Cited 88
6. Appendix 92

List of Tables

Table 1.1 Comparison of literature utilizing different photogrammetric software programs to create DEMs. Additional parameters are also listed to compare different factors associated with the DEMs. 11

Table 2.1 GCPs from the original collection date (October 23, 2010). Green indicates the target was unable to be located on the photo and therefore was used as an elevation check point rather than ground control. 20

Table 2.2 Detailed information associated with the camera obtained from the 2009 calibrated camera report from the USGS. This information is used to determine the interior properties associated with the camera as they existed at the time photos were captured. 22

Table 2.3 Calibrated Fiducial Mark Coordinates. This information is used to insure the fiducial marks defined by LPS correspond to those defined by the camera. 23

Table 2.4 GCPs from the November 11th, 2011 collection date. Green indicates the target was unable to be located on the photo and therefore was not used as ground control. 33

Table 2.5 GCPs from the October 25th/28th, 2012 collection dates. Green indicates the target was unable to be located on the photo and therefore was used as an elevation check point rather than ground control. 35

Table 2.6 Zonal statistics which determined mean elevation difference as well as standard deviations for slope (A), elevation (B), aspect (C) and burn severity (D). 47

Table 2.7 Zonal statistics which determined mean proportion of blunders as well as standard deviations for slope (A), elevation (B), aspect (C) and burn severity (D). 48

Table 2.8 Values of the measured GCP elevations as well as elevations extracted from the DEM. These values were used to calculate absolute error as well as percent error for each of the points. 52

Table 3.1 Detailed camera calibration information. 62

Table 3.2 Calibrated fiducial mark coordinates. 62

Table 3.3 Seven of the original (pre-marked) GCPs that were located on the overlap of the two images. This information was entered into the software along with corresponding image locations. 65

List of Figures

Figure 2.1 Study areas (original – blue; expanded – green) within the Schultz Fire burn area and affected regions downslope. 15

Figure 2.2 Burn Progression of the Schultz Fire (Data: Coconino National Forest). 17

Figure 2.3 Burn Severity of the Schultz Fire (Data: Coconino National Forest). 18

Figure 2.4 Location of the original study area. This area was located primarily in the southern portion of the burn area and was based on the availability of original GCPs that could be located on the imagery. 24

Figure 2.5 Standard fiducial orientation of aerial photographs. The black bar indicates the data strip and includes information such as name, scale and date of photos. This strip is used to help establish fiducial marks and orient the photo. 25

Figure 2.6 Odd numbered photo orientation (A) and even numbered photo orientation (B). The black bar represents the data strip which was used to orient the photos. 26

Figure 2.7 The orientation of the fiducials marks based on the rotation of the data strip for the odd and even flight lines. 26

Figure 2.8 Different views used to examine the images and establish fiducial mark locations. They include overview (top right), main view (left) and detailed view (bottom right). 27

Figure 2.9 Dual display used to find control points and tie points found in the overlap area of two or more photos. Image 0302 (left) and image 0303 (right) are displayed and GCP x005 is identified on both image along with reference information. 29

Figure 2.10 The base (left) and rover (right) receivers used to determine coordinates of additional GCPs in the field. 34

Figure 2.11 Example of a natural feature (boulder; left) and a man-made feature (trough; right). The features were measured in the field then located on the images to be used as GCPs. 36

Figure 2.12 Location of the expanded study area. This area was based on the location of original GCPs (purple) as well as the collection of additional GCPs in the affected area during November 2011 (green) and October 2012 (blue). 37

Figure 2.13 Results from the original study area DEM. The detailed view provides a closer look at an obvious blunder area. These blunder areas were typically located along the western edge in the mountainous regions of the study area. 40

Figure 2.14 Results from the expanded study area DEM. This area covered approximately 2.4 times the original study location and included a greater representation of the area affected by the fire and flooding. 41

Figure 2.15 The 10 m DEM used as the reference when comparing differences in elevation to the expanded study area DEM. 42

Figure 2.16 The difference between the reference DEM and the expanded area DEM (left). Blue indicated values in the expanded DEM that were lower than the reference DEM while red indicated values that were higher than the reference DEM. 43

Figure 2.17 Elevation difference distribution between the two DEMs. Values above and below ±20 were considered blunders and removed from the data. Overall, there tends to be a negative bias (mean elevation difference = -1.611). 44

Figure 2.18 Reclassified values for slope (left) and elevation (right) based on the reference DEM..... 45

Figure 2.19 Reclassified values from aspect (left) and burn severity (right). 46

Figure 2.20 Mean elevation difference (left) and mean proportion of blunders (right) by slope. 49

Figure 2.21 Mean elevation difference (left) and mean proportion of blunders (right) by elevation. 49

Figure 2.22 Mean elevation difference (left) and mean proportion of blunders (right) by aspect. 50

Figure 2.23 Mean elevation difference (left) and mean proportion of blunders (right) by burn severity. 50

Figure 2.24 Unused GCPs which were unable to be located on the images and were instead used as check points to access the accuracy of the DEM. Of the 16 unused GCPs, three were unable to be included as check points due to their locations. 51

Figure 3.1 The southeastern edge of the San Francisco Peaks. This area was used to compare different DEMs and was based on the availability of GCPs found in the overlap area of two aerial photographs..... 60

Figure 3.2 Image 0405 (left) and 0404 (right). The red boxes indicate the overlap (approximately 70%) between these two images. These images were chosen based on the high number of GCPs found in the overlap area. Note: Top of image is east..... 63

Figure 3.3 The orientation of the fiducial marks based on the rotation of the data strip. 64

Figure 3.4 DEM generated by ERDAS Imagine LPS. The black arrows indicate major blunder areas that occurred during the extraction process. These areas were predominantly along the northern section of the study area as well as smaller mountainous areas on Schultz Peak. 71

Figure 3.5 DEM generated by PCI Geomatica OrthoEngine. The black arrow indicates a major blunder area that occurred during the extraction process. This area was focused on the northern section of the study area within the mountainous region of Schultz Peak. 72

Figure 3.6 The three different DEMs (ERDAS, PCI, and USGS) used for the study area. 73

Figure 3.7 Differences in elevation values based on PCI subtracted from ERDAS. Negative values (blue) indicate areas where ERDAS elevations were lower than PCI elevations, and positive values (red) indicate areas where PCI elevations were lower than ERDAS elevations. .. 74

Figure 3.8 Differenced elevation values with the major blunder areas removed. This included removing differenced values below -18 m as well as differenced values above 18 m (two standard deviations from zero). 75

Figure 3.9 Differenced elevation values with the major and moderate blunder areas removed. This included removing differenced values below -4.5 m as well as differenced values above 4.5 m (half a standard deviation from zero). 76

Figure 3.10 Orthophoto with major differenced areas (red and blue hatch mark) and moderate differenced areas (red and blue with gray transparency). Areas where minimum/no differences occurred where left clear. 77

Figure 3. 11 A close up view highlighting that for the moderate difference elevation, the DEM generated by PCI tended to be picking up tree canopies (left), while areas of minimum/no difference elevations tended to be focused over highly burned terrain (right). 78

Figure 3.12 Profile graph locations viewed using the PCI DEM. These locations were selected based on specific features such as over a gully (1) and across a ridge (2). 79

Figure 3.13 Profile graph locations viewed using the differenced dataset. These locations were selected to inspect certain areas where these differences occurred. 79

Figure 3.14 Profile graphs over selected features of interest. These included a gully (location #1), ridge-to-ridge (location #2), a severely burned wash (location #3) as well a flat, shadowed area along the pipeline (location #4). 80

Figure 3.15 Profile graphs over feature locations. These locations were selected to include areas over negative differenced values (location #5), positive differenced values (location #6), negative and positive differenced values (location #7) as well as a known blunder area (location #8). 81

Figure 3.16 Profile graph over location #1 which also includes degraded (10 m) DEMs from ERDAS and PCI. 83

List of Appendices

Appendix 6.1 Acronyms and abbreviations 92

Appendix 6.2 USGS Camera Calibration Report 93

Appendix 6.3 Exterior orientation associated with the imagery (red triangles represent GCP locations). 97

Appendix 6.4 Horizontal and vertical precision associated with the locatable GCPs collected with the DGPS equipment. These precision values ranged from 0.002 m to 0.051 m (horizontal) and 0.004 m to 0.074 m (vertical). 98

i. Preface

The purpose of this thesis is to present two manuscript chapters which were written with the intention of being submitted for publication. In Chapter 1, background literature pertaining to the subject matter of both manuscript chapters is examined and the findings are summarized. In Chapter 2, the first manuscript is presented. In this manuscript, I demonstrate how the digital photogrammetric software program ERDAS Imagine LPS was used to create a digital elevation model (DEM) of complex terrain following the high severity Schultz Fire. This high resolution (3 m) DEM was then compared to a reference DEM (USGS 10 m) to assess the overall accuracy associated with the data. The results were then further analyzed to determine how different factors (such as slope, aspect, elevation and burn severity) affected the accuracy of the DEM.

In Chapter 3, the second manuscript is presented. In this manuscript, two digital photogrammetric software programs (ERDAS Imagine LPS and PCI Geomatica OrthoEngine) are compared and the results are analyzed to check the overall performances regarding DEM extraction for a specific area following the Schultz Fire. Benefits and limitations involved with both software applications are presented and the accuracies of the two 1 m DEMs are assessed. This included differencing the two DEMs to determine inconsistencies between the data, as well as analyzing profile graphs over selected ground features of interest.

In Chapter 4, I present an overall summary of my findings from each manuscript chapter. Appendices are also included which contain important materials which were not presented in the chapters. Please note, due to the manuscript style of this thesis, there is some redundancy among the sections.

1. Introduction

1.1 Literature Review

1.1.1 Photogrammetry

Photogrammetry is defined as the art, science and technology of obtaining reliable information and measurements from photos (Zomrawi *et al*., 2013). The output of photogrammetry is typically a three-dimensional model of some real-world object or scene, and can be in the form of a digital terrain model (DTM) or a digital surface model (DSM). A DTM represents the terrain of the Earth (topography), while a DSM represents the surface of the Earth (topography and all natural or human-made features including vegetation and buildings). These models create an overview of an area of interest, and help us to visualize and analyze surface information.

Most commonly, a DTM is converted to a grid-based digital elevation model (DEM). According to Pulighe and Fava (2013), the DEM is one of the most fundamental requirements for a large variety of spatial analysis and modeling problems in environmental sciences. One major use for DEMs is quantifying landscape changes by differencing two or more surfaces acquired over different time intervals. This has been applied to measure surface changes involving glaciers (Baltsavias *et al.*, 1996; Kääb, 2002; Schiefer and Gilbert, 2007), coastal cliff erosion (Adams and Chandler, 2002), dune migration (Brown and Arbogast, 1999; Mathew *et al.*, 2010), gully erosion (Marzolff and Poesen, 2009), as well as mass movement involved with volcanoes (Baldi *et al.*, 2002; Kerle, 2002) and landslides (Kääb, 2002; Mora *et al*., 2003). Due to the widespread availability of historical and current aerial photographs, photogrammetric

techniques are often used to study these long-term and short-term morphometric changes, typically for interannual to interdecal time intervals.

Photogrammetry, like many other technology-based fields, is in a constant state of change and development. Over the past 175 years, four major stages of development have been recognized including plane table photogrammetry, analog photogrammetry, analytical photogrammetry, and digital photogrammetry (Torlegard, 1988). The transition between each stage has been largely dependent on the advancement of science and technology. This has included the invention of photography, airplanes, computers and digital imagery.

The first generation of photogrammetry (plane table) was established around 1850 with the invention of photography. This process involved extracting relationships between objects on photographs using geometric principles (Zomrawi *et al*., 2013). This included deriving angles and directions from measurements on photographs as an alternative to making geodetic observations in the field (Torlegard, 1988). Although initially limited to terrestrial purposes, advancements included the use of kites and balloons for aerial photography and mapping to cover larger areas. However, these systems were inherently unreliable, and it was not until the invention of the airplane that the next major stage of photogrammetry (analog) was developed.

This second generation is characterized by the use of stereo measurements (stereoscopy). Using optical or mechanical instruments, the three-dimensional geometry from two overlapping photographs (stereo pairs) could be constructed (Zomrawi *et al*., 2013). During this time, the world saw rapid developments in aviation, mostly as a result of the two world wars. In addition to advances with film and cameras, the use of

airplanes provided an improved platform for aerial imaging. It was during this stage where most of the foundations of aerial surveying techniques were established, many of which are still used today.

The next generation came with the advent of the computer and is known as analytical photogrammetry. This new equipment replaced many of the expensive optical and mechanical components of analog systems. This method uses mathematical equations to establish relations between object points and image points (Ghosh, 1988). Relations between these points is based on the collinearity equations, which relate coordinates in a sensor plane (in two dimensions) to object coordinates (in three dimensions). However, the process of collecting data is still highly intuitive and often requires an experienced operator if high accuracies are to be achieved (Baily *et al.*, 2003).

In contrast to all other phases, digital photogrammetry uses images stored on a computer (softcopy) instead of aerial photographs (hard copy). These digital images can be scanned from photographs or directly captured by digital cameras and transferred to a computer (Zomrawi *et al*., 2013). Digital photogrammetric systems employ sophisticated software to automate the tasks associated with conventional photogrammetry. The output products are also stored in digital form and can be easily stored, managed, shared, or imported into a geographic information system (GIS).

In the past 25 years, there has been a major shift from analog and analytical methods to digital methods (Baily *et al*., 2003, Ruzgiene and Aleknine, 2007). A major advantage of automated digital photogrammetry over other surveying techniques is the greatly increased rates at which DEMs can be generated. This may be up to 100 times faster than those provided by earlier manual photogrammetric methods, and up to 1000

times faster when compared to the use of a modern total station or digital tachometer in the field (Chandler, 1999). However, although digital methods have the potential to replace previous analog and analytical technologies (Baily *et al.*, 2003), Gong *et al.* (2000) found that source data measured manually with analytical plotters was the most reliable because automated measurements using image matching techniques could produce systematic errors. As a result, Ruzgiene and Aleknien (2007) suggest that analytical photogrammetry is still a significant production system and should be used in conjunction with digital methods for the most accurate results.

Since there has been such a major shift to digital automated methods, Chandler (1999) offers various recommendations that enable the inexperienced user to make effective use of digital photogrammetry. This includes the role of photo-control, the significance of checkpoints, and the importance of camera calibration data. He states that even though there have been improvements to many of the procedures, some expertise is still required to obtain accurate results. Gooch and Chandler (1999) also acknowledge that the user is allowed a degree of control over certain strategy parameters when generating a DEM and wrong choices could have a significant detrimental effect on the accuracy of the DEM. As a result, only through understanding the significance of these parameters can the accuracy of DEMs be optimized.

Overall, the generation of DEMs using automated digital photogrammetry represents an important advance to representing and quantifying landform morphology. However, it is important to remember that there is considerable potential for problems to occur, especially if the user has no previous background in photogrammetry (Lascelles *et al.*, 2002). This becomes apparent when inexperienced users become disillusioned with

photogrammetric science, when an overly ambitious project fails to achieve expected results (Chandler, 1999). According to Lascelles *et al*. (1999), this will become less likely as more studies are published, and the methodology and its strengths and limitations become better known.

1.1.2 Comparing Different Systems

As stated by Chandler (1999), although photogrammetry provides one efficient means of deriving DEMs, there are other methods available. Presently, numerous DEM generation techniques are being utilized which have different accuracies and are used for different purposes (Sefercik, 2007). These include direct ground surveying, digitized topographic maps, airborne laser scanning (ALS), synthetic aperture radar (SAR), as well as various other methods. As a result, it is important to compare the DEMs generated from these different data sources to determine which method produces the most accurate results based on a specific purpose. Below are just a few of the studies conducted to determine accuracies of DEMs generated by different data sources.

In a study conducted by Sefercik (2007), three different generation methods were used to produce a DEM of Zonguldak, a mountainous region in north-western Turkey. This included digitized contour lines of 1:25000 scale topographic maps, a photogrammetric flight project, and Shuttle Radar Topography Mission (SRTM) X-band data which used single pass Interferometric Synthetic Aperture Radar (InSAR). These DEMs were then compared to determine the accuracy of each DEM, especially related to open and flat areas as well as forested areas. Based on the results, the DEM produced by the photogrammetric flight produced the most accurate DEM when compared to the other methods.

Another study that compared three different data sources was conducted by Rayburg *et al*. (2009) for the Narran Lake Ecosystem in northwestern New South Wales, Australia. This included a nine-second DEM derived from spot heights taken from 1:100000 scale topographic maps, a 20000-point differential GPS (DGPS) ground survey, and a LiDAR (light detection and ranging) survey. Based on the results, the LiDAR and DGPS-derived data generated a more thorough DEM than the nine-second DEM. However, LiDAR generated a surface topography that yielded significantly more detail than the DGPS survey.

Finally, Adams and Chandler (2002) evaluated LiDAR and digital photogrammetry, the quality of which was assessed using a third DEM derived using a total station and conventional ground survey methods. It was assumed that ground survey data would be more accurate than the other methods used, therefore allowing the accuracy of those methods to be assessed. Based on the results, the LiDAR data proved to be more accurate than photogrammetry, but both data sets displayed a tendency to generate heights slightly lower than the elevation of the terrain surface.

Based on the above studies, it seems that DEMs derived from total stations and conventional ground survey methods produce results with the highest accuracies. However, as mentioned, this process is extremely time consuming and labor intensive, and other techniques such as digital photogrammetry and LiDAR allow very dense DEMs to be generated which can accurately record detailed morphology. However, there are benefits and limitations to both of these systems, and it is important to determine which is better for a specific purpose.

Recently, there has been a major shift to applications in geomorphological studies that use LiDAR surveys (Rayburg *et al,* 2009). One of the appealing features in the LiDAR output is the direct availability of three-dimensional coordinates of points in object space (Habib *et al*., 2005). Using light in the form of a pulsed laser, three-dimensional information about the shape of the Earth and its surface characteristics can be generated. Due to the systematic errors involved with automated procedures, this data is often more accurate when compared to photogrammetry. Another major benefit to LiDAR data is its ability to penetrate through vegetation and measure surfaces through the tree canopies.

One major limitation according to Mathew *et al*. (2010) is that LiDAR data have only been available for about one decade. This greatly limits the application of studying historical changes in landscape, which is a major goal of many geomorphological studies. Additionally, LiDAR can be prohibitively expensive when compared to photogrammetry. As a result, photogrammetric techniques have and will continue to play a major role in measuring landscape changes for years to come.

1.1.3 Comparing Different Programs

According to Chandler (1999), software to carry out the photogrammetric processing is now available commercially at competitive rates, particularly for academic usage. Some examples of the available software he mentions are ERDAS Imagine OrthoMAX, PCI Geomatica EASI-PACE, R-WEL Desktop Mapping System and VirtuoZo. Other software programs that have been utilized more recently include PCI Geomatica OrthoEngine (Schiefer and Gilbert, 2007; Mathew *et al*., 2010), Helava DPW710 (Baldi *et al*., 2002), LH Systems SOCET SET (Kääb, 2002; Baily *et al*., 2003;

Mora *et al*., 2003) and ERDAS Imagine LPS (Marzolff and Poesen, 2009). These software packages have been developed for a wide market including non-photogrammetrists, and they help guide the novice through the various photogrammetric procedures through the use of dialogue boxes, user manuals/guides, and on-line help (Chandler, 1999). Table 1.1 documents a variety of these software programs, based on a comprehensive literature review, and lists different parameters that were used when generating DEMs. This included utilizing various image scales (ranging from 1:3000 to 1:40000) as well as scanning resolutions (7µm to 42 µm) resulting in a variety of ground pixel sizes (0.08 m to 0.8 m). The resultant DEMs consisted of resolutions ranging from 0.2 m to 10 m.

Due to advancements in technology, many of these software programs have transitioned from previously developed programs into new versions or completely new products. One example of this is the evolution of ERDAS Imagine OrthoMAX (1995), to OthoBASE (1999), Leica Photogrammetry Suite (2004), LPS (2008), and most recently, Imagine Photogrammetry (2014). With each stage of development, there are improvements to certain aspects of the software that were often limited in the previous version. However, as these digital photogrammetric systems become more sophisticated and the level of automation increases, the technical gap between the user and the system grows (Gooch and Chandler, 1999). As a result, it is important to understand the capabilities of these different software programs and choose the best one based on your abilities and needs.

Only a few studies have been conducted that compare one or more of these software programs in the generation of DEMs. This includes Baltsavias *et al*. (1996)

comparing Leica-Helava DPW 770 with VirtuoZo, Ruzgiene (2007) comparing DDPS (Desktop Digital Photogrammetry System) software with DPW (Digital Photogrammetric Workstation) LISA FOTO, and Acharya and Chaturvedi (1997) comparing Leica-Helava, Autometric and Intergraph's Match-T. Typically, results indicated there were benefits and limitations for each software program. For example, Ruzgine concluded that although DDPS was easier to use and had faster image processing and management, it was limited in photogrammetric processing possibilities (such as orthophoto production) when compared to LISA FOTO. Similarly, Baltsavias *et al.* found that although VirtuoZo was more user-friendly and could be obtained at a lower price, it lacked many of the functionalities included with DPW 770 such as aerial triangulation and mapping. As a result, additional studies are needed to determine exactly which of the more recent software programs should be used based on desired DEM outcomes and accuracies for specific applications.

Table 1.1 Comparison of literature utilizing different photogrammetric software programs to create DEMs. Additional parameters are also listed to compare different factors associated with the DEMs.

Reference	Year	Software	Additional Parameters			
			Photo Scale	Scanned	Ground Pixel Size	DEM Res.
Adams and Chandler	2002	ERDAS Imagine/OrthoMAX	1:7500	20 µm	0.16 m	2 m
Baily *et al.*	2003	LH Systems/SOCET SET	1:4000	20 µm	0.08 m	0.25 m to 1 m
Baldi *et al.*	2002	Helava/DPW 710	1:5000	25 µm	0.12 m	1 m
Brown and Arbogast	1999	PCI Geomatica/OrthoEngine	1:16000 to 1:20000	42 µm	0.7 m to 0.8 m	3 m
Fabris and Pesci	2005	Helava/DPW 770	1:5000 to 1:37000	12 µm to 24 µm	0.13 m to 0.45 m	1 m to 10 m
Kääb	2002	LH Systems/SOCET SET	1:7000 to 1:10000	30 µm	0.2 m to 0.3 m	0.2 m to 0.3 m
Kerle	2002	ERDAS Imagine/OrthoMAX	1:40000	14 µm	0.56 m	5 m
Lane *et al.*	2000	ERDAS Imagine/OrthoMAX	1:3000	25 µm	0.08 m	0.2 m to 2 m
Mathew *et al.*	2010	PCI Geomatica/OrthoEngine	1:4000 to 1:17000	7 µm to 20 µm	0.08 m to 0.12 m	
Mora *et al.*	2003	LH Systems/SOCET SET	1:4400	25 µm	0.11 m	0.5 m
Pulighe and Fava	2013	ERDAS Imagine/LPS	1:34000	21 µm	0.7 m	5 m
Schiefer and Gilbert	2007	PCI Geomatica/OrthoEngine	1:10000 to 1:40000	7 µm to 30 µm	0.3 m	0.3 m to 0.4 m

2. Automatic Terrain Extraction of the Schultz Burn Area

2.1 Abstract

The aim of this study was to evaluate the digital photogrammetric software program ERDAS Imagine LPS with respect to high-resolution terrain modeling in a complex topographic setting affected by fire and flooding. Using stereoscopic aerial photography acquired from the Schultz Fire burn area in October 2010, I report on the procedure, highlight potential benefits and limitations, and evaluate the quality of the resultant 3-meter digital elevation models (DEMs). The results were then examined further to determine if various conditions including slope, elevation, aspect, or burn severity affected the precision and accuracy of the generated DEMs. Findings indicate that the accuracy of the DEM decreased in areas of greater slopes, higher elevations, northern and southern facing slopes, and areas of high burn severity. These results were based on obvious blunders (errors) as well as biases (slight differences from a reference DEM).

2.2 Introduction

During the summer of 2010, the San Francisco Peaks near Flagstaff, Arizona were impacted by a high severity wildfire, followed shortly by near record monsoonal rains (Youberg *et al.*, 2010). Fueled by high winds, the human-caused Schultz Fire quickly spread across the steep mountainous slopes and grew to 6100 ha between June 20th and June 30th, becoming the largest fire in Arizona during 2010.

Shortly following the fire, ample rains from the monsoon resulted in debris flows, significant erosion, and extensive flooding to the area on and below the burn. The hydrologic behavior of the landscape was dramatically impacted as a result of the

removal of forest floor litter, alteration of soil characteristics, development of fire-induced water repellency, and loss of tree canopy cover in the moderate and high severity burn areas (Youberg *et al*., 2010).

As a way to quantify and document these impacts, it is crucial to investigate how the land surface has changed, as well as how it continues to change in the affected areas as a result of the fire and flooding. One proposed way to examine these impacts was by means of aerial photography and the application of digital photogrammetry. Few studies have been published which use this procedure to assess severely burned forest terrain following a fire.

Photogrammetry is a measurement technology that can be used to extract three-dimensional information from imagery to produce a digital terrain model (DTM). Recent improvements in digital procedures have automated the extraction process and have greatly increased the efficiency of topographic data collection and DTM generation. These outputs can then be saved in a variety of formats, such as grid-based DEMs (raster).

Based on the quality and accuracy of the DEMs acquired from these programs, there is the potential to use the results to study the land changes on the San Francisco Peaks (or potentially, similar areas affected by fire) for years to come. This new detailed information can then be used in a Geographic Information System (GIS) to perform further analysis such as in-depth hydrological studies.

2.2.1 Study Area

The San Francisco Peaks are a group of mountains in northern Arizona that are the remnants of an eroded Middle Pliocene to Holocene-aged stratovolcano. Just north of

Flagstaff, these mountains form the tallest range in Arizona and consist of seven prominent peaks over 3000 m including Schultz Peak (3073 m), Doyle Peak (3493 m), Rees Peak (3497 m), Aubineau Peak (3608 m), Fremont Peak (3648 m), Agassiz Peak (3766 m) and the tallest, Humphreys Peak (3851 m).

The San Francisco Peaks consist of diverse biomes spanning different elevations including ponderosa pine forests (1800 m to 2600 m), mixed conifer forests (2400 m to 2900 m), subalpine conifer forests (2900 m to 3500 m) and alpine tundra (above 3500 m) (Brown, 1994). These zones see a range of precipitation, averaging from 460 mm to 660 mm in the ponderosa pine forests all the way up to 1000 mm in the alpine tundra. Traditional land uses of this area have included grazing of livestock, logging, and mining of cinders and pumice (Grahame and Sisk, 2002). Currently, this area is a popular destination for outdoor recreation (motorized and non-motorized) and tourism.

The primary focus area for this research was located on the eastern edge of the San Francisco Peaks, predominantly within the Schultz Fire burn area and affected regions downslope (Figure 2.1). Here, the fire coupled with intense post-fire monsoonal rains typical for northern Arizona between July and September, significantly altered the terrain on the steep mountainous slopes and lower residential areas. The original study area was selected based on the availably of pre-marked ground control points (GCPs) located in aerial photography acquired after the fire and two major flooding events. The expanded area was based on the availably of additional aerial photographs from the flight, as well as the collection of additional GCPs the following two years (November 2011 and October 2012).

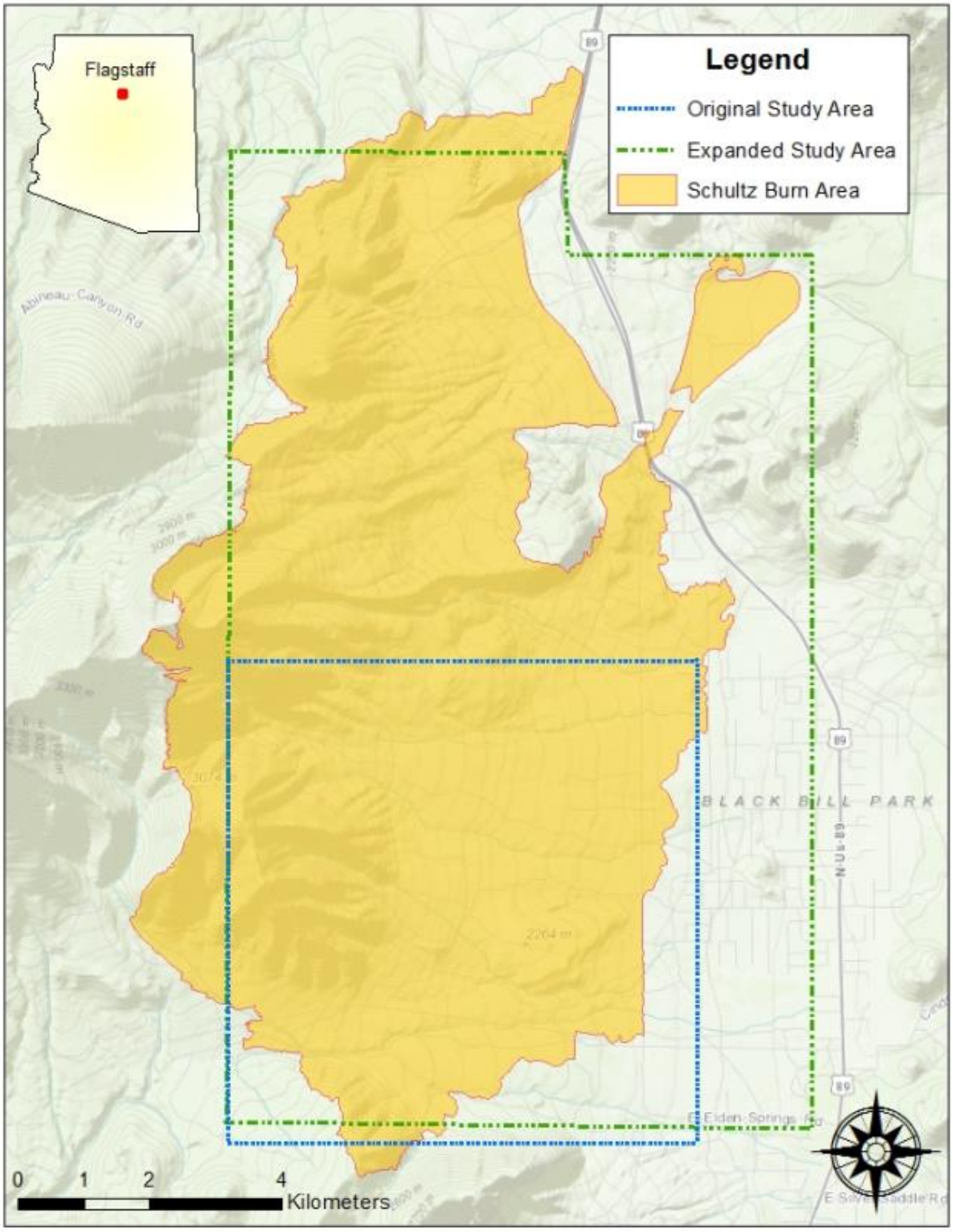

Figure 2.1 Study areas (original – blue; expanded – green) within the Schultz Fire burn area and affected regions downslope.

2.2.2 Schultz Fire and Flooding

Ignited as a result of an abandoned campfire on June 20th, the Schultz Fire started around the area of Schultz Tank and Little Elden Trail within the southeastern reaches of the San Francisco Peaks. Quickly spreading across the eastern slopes as a result of high winds, the Schultz Fire burned approximately 60% of the total 6100 ha during the first day (Figure 2.2) prompting numerous evacuations and road closures.

Approximately 40% of the fire was classified as high severity (Figure 2.3) due to the complete loss of protective ground cover and the creation of hydrophobic soil conditions (U.S. Forest Service, 2010). These areas were typically located on steep slopes (greater than 30%) and were areas of concern due to the potential for accelerated rates of soil erosion and debris flows typical after a fire (Neary *et al*., 2012).

Between July and September, monsoonal thunderstorms tend to form over the San Francisco Peaks due to orographic lifting. Before the fire was even contained, a U.S. Forest Service Burned Area Emergency Response (BAER) team began to assess the impacts and determine appropriate mitigation measures to reduce flooding potential and retain on-site soils before the impending monsoon season (U.S. Forest Service, 2010).

On July 20th, the first major impact storm occurred and brought 45 mm of rain within 45 minutes (Youberg *et al*., 2010). This event triggered the first round of debris flows, and flooding was detrimental to the residential communities below the fire. The effects of the flooding were also surprisingly widespread, as housing developments up to 6 km from the fire experienced impacts from the flooding.

Another second high intensity storm occurred on August 16th and delivered 27 mm of rain in 46 minutes and resulted in additional debris flows (Youberg *et* al., 2010).

These two storms, along with near record rains for 2010 caused substantial damage and could continue to impact this area for years to come.

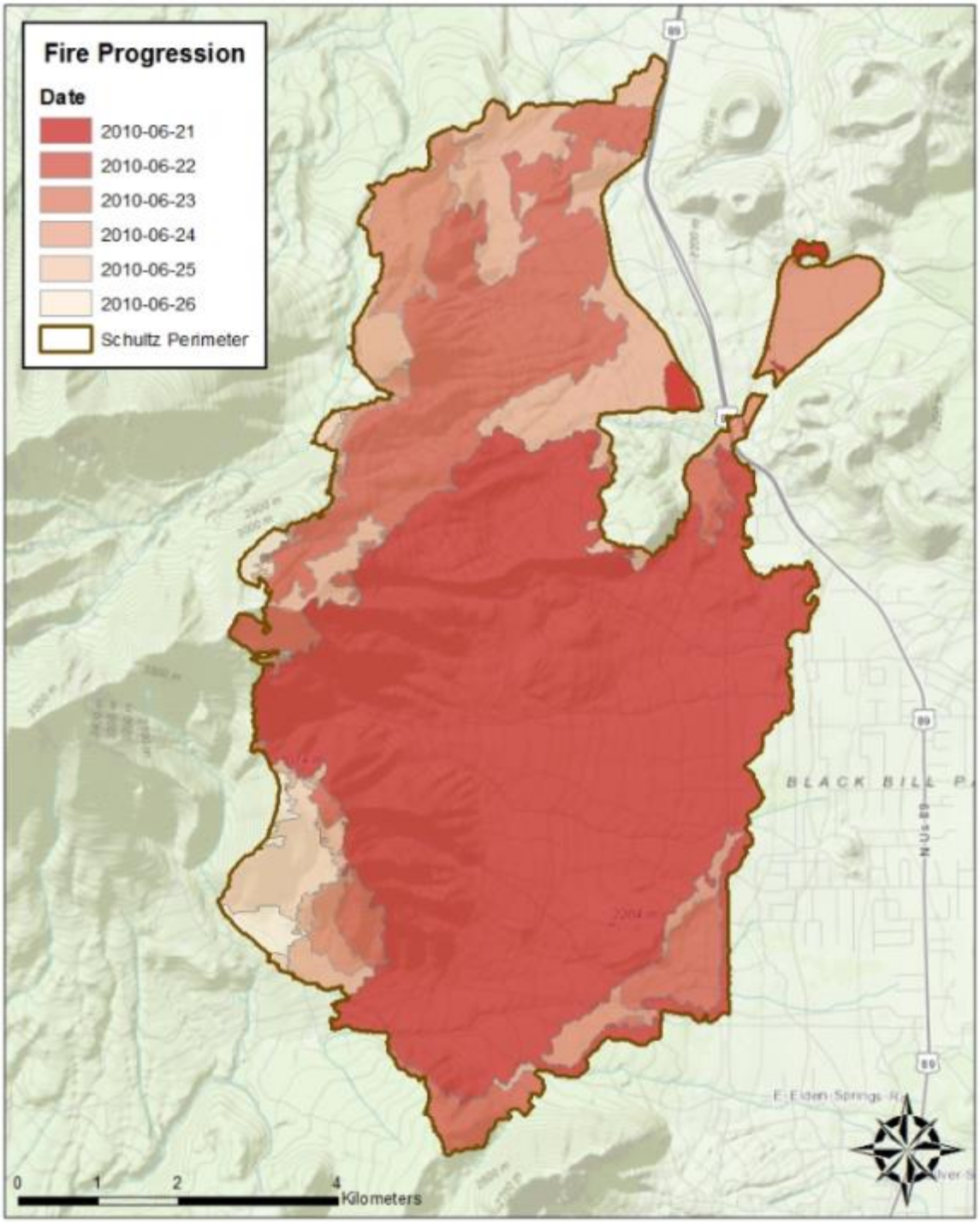

Figure 2.2 Burn Progression of the Schultz Fire (Data: Coconino National Forest).

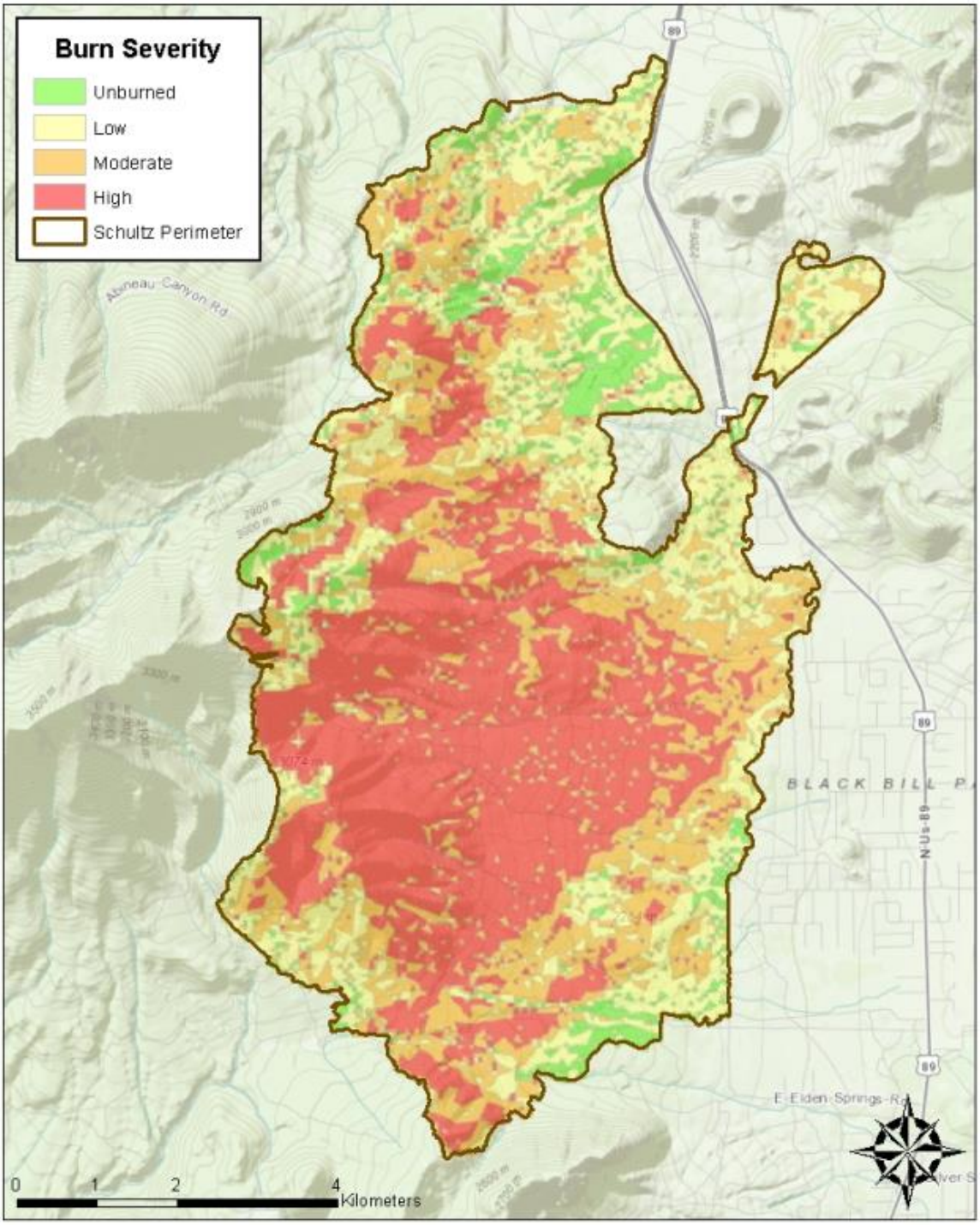

Figure 2.3 Burn Severity of the Schultz Fire (Data: Coconino National Forest).

2.3 Methods

2.3.1 Aerial Photography and Ground Control

To assess, document and monitor the effects of fire and flooding on geomorphic and watershed processes following the Schultz Fire, geoscientists from the Arizona Geological Survey (AZGS) teamed up with researchers from the U.S. Forest Service Rocky Mountain Research Station's (RMRS) Southwest Watershed Team in early August of 2010 (Youberg *et al*., 2010). One of the ways intended to monitor these effects was through repeat aerial photography of the burned area.

On October 27, 2010, the first set of aerial photographs was acquired. These photos were taken at a nominal scale of 1:12000 by Kenney Aerial Mapping (Phoenix, Arizona) at an average flying height of 1836 m. The aircraft was equipped with a Zeiss RMK TOP camera system including a TAS gyro mount and a T-MC forward motion compensating magazine. The photos were scanned at 14 microns (equivalent to 1814 dots per inch), resulting in a nominal ground resolution of approximately 17 cm, and had 16-bit color depth.

A few days prior to the photo collection, a total of 28 (1.2 x 1.2 m) iron-cross aerial targets were positioned throughout the affected area to be used as pre-marked GCPs. This positioning took place through the efforts of Dr. Erik Schiefer of Northern Arizona University (NAU) with assistance from RMRS staff. Using Differential Global Positioning System (DGPS) equipment, the three-dimensional coordinates (longitude (X), latitude (Y) and elevation (Z)) were obtained in reference to the center of the target (Table 2.1). These targets were then secured at this point of reference to mark a target position for the upcoming fly-over.

Table 2.1 GCPs from the original collection date (October 23, 2010). Green indicates the target was unable to be located on the photo and therefore was used as an elevation check point rather than ground control.

Original Ground Control Points					
GCP ID	**Longitude (X)**	**Latitude (Y)**	**Elevation (Z)**	**Lat DD**	**Long DD**
x001	111:35:19.63090 W	35:19:09.94748 N	2262.77 m	35.31942986	-111.5887864
x002	111:35:03.01191 W	35:19:35.49939 N	2225.931 m	35.32652761	-111.58417
x003	111:34:45.98165 W	35:20:05.20477 N	2212.447 m	35.3347791	-111.5794394
x004	111:34:13.12204 W	35:18:13.55867 N	2126.478 m	35.3037663	-111.5703117
x005	111:35:59.51427 W	35:16:58.75567 N	2280.6 m	35.28298769	-111.5998651
x006	111:36:38.88379 W	35:17:08.87393 N	2334.08 m	35.28579831	-111.6108011
x007	111:35:33.91068 W	35:18:36.08930 N	2264.013 m	35.31002481	-111.592753
x008	111:35:51.73256 W	35:17:42.79966 N	2270.562 m	35.29522213	-111.5977035
x009	111:36:27.72097 W	35:17:35.55066 N	2330.638 m	35.29320852	-111.6077003
x01	111:37:18.34675 W	35:17:26.97140 N	2433.976 m	35.29082539	-111.621763
x010	111:34:58.03655 W	35:16:44.06415 N	2182.478 m	35.27890671	-111.5827879
x011	111:34:36.76979 W	35:16:50.09956 N	2150.459 m	35.28058321	-111.5768805
x012	111:35:51.67092 W	35:16:53.42674 N	2265.16 m	35.28150743	-111.5976864
x013	111:37:02.32270 W	35:17:18.56448 N	2390.998 m	35.28849013	-111.6173119
x02	111:36:46.75766 W	35:17:40.86564 N	2464.969 m	35.2946849	-111.6129882
x03	111:36:28.49988 W	35:18:02.45758 N	2492.138 m	35.30068266	-111.6079166
x04	111:36:34.92218 W	35:18:17.63510 N	2516.157 m	35.30489864	-111.6097006
x041R	111:34:47.45270 W	35:21:18.29730 N	2254.738 m	35.35508258	-111.579848
x042R	111:34:45.20918 W	35:21:07.62507 N	2268.823 m	35.35211808	-111.5792248
x044R	111:34:13.84802 W	35:20:00.45133 N	2137.343 m	35.3334587	-111.5705133
x045R	111:34:10.98009 W	35:19:45.28022 N	2125.405 m	35.32924451	-111.5697167
x05	111:36:48.18130 W	35:18:49.67911 N	2570.116 m	35.31379975	-111.6133837
x06	111:37:11.41892 W	35:19:28.73627 N	2644.836 m	35.32464896	-111.6198386
x07	111:36:50.82588 W	35:19:55.79578 N	2697.832 m	35.33216549	-111.6141183
x08	111:36:56.46686 W	35:20:17.58296 N	2735.636 m	35.33821749	-111.6156852
x09	111:37:17.68503 W	35:20:34.39625 N	2761.831 m	35.34288785	-111.6215792
x10	111:37:25.88280 W	35:20:59.04063 N	2796.692 m	35.34973351	-111.6238563
x11	111:36:57.59815 W	35:21:16.45175 N	2682.824 m	35.35456993	-111.6159995

A majority of these targets were positioned in open areas along Forest Service roads around and within the burn area. These areas were selected so that when the aircraft collected the photos, it would be able to capture the target from different angles spanning multiple frames. If the tree cover was too thick, or there were other obstructions, the

target could not be located on the image and that point would not be used as ground control. Some of the targets were disturbed prior to the flight, and as a result, were unaccounted for in the photos. Of the 28 total targets, seven were unable to be located on the photos. Based on the availability of points that could be located, the initial study area was determined for analysis and the creation of the initial DEM.

2.3.2 Initial Study Area Procedure

The digital photogrammetric software used in this study was ERDAS (Earth Resources Data Analysis Systems) Imagine 2010, specifically, an extension called LPS (Leica Photogrammetry Suite; name officially and legally changed to LPS) ATE (Automatic Terrain Extraction). This program allowed fast and accurate automatic terrain extraction from multiple images. Using a robust algorithm, it was able to compare two images and look for the image positions of conjugate features appearing in the overlap portions of the image (Leica Geosystems Geospatial Imaging, 2006). The three-dimensional position of the features could then be computed following the establishment of the interior and exterior orientation associated with the imagery.

Prior to performing any photogrammetric task within LPS, a block had to be created. A block is a term used to describe and characterize all of the information associated with a photogrammetric mapping project (Leica Geosystems Geospatial Imaging, 2009). This included projection information, camera or sensor information, imagery associated with the project, GCPs and their measured image position, and the geometric relationship between the imagery in the project and the ground.

To first create a block, I had to specify that a frame camera was used as the geometric model. Single-lens frame cameras are the most common film cameras and are

usually associated with aerial cameras having an approximate focal length of 152 mm and fiducial marks positioned within the camera body. I also had to identify the different rotation system used (Omega – rotation about the X axis, Phi - rotation about the Y axis, and Kappa - rotation about the Z axis), the angle units (degrees), as well as the horizontal and vertical reference coordinate system (WGS 84).

The next step was to identify parameters associated with the camera to determine the interior geometry of the camera as it existed when the photos were captured. Aerial cameras need to be calibrated for a number of important parameters before they are used to determine precise measurements from photos. These cameras are kept current with calibrations done by the United States Geological Survey (USGS). This included defining camera properties such as calibrated focal length, principle points, and radial lens distortions (Table 2.2). This material was provided in a calibrated camera report obtained from Kenney Aerial Mapping along with the digital images.

Table 2.2 Detailed information associated with the camera obtained from the 2009 calibrated camera report from the USGS. This information is used to determine the interior properties associated with the camera as they existed at the time photos were captured.

Camera Information	
Camera Type	Zeiss RMK Top 15
Calibrated Focal Length (mm)	152.9940
Principal Point xo (mm)	-0.0100
Principal Point yo (mm)	0.0100
K_0 (radial lens distortion)	3.834e-06
K_1 (radial lens distortion)	1.057e-09
K_2 (radial lens distortion)	-9.316e-14

In addition to the calibrated camera information, I had to define the number of fiducial marks located on a photo and enter their calibrated X and Y photo-coordinate

values (Table 2.3). Fiducial marks are imaged by the camera on each exposure and are used to orient photogrammetric instruments to the camera coordinate system.

Table 2.3 Calibrated Fiducial Mark Coordinates. This information is used to insure the fiducial marks defined by LPS correspond to those defined by the camera.

Row #	Film X (mm)	Film Y (mm)
1	-113.013	-112.996
2	113.004	113.012
3	-112.992	112.994
4	113.008	-112.996
5	-113.002	0.000
6	113.015	0.011
7	0.004	113.007
8	-0.011	-112.999

There are usually between four and eight fiducial marks, located on the photo corners, middle edges or both. During the camera calibration process, the positions of the fiducial marks are precisely measured and the principal point (geometric center) of the image can be derived from the intersection of the fiducial marks. This defines a photo-coordinate system within each image, as well as determines the origin and orientation of the photo-coordinate system for each image in the block (Leica Geosystems Geospatial Imaging, 2009).

Once this preliminary information was entered, the images could be added to the block. A total of 18 images were used for the initial study area and consisted of three flight strips containing six images each (0201-0206, 0302-0307 and 0403-0408). Again, these were chosen based on the availability of the GCPs that could be located on the images and were focused primarily on the southern part of the burn area (Figure 2.4).

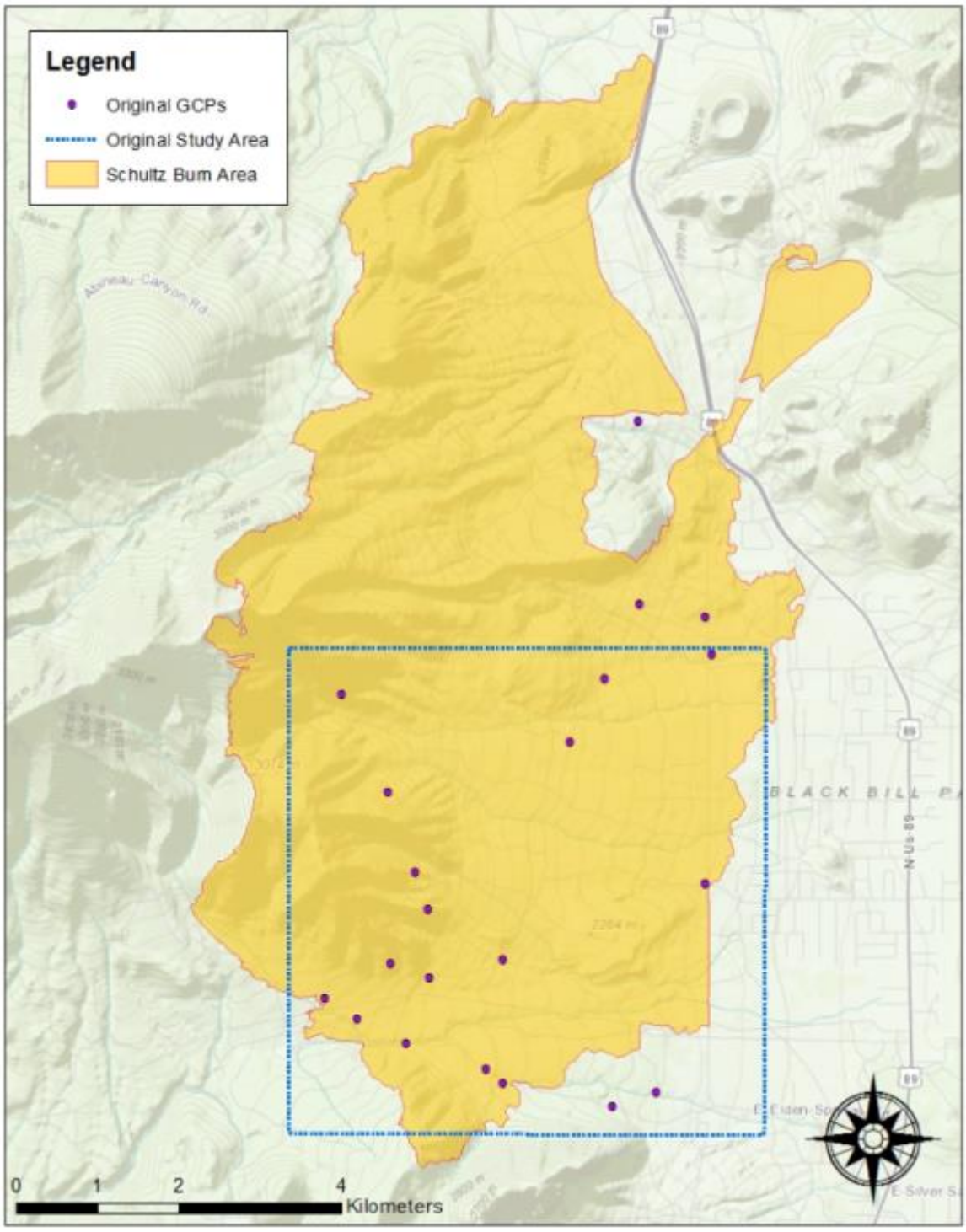

Figure 2.4 Location of the original study area. This area was located primarily in the southern portion of the burn area and was based on the availability of original GCPs that could be located on the imagery.

Typically, flight strips contain 60% to 80% end lap between adjacent images and about 30% side lap between images in neighboring strips. Due to the complexity of the steep mountainous terrain, the side lap between images in these flight strips was increased from 30% to as high as 50% to ensure all the area was included.

The next step was to determine the interior orientation of the images. This process involved measuring the pixel coordinate positions of the calibrated fiducial marks on each image within the block. However, before the fiducial marks could be measured, the correct orientation of the images had to be determined. The orientation of the image was largely dependent on the way the photos were scanned during the digitization stage.

Typically, the data strip is used as a reference in determining the manner in which the camera was calibrated (Figure 2.5). This helps insure that the numbering of the fiducial marks is consistent with how it was defined in the camera calibration report.

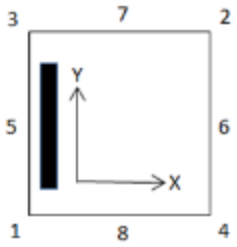

Figure 2.5 Standard fiducial orientation of aerial photographs. The black bar indicates the data strip and includes information such as name, scale and date of photos. This strip is used to help establish fiducial marks and orient the photo.

When the photos were scanned, the odd numbered flight strips (0100s and 0300s) and even numbered flight strips (0200s and 0400s) were rotated. The orientation was then adjusted based on the standard orientation. For the odd numbered images, the top of the photo was west and the data strip was on the left (south), while for the even numbered images, the top of the photo was east and the data strip was on the left (north; Figure 2.6).

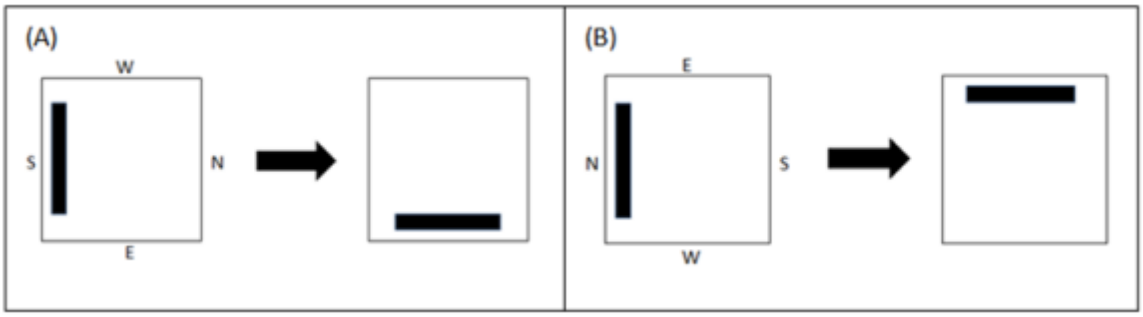

Figure 2.6 Odd numbered photo orientation (A) and even numbered photo orientation (B). The black bar represents the data strip which was used to orient the photos.

Based on this information, the position of the fiducial marks in the odd numbered photos were rotated 270º relative to the photo-coordinate systems, and the even numbered photos were rotated 90º relative to the photo-coordinate system (Figure 2.7).

Odd Flight Lines (Rotated 270°) Even Flight Lines (Rotated 90°)

Figure 2.7 The orientation of the fiducials marks based on the rotation of the data strip for the odd and even flight lines.

Once each photo was assigned the correct rotation, the fiducial marks could be established by clicking on the center of the mark, following the correct numbering sequence. To determine the center of the fiducial mark, the photos could be displayed within three views; overview, main view and detail view (Figure 2.8). These windows helped insure the correct location (middle of mark) was selected when determining fiducial mark locations.

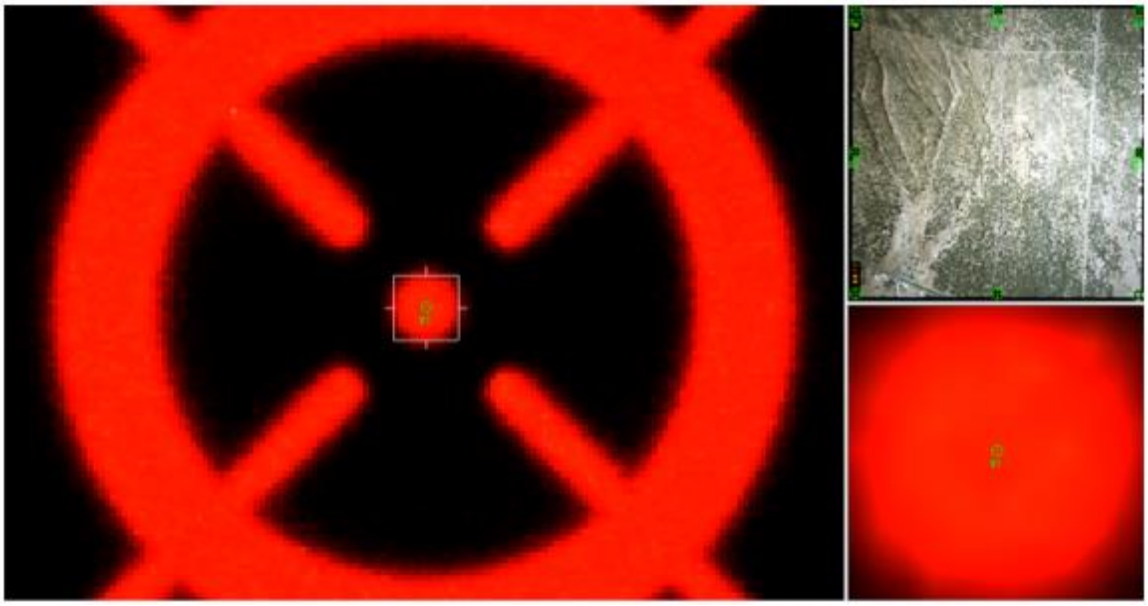

Figure 2.8 Different views used to examine the images and establish fiducial mark locations. They include overview (top right), main view (left) and detailed view (bottom right).

Based on the selected rotation, the software would automatically start in the general area of the first fiducial mark (#1) and move to the next general location (#2) once the first mark was established. Once the first two fiducial marks were established, it would continue to move to the next correct location, with better accuracy in finding the center of the next mark.

Once all eight fiducial marks were established, corresponding residuals were displayed. These residuals (Residual X and Residual Y) were computed based on a mathematical comparison made between the original fiducial mark position and the actual measured fiducial mark position. Based on the values of the eight residuals, a root mean square error (RMSE) could be calculated. The RMSE represented the overall correspondence between the calibrated fiducial mark coordinates and their measured image coordinates. These values ranged from 0.66 to 0.72 pixels for the 18 images. Values larger than 0.5 pixels inferred systematic errors or gross measurement errors

associated with the image. The errors could be attributed to film deformation, poor scanning quality, mis-measured fiducial mark positions, or incorrect calibrated fiducial mark coordinates (Leica Geosystems Geospatial Imaging, 2009). For future studies, it is recommended to review these settings again to make sure they were entered properly.

After establishing the interior orientation of the images, external properties, if available, could be defined. To determine the external properties associated with a camera, the exterior orientation parameters (Omega, Phi, Kappa) associated with the camera as they existed at the time of photographic exposure had to be established. However, no exterior orientation parameters were available, and as a result, these parameters could only be determined through aerial triangulation.

Aerial triangulation is the process of defining the mathematical relationship between the images contained within a block, the camera that obtained the images, and the ground (Leica Geosystems Geospatial Imaging, 2009). To perform aerial triangulation, GCPs and tie points had to first be identified on all of the overlapping image areas. Using a dual display, two images could be viewed to find a specific point common in both photos (Figure 2.9). These windows featured a similar view display for determining fiducial mark positions (overview, main view and detailed view).

Since GCPs are identifiable features whose ground coordinates are known (Table 2.1), locating these points in the overlap areas helped determine how the images were related spatially to other images. Tie point are also used to determine how the imagery is related, but do not include any coordinate information. Only the image positions in the overlap areas are known and measured, and X, Y and Z coordinate can only be estimated

during the aerial triangulation process. Once these values have been estimated, the point can be used as a control point for other applications.

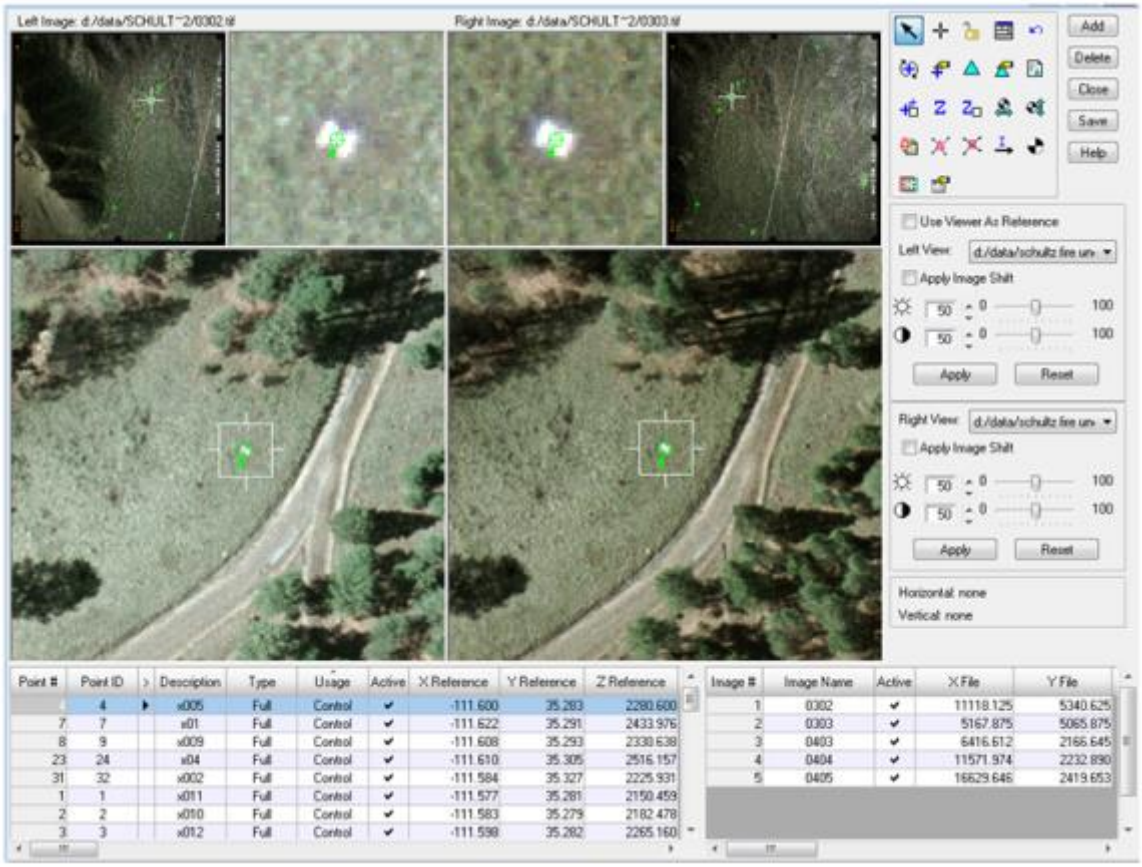

Figure 2.9 Dual display used to find control points and tie points found in the overlap area of two or more photos. Image 0302 (left) and image 0303 (right) are displayed and GCP x005 is identified on both image along with reference information.

Once all the initial points were established, automatic tie point generation was performed. Rather than manually identify additional tie points on the overlap areas, this process utilized digital image matching techniques to automatically identify and measure the image position of points appearing on two or more images with overlap (Leica Geosystems Geospatial Imaging, 2009). Since automatic tie point collection processes multiple images with overlap, LPS required information regarding image adjacency. Minimum input requirements were used to determine the block configuration with

respect to which image was adjacent to which image, and which strip was adjacent to which strip in the block. These inputs included either at least two GCPs measured on the overlap areas for the imagery in the block, or at least two tie points measured on the overlap areas of the imagery. Since numerous images did not contain at least two GCPs in the overlap area, I ensured that at least two tie points were measured on the overlap areas on adjacent imagery as well as those on adjacent flight lines.

Other strategy parameters governing the operation of the automatic tie point collection procedure could be used to optimize the performance of automatic tie point collection. These factors included search size (window size used to search for corresponding points), correlation size (window size for cross-correlation), least squares size (window size for least square matching), feature point density (feature point density percentage based on internal default), coefficient limit (threshold used to determine whether or not two points are to be considered as possible matches) and initial accuracy (relative accuracy of the initial values used by the automatic tie point generation process; Leica Geosystems Geospatial Imaging, 2009). These values could be adjusted to ensure the quality of the resulting tie points. Default values were used for correlation size (7 x 7), feature point density (100%), coefficient limit (0.80) and initial accuracy (10%). However, the value for search size was increased from 21 x 21 to 30 x 30 (increased for steeper areas) and least square size was decreased from 21 x 21 to 15 x 15 (decreased due to large degrees of topographic relief). Other values were tested, but did not produce the desired results.

Once additional tie points were generated, aerial triangulation could occur. Aerial triangulation is performed using a bundle block adjustment. This approach utilized an

iterative least squares solution. Based on the triangulation, the perspective center (X, Y, Z) and orientation (Omega, Phi, Kappa) of each image in the block as they existed at the time of capture were established (exterior information). A triangulation summary was generated which included a total unit-weight RMSE (0.8465). This standard deviation of unit weight is a global precision indicator describing the quality of the entire solution (Leica Geosystems Geospatial Imaging, 2009).

The final step in the process was the automatic extraction of terrain information and the creation of a DEM. As mentioned above, using a robust algorithm, LPS compared two images and looked for the image positions of conjugate features appearing in the overlap portion of the images. The three-dimensional position of the features in the block projection system was then computed. The results were exported as a DEM with a resolution of 3 m (although it could have been up to 0.17 m). For such a large area, a higher resolution would require much more processing time and memory. For this application, a Windows 7 Enterprise operating system with 64-bit color depth was used. This also included an Intel ® Core ™ 2 Duo CPU E8400 @ 3 GHz processor with 4 GB RAM and a 250 GB data drive.

These DEMs could then potentially be imported into a GIS for further analysis and also be used to orthorectify the associated imagery. This would remove the geometric distortion inherent in imagery caused by camera orientation, topographic relief displacement, and systematic errors associated with the imagery (Leica Geosystems Geospatial Imaging, 2009). These images would then be planimetrically true and represent ground objects in their true, real-work X and Y positions. This information

could also be mosaicked together and draped over the DEM to create a 3-dimensional map of the study area using the actual imagery from the study.

Although these high-resolution DEMs could be analyzed using a variety of applications, the results would be entirely dependent on the quality of this final product. As expected, this process was not entirely devoid of errors. As a result, it was crucial to investigate areas which contained obvious blunders and/or systematic biases to determine where the software generated erroneous DEM values.

2.3.3 Extended Study Area

Due to the availability of additional photos acquired from the original flight, I wanted to explore the feasibility of expanding the initial study area to incorporate a greater representation of the affected area. This included the northern section of the burn area as well as the lower residential communities below the fire. However, lack of available GCPs within this expanded photo area limited the software's ability to extract further terrain information. As a result, manual collection of natural or human-built features found in the images as they remained in the field provided an opportunity to expand this new study area.

On November 11, 2011, eight additional GCPs were collected (Table 2.4). These points were predominantly located along Route 89A, and within the lower residential area below the burn. Collection of further points in the higher elevations was unsuccessful due to snowy conditions resulting in closures along Forest Service roads up to Lockett Meadow and surrounding areas.

Table 2.4 GCPs from the November 11th, 2011 collection date. Green indicates the target was unable to be located on the photo and therefore was not used as ground control.

November 2011 Ground Control Points					
GCP ID	**Longitude (X)**	**Latitude (Y)**	**Elevation (Z)**	**Lat DD**	**Long DD**
GC01	111:33:17.24039 W	35:18:07.37669 N	2057.828 m	35.30204908	-111.554789
GC02	111:32:33.40590 W	35:17:14.90104 N	2029.682 m	35.28747251	-111.5426128
GC03	111:32:55.88321 W	35:18:30.38248 N	2033.955 m	35.30843958	-111.5488565
GC04	111:32:43.59683 W	35:19:42.84365 N	2043.762 m	35.32856768	-111.5454436
GC05	111:34:06.02652 W	35:21:08.64906 N	2169.727 m	35.35240252	-111.5683407
GC06	111:34:34.54342 W	35:22:19.71737 N	2184.962 m	35.37214371	-111.5762621
GC07	111:33:28.62974 W	35:20:26.04444 N	2097.137 m	35.3405679	-111.5579527
GC08	111:33:06.87222 W	35:16:20.63018 N	2038.176 m	35.27239727	-111.551909

Before going out in the field, I went through the imagery and found features that could potentially be located on the ground. This included objects such as downed trees, corners of cattle guards, painted objects on the road, and any other object that would be easily locatable while out in the field. As long as these features had not changed since photo acquisition (over a year before), the coordinates of these points could be used to expand the study area.

Much like the original GCPs, I obtained the coordinates (X, Y, and Z) of these eight additional locations using DGPS surveying techniques. This process involved the cooperation of two receivers; one that was stationary (base) and another that was roving (rover) making positional measurements (Figure 2.10). The stationary receiver was used as a solid location reference, and helped eliminate any error experienced by the receivers in relation to the signal traveling through space.

The specific equipment, TOPCON GR-3, was a triple constellation receiver capable of picking up multiple signals from GPS (USA), Glonass (Russia), and Galileo (Europe) navigation satellites. Depending on the distance from the base, I used a static occupancy of 10-15 minutes for each location. This data was then post-processed, yielding sub-meter accuracy for the measured locations (Appendix 6.4).

Figure 2.10 The base (left) and rover (right) receivers used to determine coordinates of additional GCPs in the field.

Collection of additional points was again delayed due to construction along forest roads resulting in closures in the affected area. On September 14, 2012, the roads officially re-opened and I was able to collect the final GCPs in the burn area. Over the span of two days (October 25th and 28th), a total of 21 points were collected (in addition to the 8 from the previous year) and were used to expand the initial study area (Table 2.5).

Table 2.5 GCPs from the October 25th/28th, 2012 collection dates. Green indicates the target was unable to be located on the photo and therefore was used as an elevation check point rather than ground control.

October 2012 Ground Control Points					
GCP ID	**Longitude (X)**	**Latitude (Y)**	**Elevation (Z)**	**Lat DD**	**Long DD**
1	111:32:59.76329 W	35:17:11.97585 N	2051.638 m	35.28665996	-111.5499343
2	111:33:22.88053 W	35:22:19.69593 N	2107.058 m	35.37213776	-111.5563557
3	111:37:16.29324 W	35:21:42.56110 N	2573.273 m	35.36182253	-111.6211926
4	111:36:43.99315 W	35:21:24.48671 N	2637.871 m	35.35680186	-111.6122203
5	111:37:23.55735 W	35:21:00.76695 N	2782.293 m	35.35021304	-111.6232104
6	111:37:06.98857 W	35:22:09.57064 N	2560.912 m	35.36932518	-111.6186079
7	111:36:44.27825 W	35:22:39.77304 N	2480.72 m	35.37771473	-111.6122995
8	111:36:22.60766 W	35:22:45.85783 N	2429.732 m	35.37940495	-111.6062799
9	111:36:37.12612 W	35:21:00.04125 N	2595.402 m	35.35001146	-111.6103128
10	111:36:00.05068 W	35:21:04.36004 N	2445.226 m	35.35121112	-111.6000141
11	111:35:19.75103 W	35:21:21.77728 N	2324.245 m	35.35604924	-111.5888197
12	111:36:01.53036 W	35:22:23.76049 N	2325.876 m	35.3732668	-111.6004251
13	111:35:22.55950 W	35:22:45.71100 N	2238.239 m	35.37936417	-111.5895999
14	111:35:01.01403 W	35:22:09.62790 N	2233.252 m	35.36934108	-111.583615
15	111:34:35.06204 W	35:21:41.45381 N	2218.021 m	35.36151495	-111.5764061
16	111:34:29.08974 W	35:20:45.77219 N	2224.772 m	35.34604783	-111.5747472
17	111:35:19.10472 W	35:20:07.35586 N	2285.73 m	35.33537663	-111.5886402
18	111:35:34.50256 W	35:20:07.26909 N	2356.891 m	35.33535253	-111.5929174
19	111:35:27.55689 W	35:18:16.73263 N	2253.856 m	35.30464795	-111.590988
20	111:34:07.11722 W	35:16:44.46550 N	2112.855 m	35.27901819	-111.5686437
21	111:33:23.60506 W	35:16:42.84448 N	2068.883 m	35.27856791	-111.556557

Again, using DGPS equipment, features were located in the field which would not have changed in the time since the photos were acquired (two years before). This could include stable, natural features such as large boulders or fallen logs, or man-made structures such as cattle guards (Figure 2.11). Using rough estimates for latitude and longitude, possible points were first located on the images that would be easily accessible in the field. This proved more difficult than expected as many of the chosen locations were not able to be located. As a result, new objects were located and based on the amount of open space above and around, were used as new points.

Figure 2.11 Example of a natural feature (boulder; left) and a man-made feature (trough; right). The features were measured in the field then located on the images to be used as GCPs.

Once all the additional points were collected, the data was post-processed and the locations could be used as GCPs in LPS. A total of seven points could not be located on the images and as a result were not used as control. This brought the total number of GCPs for the entire area (including original, Nov 2011 and Oct 2012 points) to 41 (Figure 2.12). A total of 46 images were included in this expanded area (0101-0111, 0201-0211, 0302-0313 and 0403-0414) and included four different flight strips.

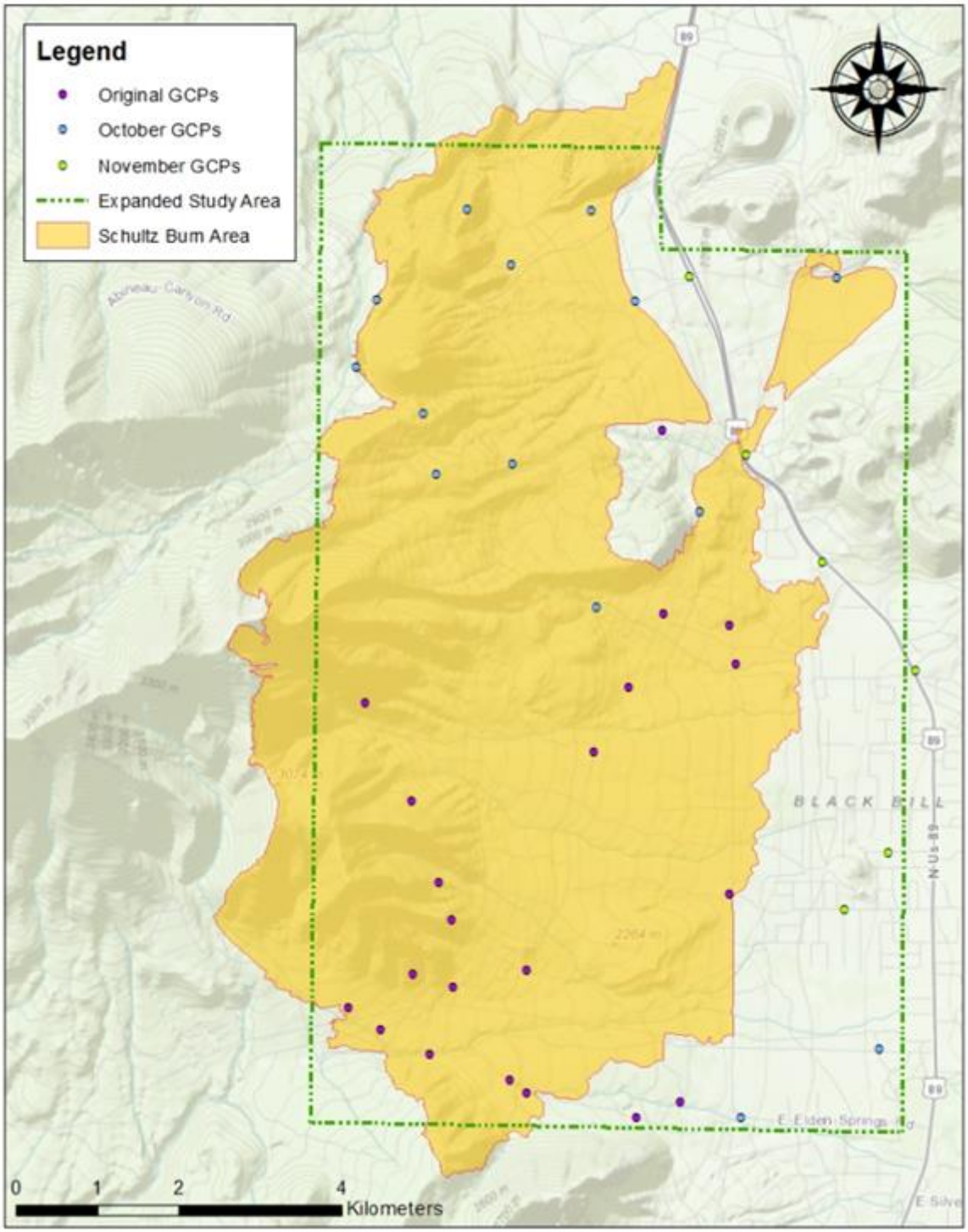

Figure 2.12 Location of the expanded study area. This area was based on the location of original GCPs (purple) as well as the collection of additional GCPs in the affected area during November 2011 (green) and October 2012 (blue).

Following the same procedure as the initial study area, LPS was used to generate a 3 m DEM of the expanded area. In addition to the original study area, this included the northern section of the burn as well as the lower residential areas that were impacted by the flooding. Although there were sections of the burn that were not represented in the expanded DEM, the overall extent included most of the affected area which was a major improvement over the original DEM. However, there were still sections within the study area where GCPs were unable to be collected, and as a result, limited the software's ability to extract accurate elevation data in these locations.

Similar to the original results, this expanded DEM also contained areas of obvious blunders. To determine where these blunders were occurring, a 10 m DEM from the USGS was used to compare the results. This included looking at slope, elevation, aspect, and burn severity variables to determine if there are correlations between these factors and where the blunders were occurring. Additionally, this information was used to determine if there are systematic biases in the DEM once the known blunders were removed. Based on the results, the accuracy of the expanded area DEM was evaluated.

2.4 Results

The original 3 m DEM that was generated by LPS covered an area of 3513 ha and ranged in elevation from 2083 m to 3236 m (Figure 2.13). Visually, there were obvious blunders in the higher elevations, especially in the mountainous regions along the western edge of the study area. These blunders appeared very coarse and pixelated, and could have been a result of issues with the software (such as poor image matching) that limit its ability to extract accurate data from these types of data.

Other areas of the DEM seemed to be correctly represented, especially along the areas of minimal relief variation east of the mountainous slopes. Even with the blunders, these results could potentially be used in preliminary studies measuring land changes as a result of the fire and flooding. However, a major constraint with this data was that the extent was again very limited to the southern portion of the burn area.

As a result of the successful collection of additional GCPs, this area was expanded to include a greater representation of the affected landscape (Figure 2.14). This expanded 3 m DEM covered an area of 8365 ha, which was approximately 2.4 times larger than the original study area, and ranged in elevation from 2023 m to 3287 m. However, much like the original DEM, the results contained areas of obvious blunders. Again, these seemed to be located mostly in the mountainous areas along the western edge of the study area.

Due to the consistency of blunder locations between the original DEM and the expanded DEM, only the expanded area was used when determining factors that may have had an effect on the accuracy of the resultant DEM. This process involved comparing the results of the generated DEM to a reference DEM to determine the areas containing blunders. By subtracting the two different DEMs, it was possible to find discrepancies in the data (both lower and higher) to determine exactly where the major blunder areas were occurring.

Once the blunder areas were identified, these areas could be examined further to determine factors that may have affected these results. This could include differences in slope, elevation, aspect, or burn severity. These blunder areas could also be removed to determine bias between the two DEMs that were compared.

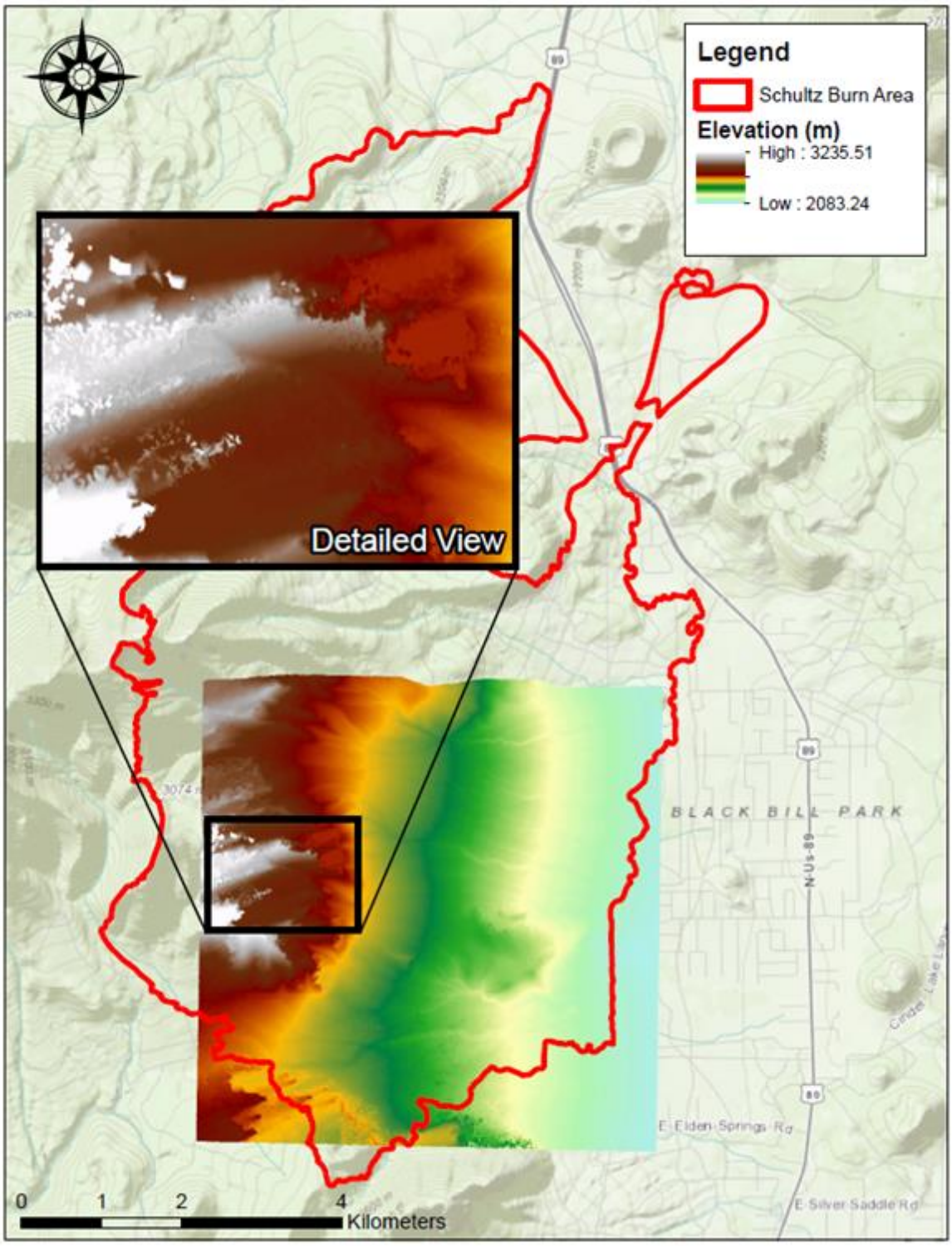

Figure 2.13 Results from the original study area DEM. The detailed view provides a closer look at an obvious blunder area. These blunder areas were typically located along the western edge in the mountainous regions of the study area.

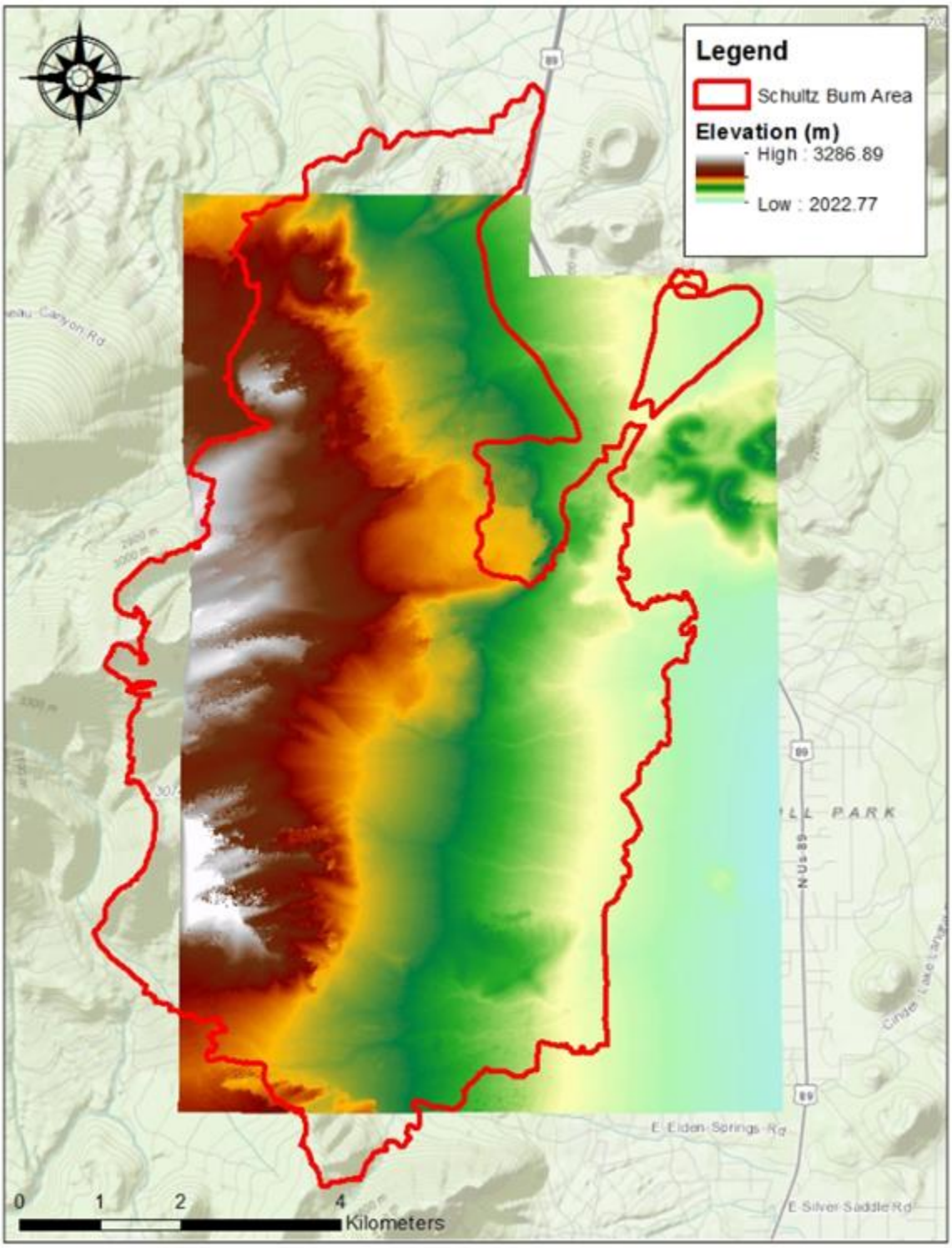

Figure 2.14 Results from the expanded study area DEM. This area covered approximately 2.4 times the original study location and included a greater representation of the area affected by the fire and flooding.

For the reference DEM, I used the National Elevation Dataset (NED), which is the primary elevation data product of the USGS (Figure 2.15). The 10 m DEM obtained for the study area consisted of seamless data devoid of errors. However, due to undulations of the geoid, a value of 22.9 was subtracted from these elevation values to match the surface of the expanded DEM. This correction was based on the GEOID03 model and was determined by the extent of the expanded study area.

Although this type of DEM is publicly available for download, it is often limited to resolutions of 10 m or 30 m, as well as in how often it is updated. This provided just one indication into the importance of the newly created DEMs of the study area, especially in terms of the ability to obtain higher resolutions (up to 17 cm) and the potential to update the data as needed. However, blunder areas are a major concern.

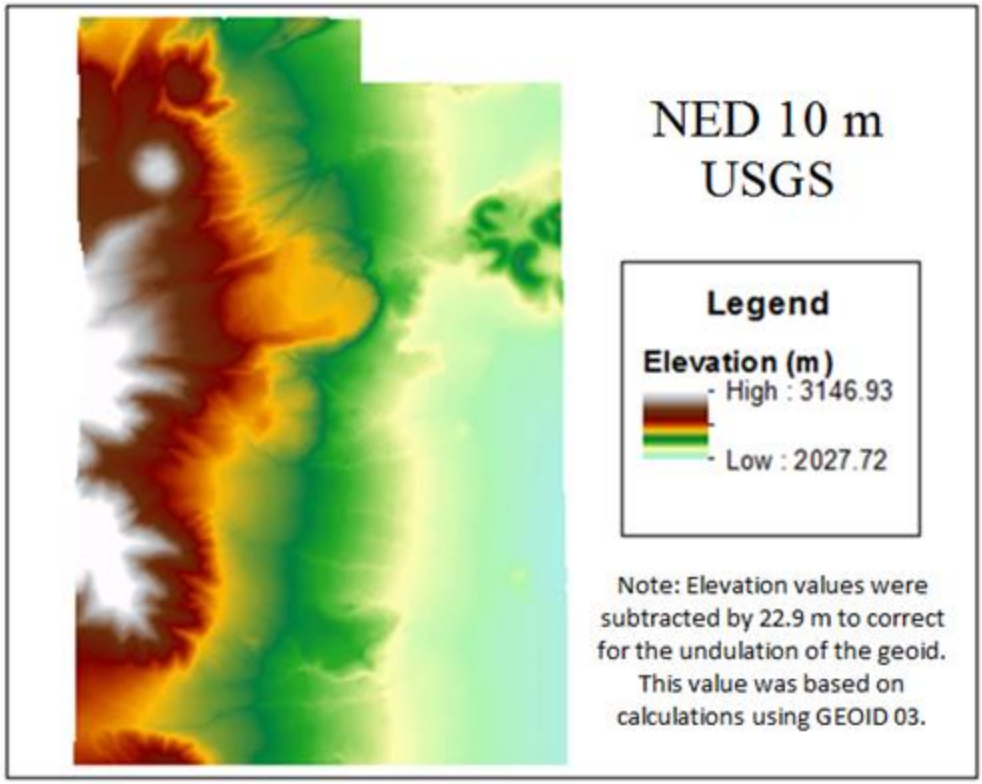

Figure 2.15 The 10 m DEM used as the reference when comparing differences in elevation to the expanded study area DEM.

To determine differences between the two DEMs, I subtracted the reference DEM from the expanded area DEM (Figure 2.16). Negative values (blue) indicated areas in the expanded DEM that were lower than the reference DEM while positive values (red) indicated areas that were higher than the reference DEM. These values ranged from -421.754 m to 308.557 m. As expected, major blunder areas were focused primarily on the western edge of the study area and a majority of these areas consisted of lower values. The rest of the area contained much smaller variances, indicating slight biases between the DEMs.

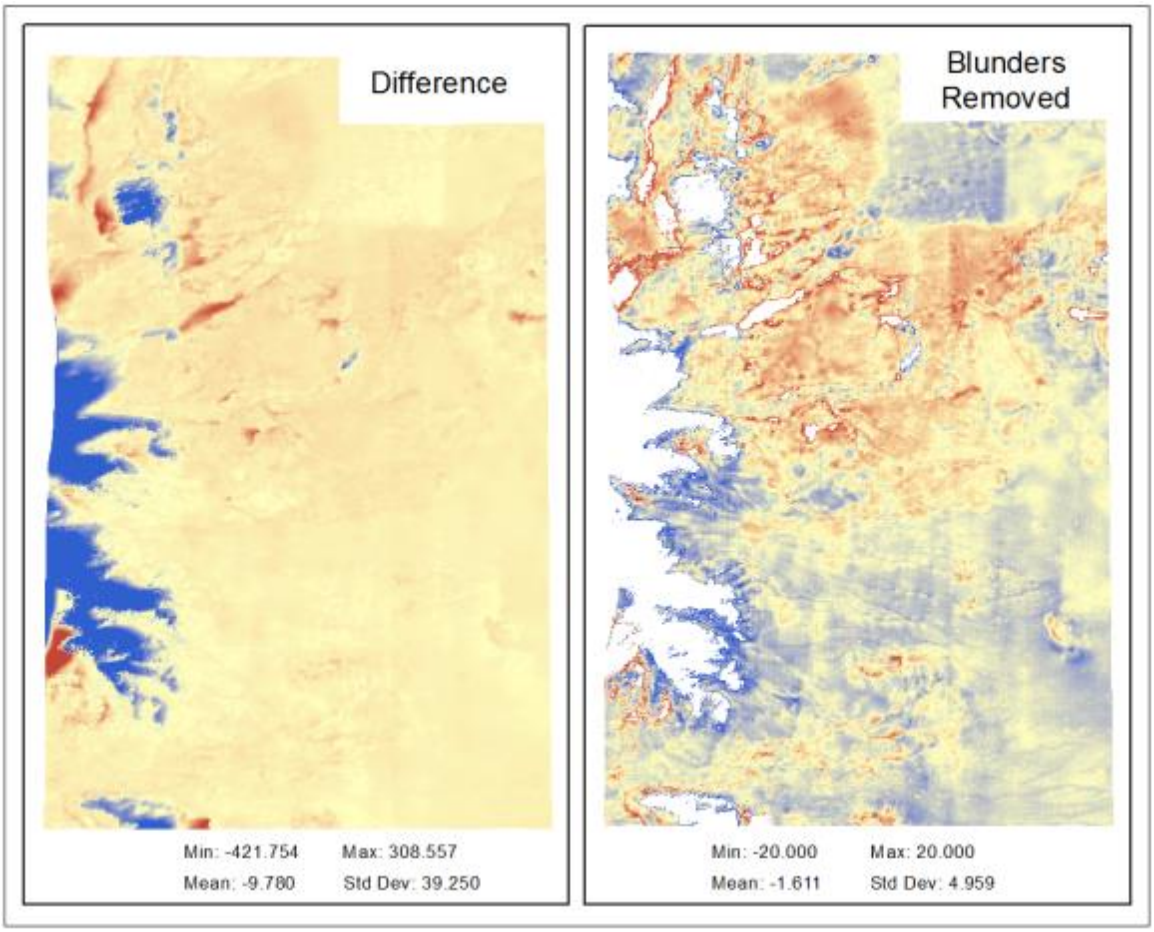

Figure 2.16 The difference between the reference DEM and the expanded area DEM (left). Blue indicated values in the expanded DEM that were lower than the reference DEM while red indicated values that were higher than the reference DEM.

Using approximately half a standard deviation from zero (±20), values above and below this extent were classified as major blunders in the expanded DEM. This value was chosen based on the positive kurtosis (18.68; Leptokurtic) indicating a high degree of peakedness. Differences less than -20 m were considered low blunders (values were far lower than the reference data) while differences greater than 20 m were considered high blunders (values were far higher than the reference data). Values between this extent (-20 m to 20 m) were not considered blunders, but rather were determined to indicated bias between the two DEMs (Figure 2.17). Different factors were then used to determine mean elevation differences as well as mean proportion of blunders for the expanded area DEM.

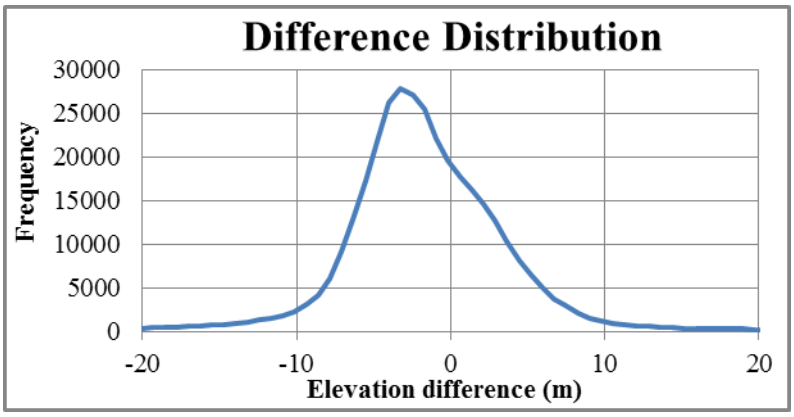

Figure 2.17 Elevation difference distribution between the two DEMs. Values above and below ±20 were considered blunders and removed from the data. Overall, there tends to be a negative bias (mean elevation difference = -1.611).

Using the reference DEM, slope, elevation, and aspect were determined and the values were reclassified into distinct classes. Burn severity data was also analyzed, but was unrelated to the reference DEM. Zonal statistics were then used to look at blunder areas (high and low) as well as biases between the DEMs based on each of the different variable classes to explore potential systematic pattern in the distribution of DEM inconsistencies.

The first two factors that were examined were slope and elevation (Figure 2.18). Slope values were reclassified into nine classes and increased by increments of 5%, except for the last class which combined the last three due to the limited presence of slopes greater than 40% within the study area. Elevation was reclassified into eight classes and increased by increments of 150 m.

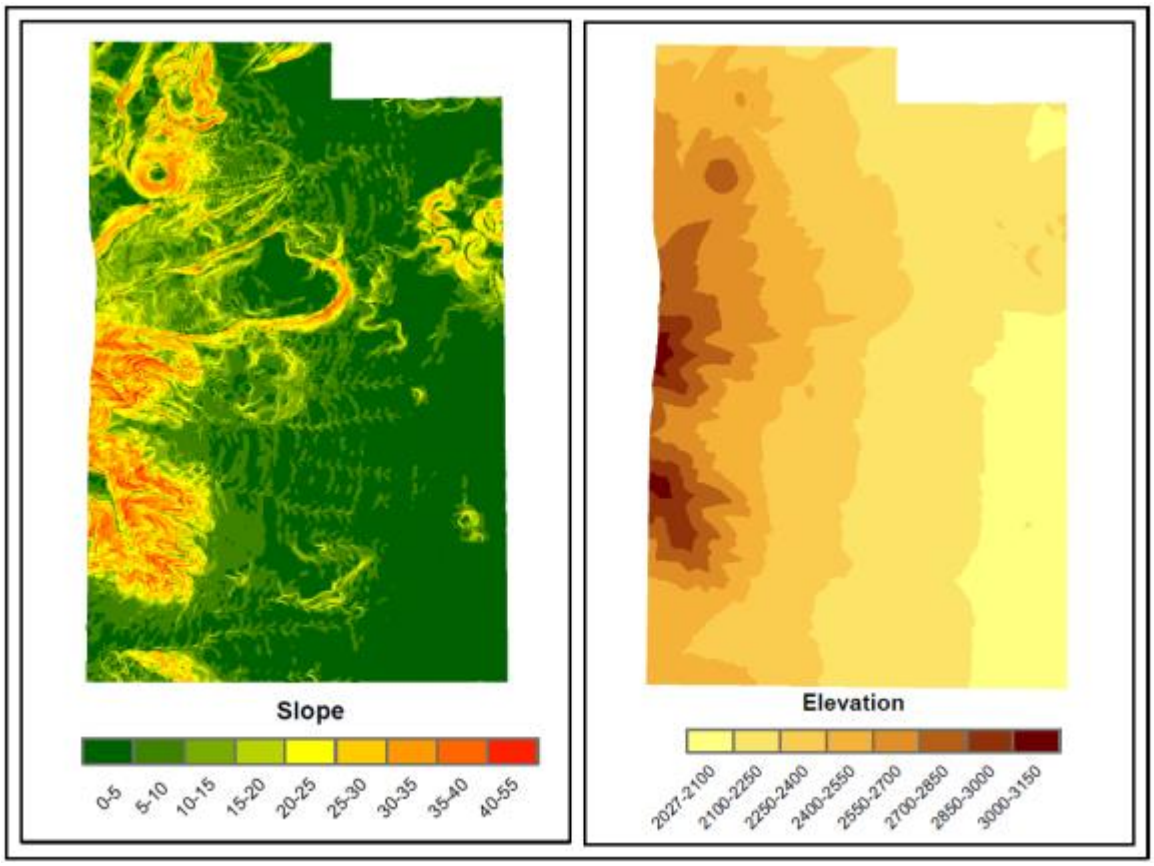

Figure 2.18 Reclassified values for slope (left) and elevation (right) based on the reference DEM.

The next two factors were aspect and burn severity (Figure 2.19). Aspect was reclassified into five classes (N, NE, E, SE and S) and did not include western facing slopes (W, NW and SW). These slopes only made up about 6% of the entire study area, with a majority being eastern (41%), southeastern (19%) and northeastern (17%) facing

slopes. As a result, these western slopes were removed so the results would not be skewed due to limited sample size. Burn severity data was already classified as distinctive classes including very low/unburned (VL), low (L), moderate (M) and high (H) so did not need to be reclassified. This only included information from within the burn, and did not include areas outside the perimeter.

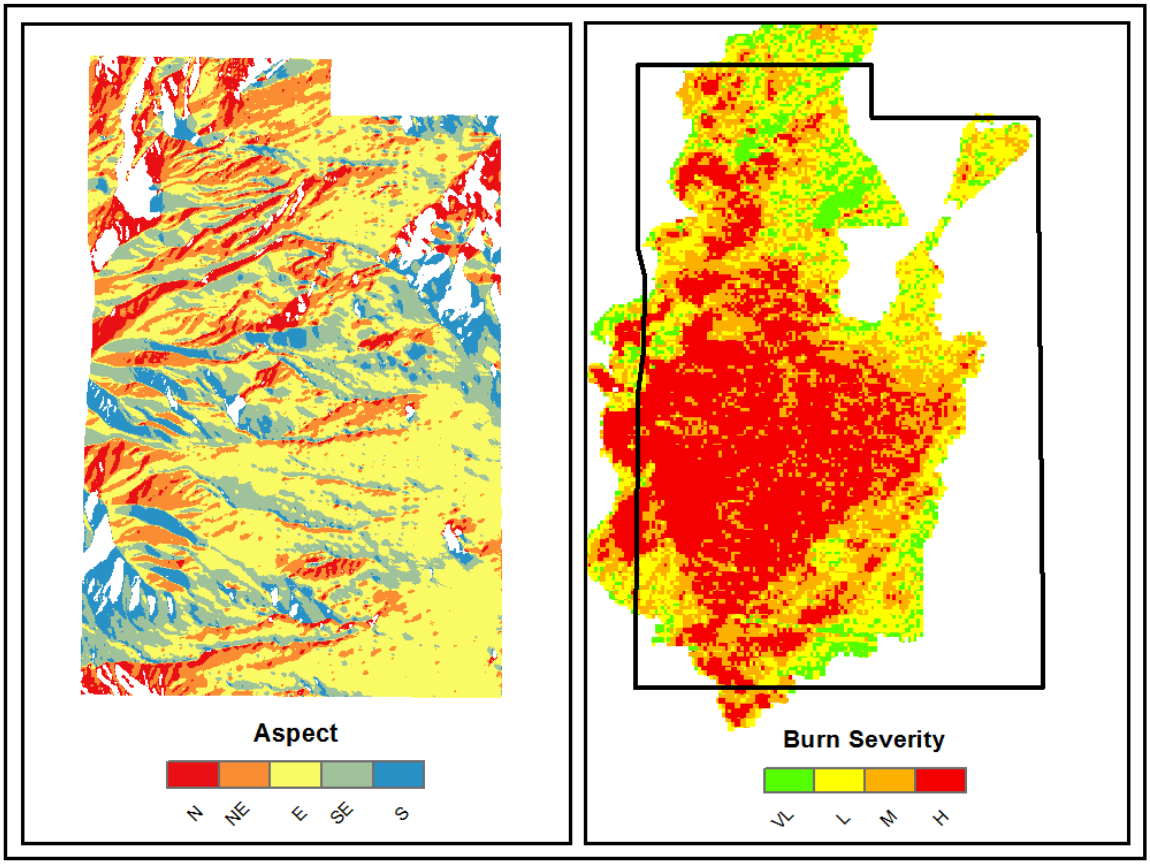

Figure 2.19 Reclassified values from aspect (left) and burn severity (right).

The next step involved computing zonal statistics for each of the different classes. With zonal statistics, a statistics is calculated for each zone (class) based on the values from another dataset. In this case, the four factors (slope, elevation, aspect and burn severity) were compared against the layer where the blunders were removed (Table 2.6), as well as the layer that contained the high and low blunders (Table 2.7).

Table 2.6 Zonal statistics which determined mean elevation difference as well as standard deviations for slope (A), elevation (B), aspect (C) and burn severity (D).

A) Slope – Blunders Removed				
VALUE	**SLOPE**	**MEAN**	**STD**	**COUNT**
1	0-5	-1.9812	3.543896	357966
2	5-10	-0.94551	4.412118	174972
3	10-15	-0.81509	5.707876	75737
4	15-20	-1.30001	6.947268	44881
5	20-25	-1.83925	7.953698	32890
6	25-30	-2.61529	8.566173	22477
7	30-35	-3.1874	9.057444	11413
8	35-40	-4.32635	9.252083	3446
9	40-55	-6.6676	8.929877	835

B) Elevation – Blunders Removed				
VALUE	**ELEVATION**	**MEAN**	**STD**	**COUNT**
1	2027-2100	-3.27305	2.107466	109253
2	2100-2250	-1.43852	3.963552	279033
3	2250-2400	-0.55169	4.88614	173447
4	2400-2550	-1.8424	6.823494	98304
5	2550-2700	-1.43911	7.349099	50622
6	2700-2850	-4.03865	7.84863	12559
7	2850-3000	-7.15863	9.194691	1108
8	3000-3150	-12.2127	2.165361	291

C) Aspect – Blunders Removed				
VALUE	**ASPECT**	**MEAN**	**STD**	**COUNT**
1	N	0.757562	6.017828	51490
2	NE	-0.57499	5.436751	114723
3	E	-2.24409	4.026243	311650
4	SE	-2.25614	4.603161	145939
5	S	-3.00449	5.723807	54774

D) Burn Severity – Blunders Removed				
VALUE	**SEVERITY**	**MEAN**	**STD**	**COUNT**
1	Very Low/Unburned	-0.686	4.643621	3480
2	Low	-0.79042	5.276166	11997
3	Moderate	-0.16535	4.63158	10418
4	High	-2.66223	5.604695	14492

Table 2.7 Zonal statistics which determined mean proportion of blunders as well as standard deviations for slope (A), elevation (B), aspect (C) and burn severity (D).

A) Slope Blunders			High Blunder		Low Blunder	
VALUE	SLOPE	COUNT	MEAN	STD	MEAN	STD
1	0-5	359034	0.000947	0.030759	0.002028	0.044984
2	5-10	178792	0.008524	0.091931	0.012842	0.112591
3	10-15	83419	0.025402	0.157342	0.066687	0.24948
4	15-20	55603	0.042768	0.202333	0.150064	0.357134
5	20-25	46983	0.063065	0.243081	0.236894	0.425177
6	25-30	42542	0.065817	0.247963	0.405834	0.491053
7	30-35	28274	0.063168	0.243264	0.533175	0.498898
8	35-40	10659	0.068393	0.252419	0.608312	0.488128
9	40-55	2036	0.053536	0.2251	0.536346	0.498677

B) Elevation Blunders			High Blunder		Low Blunder	
VALUE	ELEVATION	COUNT	MEAN	STD	MEAN	STD
1	2027-2100	109253	0	0	0	0
2	2100-2250	279633	0.002099	0.045769	4.65E-05	0.006818
3	2250-2400	176784	0.013276	0.114455	0.0056	0.074624
4	2400-2550	115462	0.048033	0.213836	0.10057	0.300758
5	2550-2700	72625	0.052558	0.223149	0.25041	0.433249
6	2700-2850	36939	0.060478	0.238371	0.599529	0.489994
7	2850-3000	13673	0.015724	0.124407	0.90324	0.295631
8	3000-3150	2973	0.000673	0.025928	0.901446	0.298062

C) Aspect Blunders			High Blunder		Low Blunder	
VALUE	ASPECT	COUNT	MEAN	STD	MEAN	STD
1	N	65284	0.03039	0.171659	0.180902	0.384937
2	NE	138579	0.013379	0.11489	0.158769	0.36546
3	E	329042	0.005723	0.075432	0.047134	0.211925
4	SE	156957	0.010685	0.102812	0.059513	0.236583
5	S	61070	0.016653	0.127968	0.086442	0.281015

D) Burn Severity Blunders			High Blunder		Low Blunder	
VALUE	SEVERITY	COUNT	MEAN	STD	MEAN	STD
1	Very Low/Unburned	3685	0.008955	0.094207	0.046676	0.210943
2	Low	13348	0.031091	0.173563	0.070123	0.255354
3	Moderate	11077	0.012549	0.111315	0.046944	0.211519
4	High	18830	0.020765	0.142596	0.209612	0.407032

The mean values were then graphed to visually represent the relationship between these conditions and the location of the blunders, as well as determine biases when the blunders were removed (Figure 2.20-2.23). For the mean elevation difference, upward trends indicated more biased and error prone surfaces. Similarly, for mean proportion of blunders, higher values indicated more blunders (a value of 1 indicated blunder while a value of zero 0 indicated no blunder).

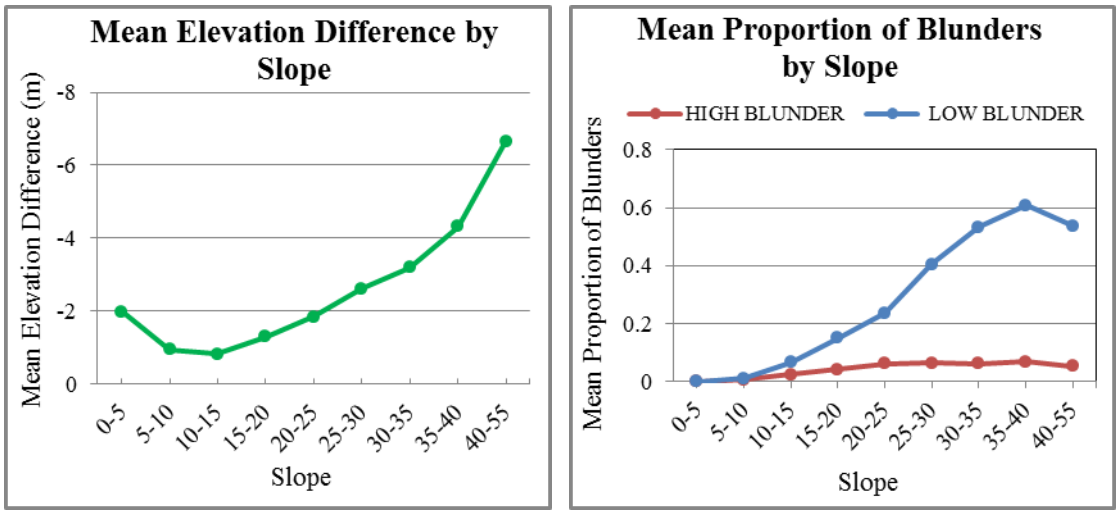

Figure 2.20 Mean elevation difference (left) and mean proportion of blunders (right) by slope.

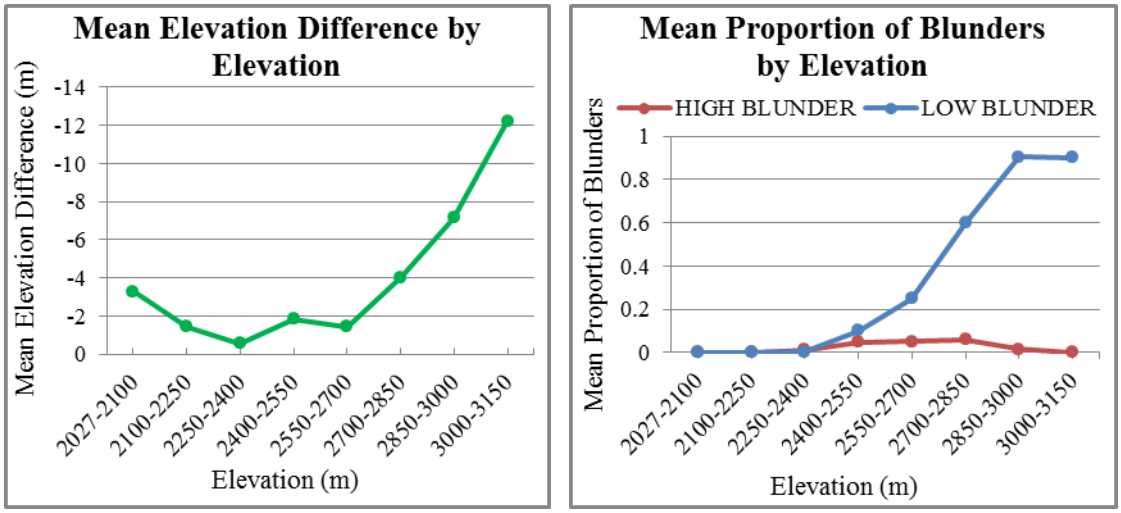

Figure 2.21 Mean elevation difference (left) and mean proportion of blunders (right) by elevation.

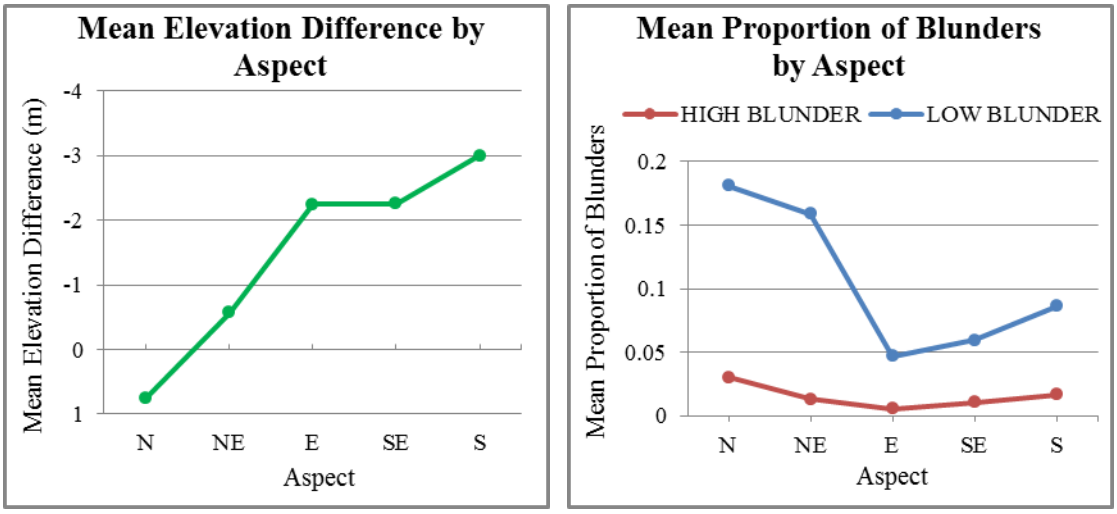

Figure 2.22 Mean elevation difference (left) and mean proportion of blunders (right) by aspect.

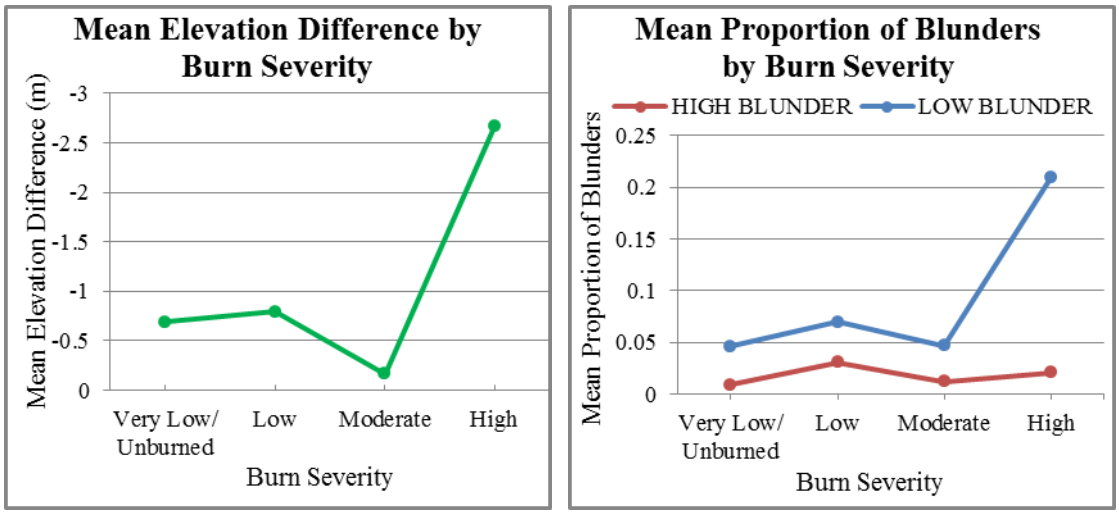

Figure 2.23 Mean elevation difference (left) and mean proportion of blunders (right) by burn severity.

In addition to looking at factors which may have affected the accuracy of the DEM, GCPs that were unable to be located on the images were used as elevation check points to assess the accuracy of the generated DEM (Figure 2.24). Using the coordinates from each of location, I was able to extract the elevation information from the generated DEM. The difference between the measured elevation data and extracted elevation data could then be compared (Table 2.8).

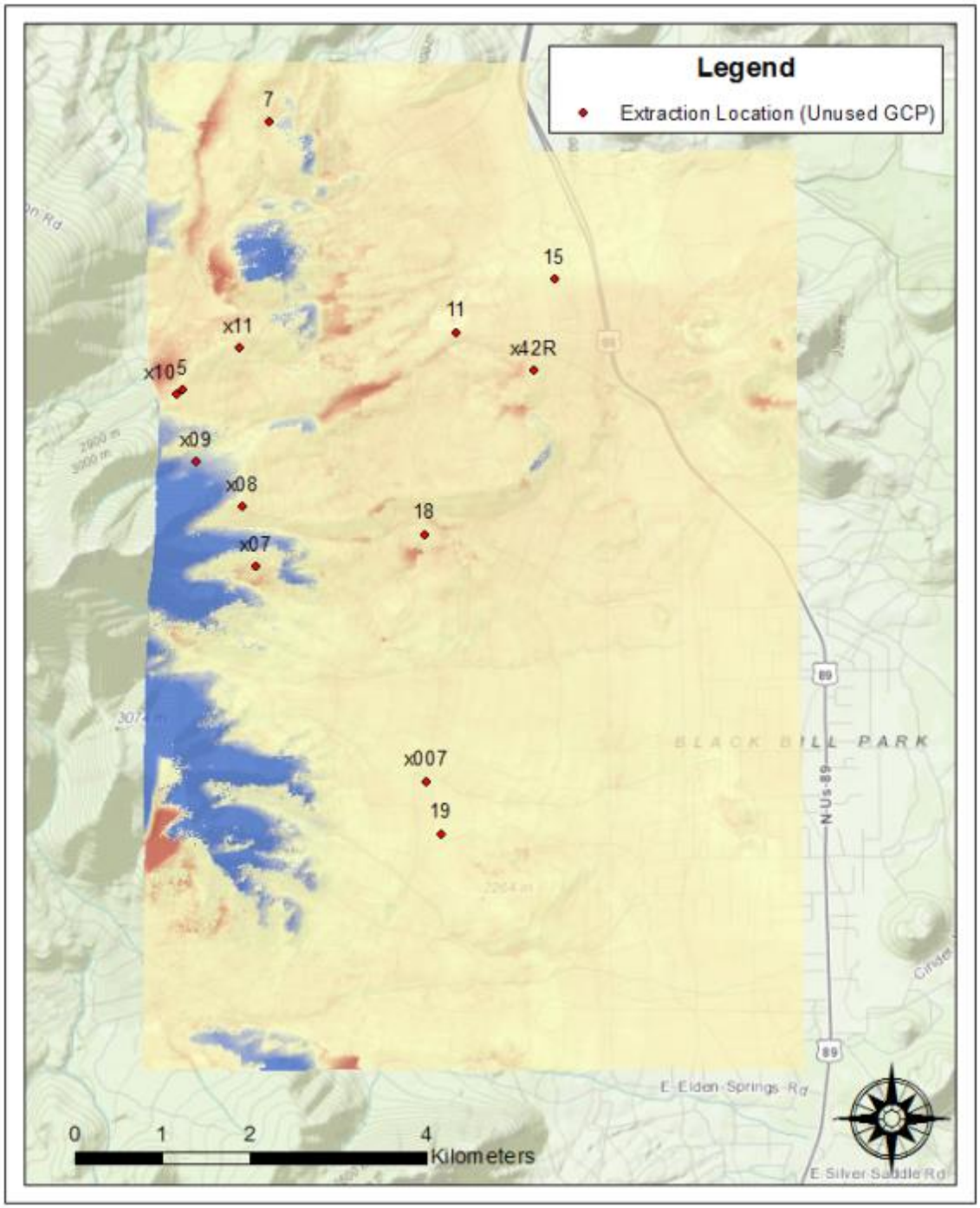

Figure 2.24 Unused GCPs which were unable to be located on the images and were instead used as check points to access the accuracy of the DEM. Of the 16 unused GCPs, three were unable to be included as check points due to their locations.

Table 2.8 Values of the measured GCP elevations as well as elevations extracted from the DEM. These values were used to calculate absolute error as well as percent error for each of the points.

Difference in Elevation Between Measured and Extracted Values				
ID	**Measured Values (m)**	**Extracted Values (m)**	**Absolute Error**	**Percent Error**
x007	2264.013	2263.674	0.339	0.015%
x042R	2268.823	2268.925	-0.102	0.004%
x07	2697.832	2697.866	-0.034	0.001%
x08	2735.636	2735.221	0.415	0.015%
x09*	2761.831	2692.691	69.14*	2.503%
x10	2796.692	2795.624	1.068	0.038%
x11	2682.824	2682.603	0.221	0.008%
5	2782.293	2781.126	1.167	0.042%
7	2480.720	2478.054	2.666	0.107%
11	2324.245	2324.031	0.214	0.009%
15	2218.021	2214.007	4.014	0.181%
18	2356.891	2355.750	1.141	0.048%
19	2253.856	2252.836	1.02	0.045%

From this information, absolute error and percent error could be calculated for each point. A positive absolute error indicated that the extracted elevations were lower than the measured values while a negative value indicated that the extracted elevations were higher than the measured values. A RMSE of 19.232 was then determined based on these values. However, the absolute error from point x09 was 69.14 m which indicated a major blunder. As a result, this value was removed and a RMSE of 1.540 was obtained when recalculating these values. This indicated that the difference between these values was very low, and overall, the DEM was accurate in relation to these points.

2.5 Discussion

Overall, results demonstrate that the digital photogrammetric software program ERDAS Imagine LPS can be used to generate complex terrain affected by fire and flooding. This data can be obtained at exceedingly high rates when compared to other photogrammetric methods (such as older manual techniques), and at relatively low costs

when compared to non-photogrammetric methods (such as LiDAR). The resultant DEMs also contained much higher resolutions than publicly accessible DEMs available for download (such as 10 m from the USGS) and also have the potential to be updated as needed. However, there were also drawbacks and limitations to this specific software which may have affected the overall accuracy of the generated DEMs. This included obvious blunder areas along the mountainous region, as well as slight biases when compared to a reference DEM. As a result, it is important to recognize these potential limitations, especially for future studies on similar terrain affected by fire and flooding.

Based on the results from the zonal statistics, the different factors could be used to determine how these conditions affected the accuracy of the resultant DEM. For slope, the smallest mean proportion of blunders occurred in flatter areas, while the largest mean proportion of blunders occurred in steeper areas. This was likely due to geometric distortions between the image pairs, as well as the occurrence of parallax; the apparent displacement of an observed object due to a change in the position of the observer. It was much more difficult to identify congruent objects on two or more overlapping images due to the observable difference in object appearance on steeper slopes. Similarly, for elevation, the smallest mean proportion of blunders occurred in lower elevations while the largest mean proportion of blunders occurred in higher elevations. Again, this was most likely a result of higher elevations experiencing greater differences in object appearance (higher elevations usually contain areas of steeper slopes). This could have also been a result of different vegetation cover at different elevations, with lower elevations containing less dense areas of vegetation (more open areas) and higher elevations containing more dense areas of tree cover.

For aspect, the smallest mean proportion of blunders occurred on the eastern and southern facing slopes while the largest mean proportion of blunders occurred on the northern facing slopes. This may have been a result of northern facing slopes experiencing more shadowed areas based on the angle of sun at the time of image capture. These areas may have been too shaded to differentiate between similar features, ultimately leading to higher occurrences of blunders in these areas. Finally, the smallest mean proportion of blunders for burn severity occurred in areas of very low/unburned or moderate burn severities while the largest proportion of blunders occurred in areas of high severity. This was most likely a result of areas experiencing low contrast due to the absence of trees or other protective cover, ultimately overexposing these areas.

All of these conditions help indicate possible areas where the software had a difficult time extracting accurate elevation data, resulting in areas of obvious blunders. For the most part, these conditions (higher elevations, steeper slopes, northern facing slopes and high burn severities) indicate that more complex terrain produces less accurate results. These areas also tended to have very limited ground control, which may have also added to the inability for the software to extract accurate elevation information from these locations.

Similar to mean proportion of blunders, measuring the degree of bias was very comparable. For slope, the smallest mean elevation difference occurred in flatter areas, while the largest mean elevation difference occurred in steeper areas. For elevation, the smallest mean elevation difference occurred in lower elections while the largest mean elevation difference occurred in higher elevations. For aspect, the smallest mean elevation difference occurred on northern facing slopes (N and NE) while the largest

mean elevation difference occurred on southern facing slopes. Finally, for burn severity, the smallest mean elevation difference occurred on the lower burn severities (with the lowest being moderately burned), while the largest mean proportion of blunders occurred in the high burn severity. However, rather than issues with the software, the amount of bias was more likely attributed to user set properties, which may have affected the overall DEM accuracy, producing higher or lower elevations than the reference DEM.

For future studies (whether on the Schultz burn or similar areas), all of these conditions must be considered when deciding whether to use LPS or another similar photogrammetric product to produce DEMs of affected areas. Again, results indicate that LPS had a more difficult time generating accurate results in more complex terrain where GCP cover was limited. Many of the GCPs used for this study were located in open areas next to Forest Service roads that transverse most of the study area. However, there were still areas that were inaccessible, and adequate GCP cover was not possible. Similar studies may be more remote (no roads) , and adequate GCP cover may be difficult, if not unachievable. Fires also typically occur in more complex terrain (such as on steeper slopes) and use of LPS may not be desirable. As a result, it is important to identify the type of terrain as well as achievable GCP before staring a project in LPS.

2.6 Conclusion

ERDAS Imagine LPS provided a feasible way of analyzing high accuracy terrain data following a high severity wildfire. This included the original area using pre-marked GCPs as well as the extended area using post-marked GCPs that were collected two years after the imagery was acquired. In both DEMs, obvious blunders tended to be located in the mountainous regions along the western edge of the study area. By isolating and

removing these blunder areas, the overall accuracy of the DEMs were greatly increased. This was apparent when an elevation check point in the blunder area was removed and the RMSE was reduced from 69.14 to 1.540.

Zonal statistics were also used on the isolated blunder areas as well as the DEM with the blunder areas removed to determine potential factors which decreased the accuracy of the DEM. These included areas in higher elevations, steeper slopes, northern and southern facing slopes and high burn severities. These typically indicated areas of more complex terrain, and were typically located in areas where GCP cover and tie point cover was limited. Smaller differences (bias) were most likely a result of user specified parameters, resulting in slightly higher or slightly lower elevations when compared to the reference DEM.

Finally, it is important to mention that factors from this study are very limited to the Schultz Fire, and additional studies are needed to accurately analyze the results. This includes the fact that a majority of the slopes were eastern facing (77%), as well as numerous other factors. In conclusion, although LPS provided feasible results for studying the Schultz Fire burn area, more studies are needed to determine how different conditions could affect the accuracy of a similar area affected by fire and flooding.

3. Comparing Schultz Burn Area Terrain Data Derived From Two Photogrammetric Software Programs

3.1 Abstract

The aim of this study was to compare two digital photogrammetric software programs (ERDAS LPS, 2010 and PCI Geomatica OrthoEngine, 2013) and check their performance regarding automatic digital elevation model (DEM) extraction in a complex geomorphological setting. Specifically, these systems were used to compare an area which consisted of the overlap of two aerial photos within a high-severity area of the Schultz Fire burn area. The procedure for generating the DEMs is described, and the benefits and limitations of each system are highlighted. The resultant DEMs were compared by differencing the data sets as well as generating profile graphs of various locations and analyzing the results. Overall, LPS tended to produced more systematic errors, but the system was much more flexible, especially in its ability to extract elevation information over smaller-scale topographic features when compared to OrthoEngine.

3.2 Introduction

Digital elevation models (DEMs) play an important role for observing and measuring landscape changes involved with geomorphological studies. These models require high resolution quantitate terrain data to document topographic changes, and traditionally have been acquired through the process of photogrammetry. In particular, digital aerial photogrammetry is a powerful tool in surface model generation, and is able to extract high resolution DEMs by means of automated image matching procedures (Fabris and Pesci, 2005). Developments in digital photogrammetry have provided

geomorphologists with an automated tool to generate DEMs at exceedingly high densities.

Software to carry out the photogrammetric processing is now available commercially at competitive rates (Chandler, 1999). Some of more recent digital photogrammetry software programs include BAE Systems SOCET SET, ERDAS Imagine LPS, Intergraph ImageStation and PCI Geomatica OrthoEngine. Although these software programs are often geared towards the novice user, some expertise is still required to derive accurate data. As a result, it is important to choose the best software program based on your specific photogrammetric needs.

Few studies have been published which compare two or more of these digital photogrammetry applications and report on how they relate to one another based on their terrain extraction capabilities. This information is important to determine exactly which of the more recent software programs should be used based on desired DEM outcomes and accuracies for specific projects. As a result, this particular study compares two such photogrammetric software programs and limitations and benefits involved with each software program are examined, especially relating to DEM accuracies over various terrain features.

3.2.1 Software Programs

Based on an extensive literature review and the ability to acquire program licenses, two photogrammetric software programs were selected for analysis. The first software program examined was ERDAS (Earth Resources Data Analysis Systems) Imagine 2010, specifically, an extension called LPS (Leica Photogrammetry Suite; name officially and legally changed to LPS) ATE (Automatic Terrain Extraction). LPS is a

comprehensive collection of software tools that enables users to transform raw imagery into reliable, accurate data layers required for digital mapping. Available through a license agreement with Northern Arizona University (NAU), LPS was readily available and accessible for terrain extraction analysis.

The second software program was PCI Geomatica OrthoEngine. Canada-based PCI Geomatica is aimed primarily at faster data processing and allows users to load satellite and aerial imagery where advanced analysis can be performed. OrthoEngine is a powerful photogrammetric tool designed to handle small and large production workloads to efficiently produce quality geospatial products (PCI Geomatics, 2003). In September of 2012, PCI Geomatics release a new version (2013) of OrthoEngine that offered improved DEM extraction capabilities from previous versions. As a result, a 30 day trial license was downloaded from the PCI Geomatics website to be used to test to generation of a terrain model of the Schultz Fire burn area.

3.2.2 Study Area

The study area was located along the southeastern edge of the San Francisco Peaks 10 km northeast of Flagstaff, Arizona. Remnants of an eroded stratovolcano, the San Francisco Peaks form the tallest mountain feature in Arizona consisting of seven prominent peaks ranging from 3073 m (Schultz Peak) to 3851 m (Humphreys Peak). Diverse biomes span different elevations including ponderosa pine forests (1800 m to 2600 m), mixed conifer forests (2400 m to 2900 m), subalpine conifer forests (2900 m to 3500 m) and alpine tundra (above 3500 m) (Brown, 1994). This area also offers numerous scenic drives and a rich array of seasonal recreational activities including, hiking, biking, camping and skiing.

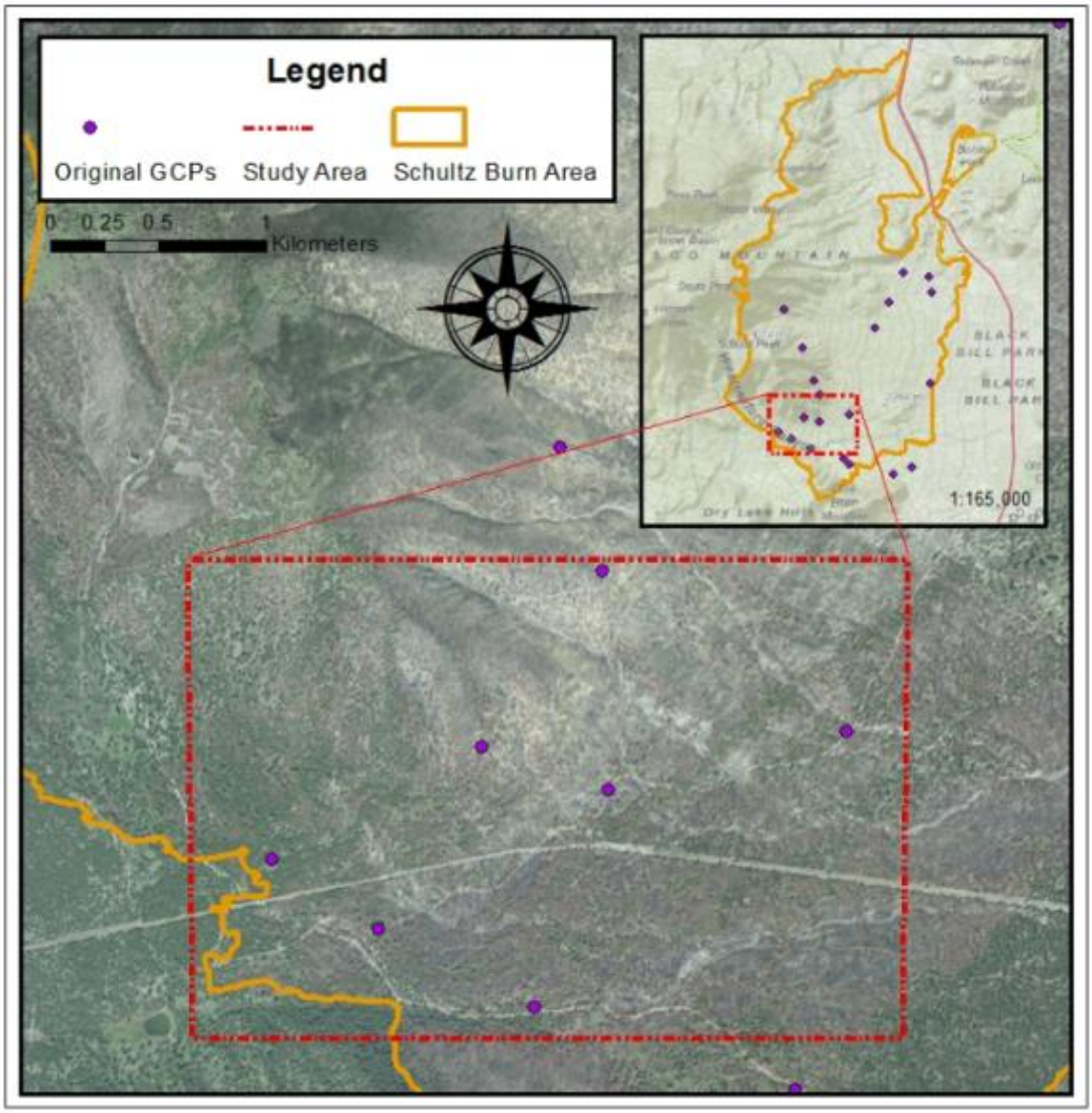

Figure 3.1 The southeastern edge of the San Francisco Peaks. This area was used to compare different DEMs and was based on the availability of GCPs found in the overlap area of two aerial photographs.

During the summer of 2010 the eastern edge of the San Francisco Peaks was impacted by the high severity Schultz Fire. Ignited as a result of an abandoned campfire on June 20th, the fire quickly spread across the steep mountainous slopes due to high winds, burning approximately 60% of the entire area during the first day. Between June 20th and June 30th, the fire burned 6100 ha with approximately 40% being classified as

high severity due to the complete loss of protective ground cover and the creation of hydrophobic soil conditions (U.S. Forest Service, 2010). Although no structures were directly affected by the fire, heavy flooding shortly following the fire caused millions of dollars in damage to the residential communities below the burn.

The primary focus area for this study is located in the southern portion of the Schultz Fire burn area (Figure 3.1). This area, located around Schultz Tank and Little Elden Trail (believed to be the origin of the fire) is situated between Little Elden Mountain to the south and the southeastern base of Schultz Peak to the northwest. This area was selected based on the availability of seven original, pre-marked ground control points (GCPs) found in the overlap of two photos (0404 and 0405) from an aerial flight that took place October 27th, 2010. This study area was limited in extent because OrthoEngine required a minimum of at least three GCPs to be located in the overlap area to extract terrain information from the photos.

3.3 Methods

3.3.1 ERDAS LPS

To begin a project in LPS, a block had to first be created. A block is a term used to describe and characterize projection information, camera or sensor information, imagery associated with the project, GCPs and their measured image position, and the geometric relationship between the imagery in the project and the ground. When first creating a block, I had to specify that a frame camera was used as the geometric model. I also had to identify the rotation system (Omega, Phi and Kappa), the angle units (degrees),

average flying height of the aircraft (1836 m), as well as the horizontal and vertical reference coordinate system (WGS 84).

The next step was to identify parameters associated with the camera to determine the interior geometry of the camera as it existed when the photos were captured. This included defining camera properties such as calibrated focal length, principle points, and radial lens distortions (Table 3.1). In addition to the calibrated camera information, I had to define the calibrated X and Y photo-coordinate values of the fiducial marks located on an image (Table 3.2). These fiducial marks are used to define a photo-coordinate system within each image, as well as determine the origin and orientation of the photo-coordinate system for each image in the block (Leica Geosystems Geospatial Imaging, 2009).

Table 3.1 Detailed camera calibration information.

Camera Calibration Information	
Camera Type	Zeiss RMK Top 15
Calibrated Focal Length (mm)	152.9940
Principal Point xo (mm)	-0.0100
Principal Point yo (mm)	0.0100
K_0 (radial lens distortion)	3.834e-06
K_1 (radial lens distortion)	1.057e-09
K_2 (radial lens distortion)	-9.316e-14
P_1 (decentering distortion)	1.445e-007
P_2 (decentering distortion)	-6.979e-008
Image scale	1:12000

Table 3.2 Calibrated fiducial mark coordinates.

Row #	**Film X (mm)**	**Film Y (mm)**
1	-113.013	-112.996
2	113.004	113.012
3	-112.992	112.994
4	113.008	-112.996
5	-113.002	0.000
6	113.015	0.011
7	0.004	113.007
8	-0.011	-112.999

Once this preliminary information was entered, the raw images could be added to the block. Only two images (0404 and 0405) were added, and the study area consisted of the overlap between these two images (Figure 3.2). Typically, flight strips contain 60% to 80% end lap between adjacent images. For these two images, there was approximately 70% overlap.

Figure 3.2 Image 0405 (left) and 0404 (right). The red boxes indicate the overlap (approximately 70%) between these two images. These images were chosen based on the high number of GCPs found in the overlap area. Note: Top of image is east.

The next step was to determine the interior orientation of the images. This process involved measuring the pixel coordinate positions of the calibrated fiducial marks on each of the two images within the block. However, before the fiducial marks could be established, the fiducial orientation had to be rotated 90º relative to the photo-coordinate system. This rotation was based on the location of the data strip located on the images (top of the image was east and the data strip was along the left edge). Once each image was assigned the correct rotation, the fiducial marks could be established by clicking on the center of the mark, following the correct numbering sequence (Figure 3.3).

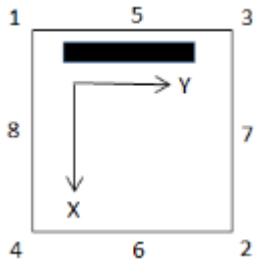

Figure 3.3 The orientation of the fiducial marks based on the rotation of the data strip.

Once all eight fiducial marks were established for the two images, corresponding residuals were displayed. These residuals (Residual X and Residual Y) were computed based on a mathematical comparison made between the original fiducial mark position and the actual measured fiducial mark position. Based on these values, a root mean square error (RMSE) could be calculated. The RMSE represented the overall correspondence between the calibrated fiducial mark coordinates and their measured image coordinates. These values were 0.70 and 0.66 for 0404 and 0405, respectively. Values larger than 0.5 pixels inferred systematic errors or gross measurement errors associated with the image. The errors could be attributed to film deformation, poor scanning quality, mis-measured fiducial mark positions, or incorrect calibrated fiducial mark coordinates (Leica Geosystems Geospatial Imaging, 2009).

After establishing the interior orientation of the images, external properties had to be defined. This process involved establishing the exterior orientation parameters associated with the camera as they existed at the time of photographic exposure. Specifically, the exterior orientation parameters define the position and orientation of the perspective center (X, Y, Z) and rotation angles (Omega, Phi, Kappa) for each image. Thus, each image in a block had different exterior parameters. However, this information was not provided, and could only be established after aerial triangulation.

Aerial triangulation is the process of defining the mathematical relationship between the images contained within a block, the camera that obtained the images, and the ground (Leica Geosystems Geospatial Imaging, 2009). To perform aerial triangulation, seven GCPs and seven tie points were first identified on the overlap area. Since GCPs are identifiable features whose ground coordinates are known (Table 3.3), locating these points in the overlap area helps determine how the images are related spatially to one another. Tie point are also used to determine how the imagery is related, but do not include any coordinate information. Only the image positions in the overlap areas are known and measured, and X, Y and Z coordinate can only be estimated during the aerial triangulation process.

Table 3.3 Seven of the original (pre-marked) GCPs that were located on the overlap of the two images. This information was entered into the software along with corresponding image locations.

Ground Control Points					
GCP ID	**Latitude (Y)**	**Longitude (X)**	**Elevation (Z)**	**Lat DD**	**Long DD**
x005	35:16:58.75567 N	111:35:59.51427 W	2280.6 m	35.28298769	-111.5998650
x006	35:17:08.87393 N	111:36:38.88379 W	2334.08 m	35.28579831	-111.6108011
x009	35:17:35.55066 N	111:36:27.72097 W	2330.638 m	35.29320852	-111.6077003
x01	35:17:26.97140 N	111:37:18.34675 W	2433.976 m	35.29082539	-111.621763
x013	35:17:18.56448 N	111:37:02.32270 W	2390.998 m	35.28849013	-111.6173119
x02	35:17:40.86564 N	111:36:46.75766 W	2464.969 m	35.2946849	-111.6129882
x03	35:18:02.45758 N	111:36:28.49988 W	2492.138 m	35.30068266	-111.6079166

Once all the initial points were established, automatic tie point generation was performed. Rather than manually identify additional tie points on the overlap area, this process utilized digital image matching techniques to automatically identify and measure the image position of congruent points appearing on in the overlap of the two images (Leica Geosystems Geospatial Imaging, 2009). Strategy parameters governing the

operation of the automatic tie point collection procedure could be used to optimize the performance of automatic tie point collection. These factors included search size (window size used to search for corresponding points), correlation size (window size for cross-correlation), least squares size (window size for least square matching), feature point density (feature point density percentage based on internal default), coefficient limit (threshold used to determine whether or not two points are to be considered as possible matches) and initial accuracy (relative accuracy of the initial values used by the automatic tie point generation process; Leica Geosystems Geospatial Imaging, 2009). These values govern the operation of the algorithm and could be adjusted to ensure the quality of the resulting tie points. Default values were used for correlation size (7 x 7), feature point density (100%), coefficient limit (0.80) and initial accuracy (10%). However, the value for search size was increased from 21 x 21 to 30 x 30 (increased for steeper areas) and least square size was decreased from 21 x 21 to 15 x 15 (decreased due to large degrees of topographic relief). Other values were tested, but did not produce the desired results associated with these parameters.

Once additional tie points were generated, aerial triangulation could occur. Aerial triangulation is performed using a bundle block adjustment. This approach utilized an iterative least squares solution. Based on the triangulation, the perspective center and rotation angles of each image in the block as they existed at the time of capture were established. A triangulation summary was generated which included a total unit-weight RMSE (0.2164). This standard deviation of unit weight is a global precision indicator describing the quality of the entire solution (Leica Geosystems Geospatial Imaging, 2009).

The final step in the process was the automatic extraction of terrain information and the creation of a DEM. Using a robust algorithm, LPS compared the two images and looked for the image positions of conjugate features appearing in the overlap portion of the images. The three-dimensional position of the features in the block projection system was then computed. The results were exported as a DEM with a resolution of 1 m. This DEM was then compared to the DEM generated by OrthoEngine as well as a 10 m reference DEM from the United States Geological Survey (USGS), and the results were analyzed based on accuracy and consistency of the resulting elevation data sets.

3.3.2 PCI OrthoEngine

To begin using OrthoEngine, a new project had to be created by selecting the Aerial Photography math model. This is a rigorous model that compensates for known distortions to calculate the position and orientation of the camera at the time the image was taken (PCI Geomatics, 2006). Once this model was selected, I had to define the camera type (standard aerial) and determine that the exterior orientation would be computed from GCPs and tie points. Additionally, I had to define the projection related to the GCPs (Long/Lat) and output data (UTM) and determine output pixel/line spacing (1 m).

Since a standard aerial camera was used to acquire the images, the next step was to establish camera calibration information. In addition to defining focal length, principal point offset, decentering distortion, and image scale (Table 3.1), fiducial mark locations had to be established (Table 3.2). However, rather than the typical numbering sequence (Figure 3.3), the coordinates of the fiducial marks were determined by their position on the image. This included defining X and Y coordinates of the fiducial marks for the top

left, top middle, top right, right middle, bottom right, bottom middle, bottom left and left middle edges and corners (corresponding to row number 3, 7, 2, 6, 4, 8, 1, and 5, respectively, from LPS).

The next step was to import the images into the project. Again, only two images (0404 and 0405) were used because of the high density of available GCPs, and the study area consisted of the overlap between these two images (Figure 3.2). One of the major limiting factoring for OrthoEngine was that it required at least three GCPs to be located in the overlap area of the images to extract elevation information. This greatly limited the number of images that could be included in the project since there were often less than three GCPs located in the overlap area of additional images.

Once the images were added to the project, the fiducial mark locations could be collected. This collection was based on the position of the fiducial marks as they appeared in the image on the screen. If the fiducial mark in the upper left corner of the image was selected, then this needed to be set as top left in the fiducial mark collection window. OrthoEngine automatically adjusts its parameters to account for the orientation of the scanned image relative to the orientation of the camera (PCI Geomatics, 2003). Additionally, I had to set the calibration edge indicating the position of the data strip was on the left side of the image. Once all of the fiducial mark locations were established, error values were calculated for each position. These values ranged from 0.1 to 0.4 pixels for each position on the images. These values were determined by comparing the fiducial mark positions based on the measurements taken from the screen with the fiducial information that was entered from the camera calibration report. Errors greater than one

pixel indicated that either the coordinates from the camera calibration report were entered incorrectly or the fiducial mark was collected incorrectly from the scanned image.

The next step was to determine exterior orientation. Exterior orientation represents a transformation from the ground coordinate system to the photo coordinate system. This was determined by manually collecting seven GCPs and seven tie points found in the overlap area of the imagery. Again, GCPs are features that can clearly be identified in the raw imagery which also have known ground coordinates (Table 3.3). These GCPs are used to determine the relationship between the raw image and the ground by associating the location on the image to the X, Y and Z coordinates on the ground. As mentioned, the minimum GCP requirement for a project was 3 (although it was highly recommended that more were used to ensure accuracy). Additionally, tie points were used to extend ground control over areas that did not contain GCPs. Again, these are features that were clearly identifiable in the two images (but do not have known ground coordinates), and helped identify how the images spatially relate to each other. Automatic tie point collect procedures could also be used to collect additional points (rather than manually collect more points).

After these control and tie points were entered, bundle adjustment could occur. The bundle adjustment is simply a computation of a rigorous math model, which is a method to calculate the position and orientation of the aerial camera at the time the image was taken. Once the position and orientation of the sensor was identified, this information could be used to accurately account for known distortions in the image. GCPs and tie points combined with the knowledge of the intricate geometry of the sensor are used to calculate the best fit for all images in the project simultaneously (PCI Geomatics, 2003).

The final step before DEM extraction was to create epipolar images. Epipolar images are stereo pairs that are reprojected so that the left and right images have a common orientation, and matching features between the images appear along a common X-axis (PCI Geomatics, 2003). Using epipolar images increases the speed of the correlation process and reduces the possibility of incorrect matches. Once these epipolar images were created from the two images, a DEM could be extracted.

To create a DEM, OrthoEngine uses image correlation to extract matching pixels in the two images and then uses the sensor geometry from the computed math model to calculate X, Y, and Z positions (PCI Geomatics). This DEM was extracted from the overlap between the epipolar pairs. Additional parameters were set which included setting the minimum and maximum elevation (estimated, 2000 m and 3000 m), DEM detail (high), terrain type (mountainous) and the smoothing filter (low). Finally, I had to select that the DEM was to be geocoded and have a resolution of 1 m.

The resultant DEM was then compared to the DEM generated from LPS by differencing a clipped section of the two data sets. This was used as a way to determine erroneous data (blunder areas) as well as more minor differences in the extracted elevations. Additionally, profile graphs were compared over selected ground features of interest. These graphs also included a reference DEM (10 m) from the USGS as a way to compare the detail associated when the new DEMs. The results were then analyzed to determine accuracies associated with the two generated models.

3.4 Results

The DEMs generated by LPS (Figure 3.4) and OrthoEngine (Figure 3.5) covered an area of approximately 700 ha. Elevation values ranged from 2050 m to 2797 m for LPS, while for OrthoEngine, these values ranged from 2000 m to 2748 m. However, both of these data sets also included areas where obvious blunders occurred during the extraction process (indicated by black arrows on both of the figures). For LPS, this included the entire northern edge of the DEM area, as well as some smaller areas located on Schultz Peak. For OrthoEngine, one major noticeable blunder area occurred along the northern edge of the DEM area, and was predominantly located within the steep mountainous region. These blunder areas typically contained elevation values that were much lower than the other values located throughout the DEM extents.

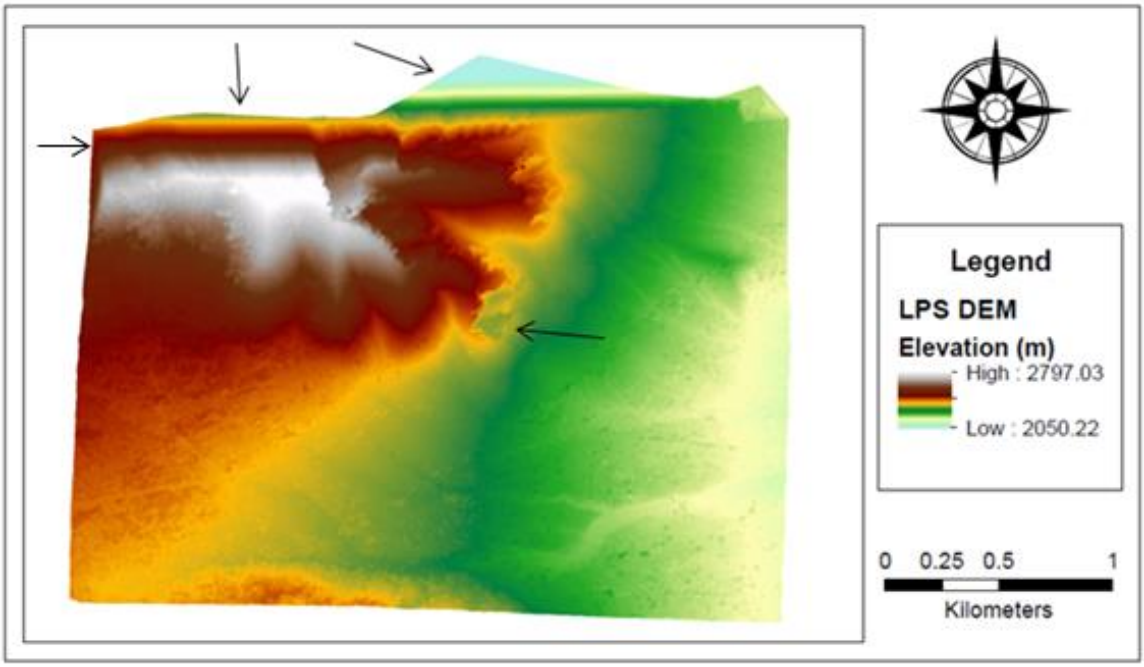

Figure 3.4 DEM generated by ERDAS Imagine LPS. The black arrows indicate major blunder areas that occurred during the extraction process. These areas were predominantly along the northern section of the study area as well as smaller mountainous areas on Schultz Peak.

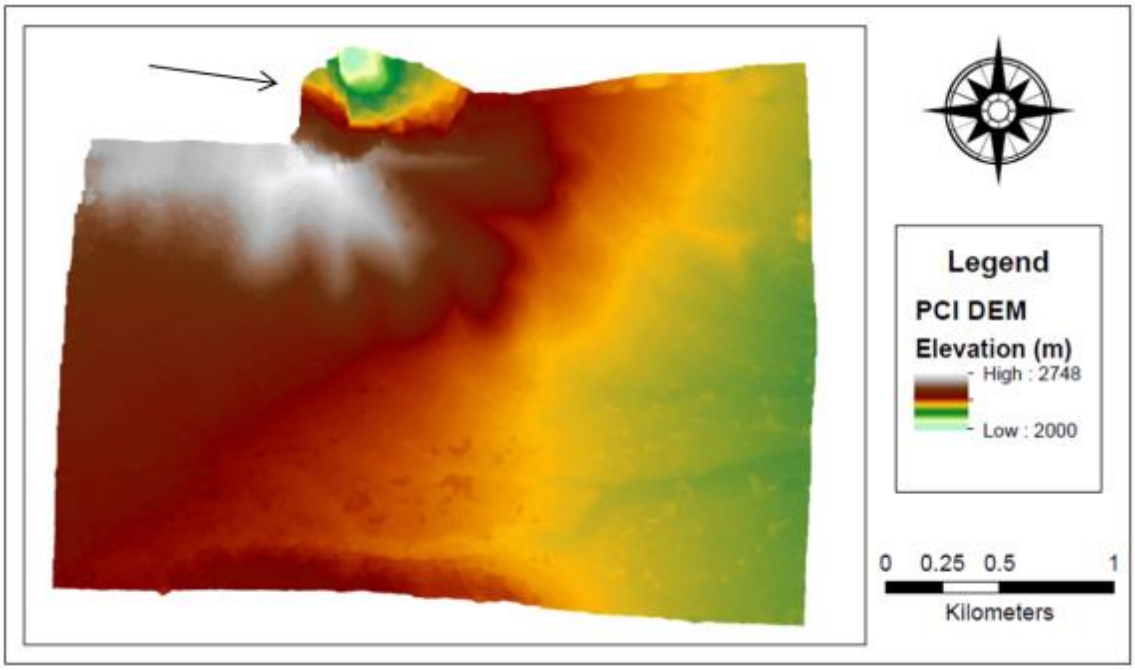

Figure 3.5 DEM generated by PCI Geomatica OrthoEngine. The black arrow indicates a major blunder area that occurred during the extraction process. This area was focused on the northern section of the study area within the mountainous region of Schultz Peak.

To evaluate the overall accuracy of the rest of the two DEM areas, a reduced section of the original extent was selected for the primary study area. This area covered approximately 500 ha and restricted the availability of the major blunder areas (although it did not completely eliminate them). Elevation values were much more consistent between the two DEMs in this area, and as a result, a thorough comparison could be made to determine major and minor discrepancies between the two data sets. Additionally, a third DEM of this area was used as a reference to visually and quantitatively compare the results to determine accuracies of the other two DEMs.

For the reference DEM, I used the National Elevation Dataset (NED), which is the primary elevation data product of the USGS. This 10 m DEM consisted of smooth, seamless data devoid of errors. However, due to undulations of the geoid, a value of 22.9 was subtracted from these elevation values to match the surface of the other two DEMs.

This correction was based on the GEOID03 model and was determined by the extent of the study area. Although there was a variance in resolutions (1 m vs. 10 m), all three DEMs could still be compared to determine overall accuracies between each of the data sets (Figure 3.6).

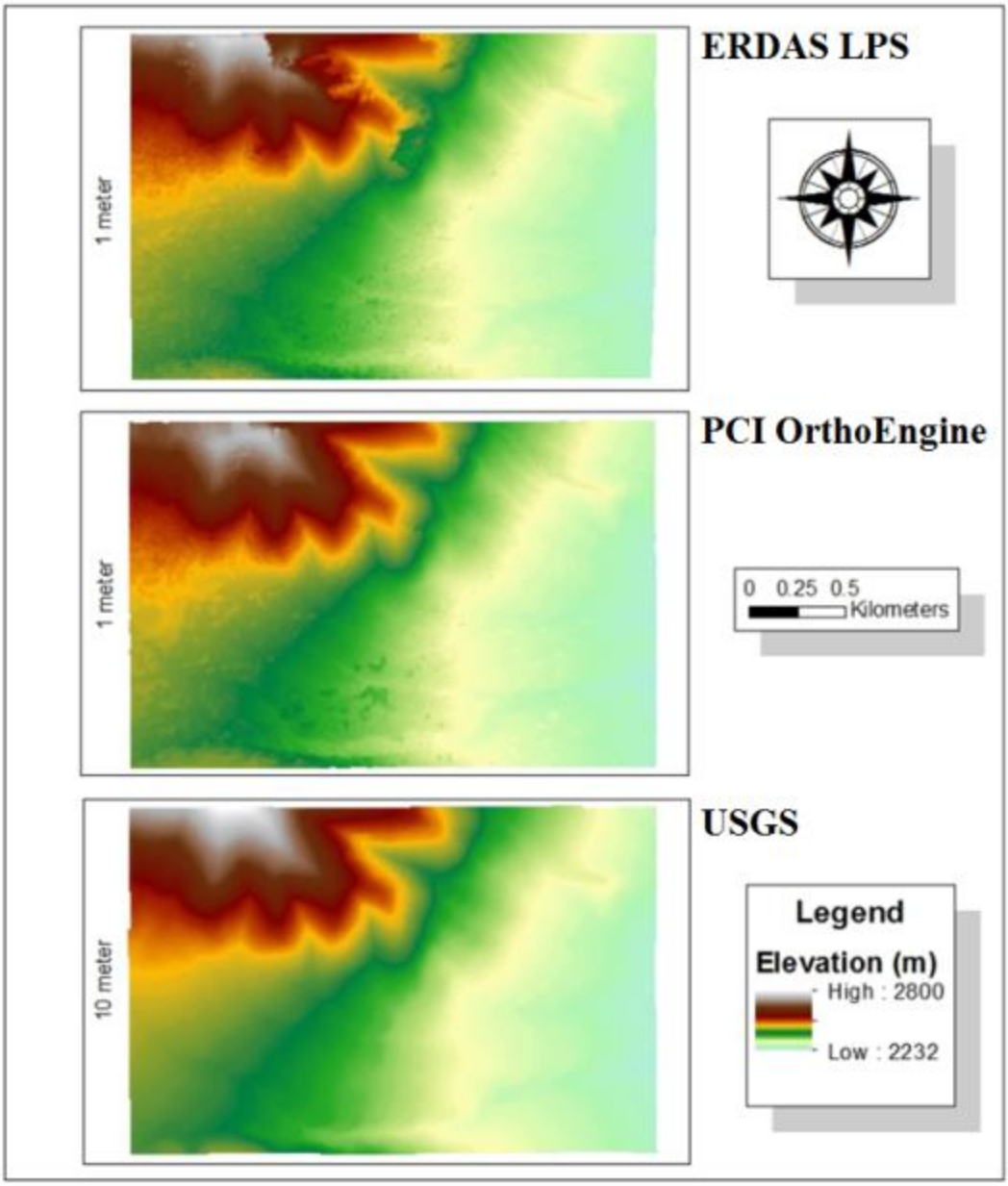

Figure 3.6 The three different DEMs (ERDAS, PCI, and USGS) used for the study area.

To quantitatively assess the variations in the generated datasets, I differenced the surfaces of the DEMs generated by ERDAS and PCI (Figure 3.7). These differenced values ranged from -123.285 m to 84.778 m. Negative values (blue) indicate areas where ERDAS elevations were lower than PCI elevations, while positive values (red) indicate areas where PCI elevations were lower than ERDAS elevations. The mean for these values was -1.58 m and the standard deviation was 8.86. However, to more accurately represent this data, I wanted to categorize these values into three separate classes including major differences (blunders), moderate differences and minor/no differences.

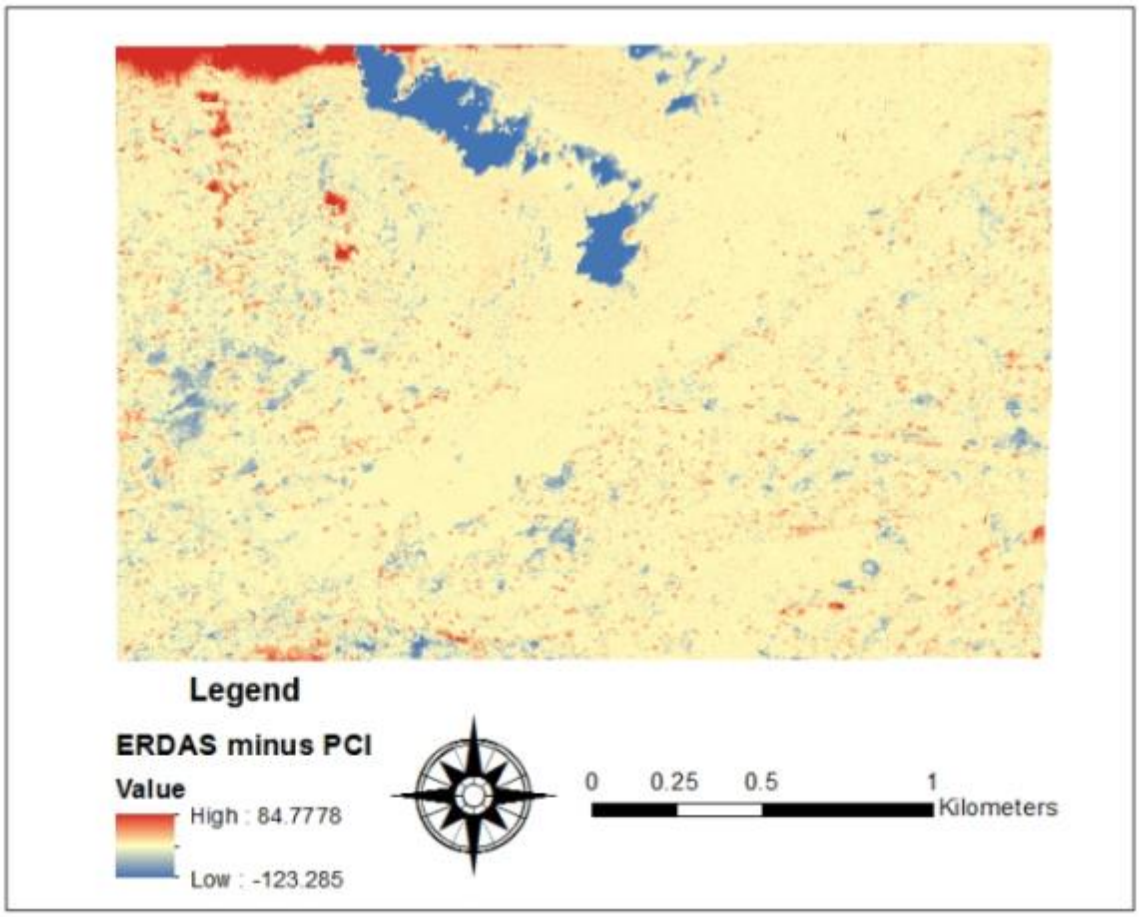

Figure 3.7 Differences in elevation values based on PCI subtracted from ERDAS. Negative values (blue) indicate areas where ERDAS elevations were lower than PCI elevations, and positive values (red) indicate areas where PCI elevations were lower than ERDAS elevations.

To analyze the major discrepancies between the DEMs, I attempted to isolate the known blunder areas. Using approximately two standard deviations from zero (±18), values above and below this this extent were classified as major differences (blunders). These values could then be removed from the data to help highlight the more minor differences between the datasets (Figure 3.8). They could also be analyzed further to determine whether there was any consistency in the location where these blunders occurred (such as on a specific slope or aspect).

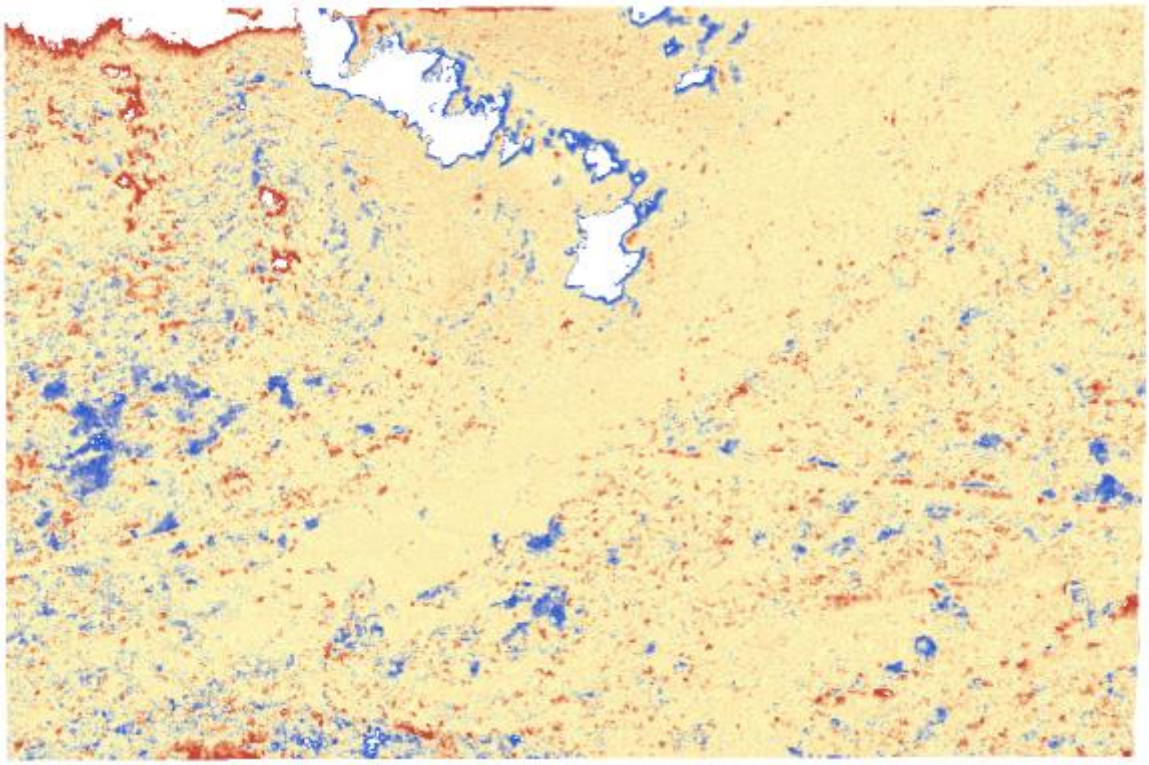

Figure 3.8 Differenced elevation values with the major blunder areas removed. This included removing differenced values below -18 m as well as differenced values above 18 m (two standard deviations from zero).

Once these areas of major differences were distinguished, the next step was to isolate the areas of moderate and minor/no differences. Using approximately half a standard deviation from zero (±4.5), values below (-18 m to -4.5 m) and above (4.5 m to 18 m) this extent were classified as the areas of moderate differences. In addition to the

major blunder areas, these values could also be removed from the dataset to help highlight the areas that contained minor/no differences (Figure 3.9).

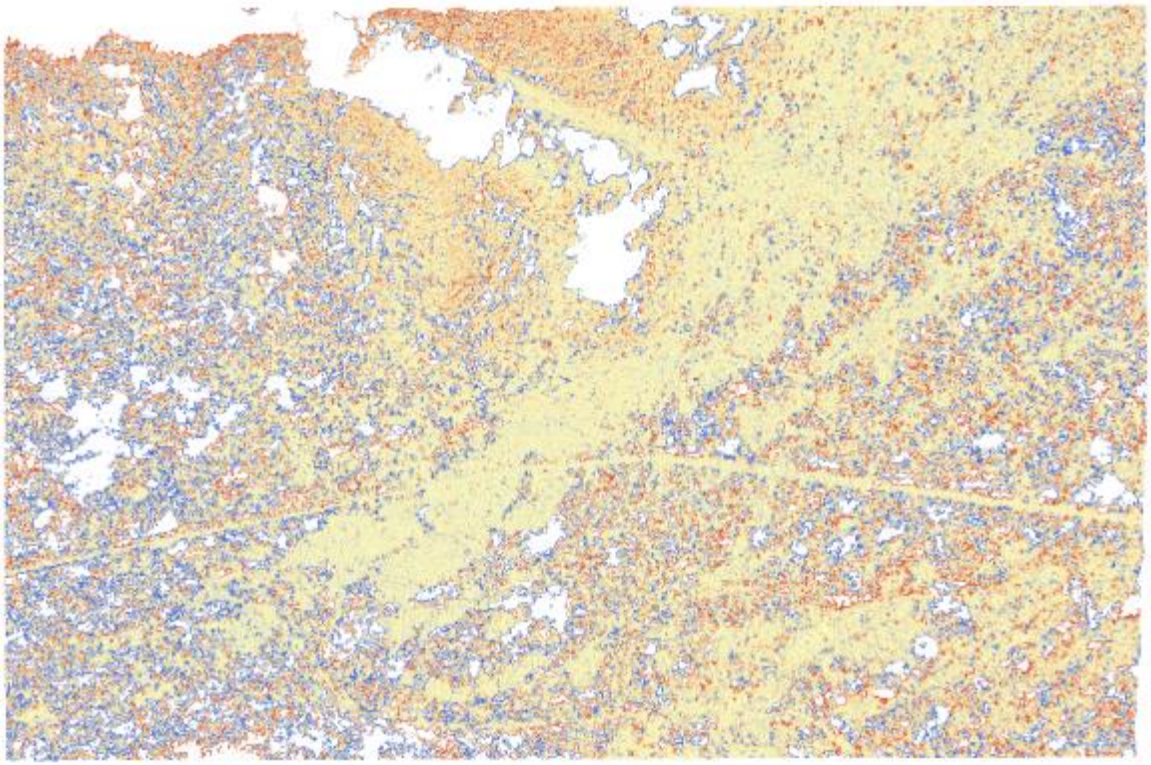

Figure 3.9 Differenced elevation values with the major and moderate blunder areas removed. This included removing differenced values below -4.5 m as well as differenced values above 4.5 m (half a standard deviation from zero).

Once these three classes were identified, the results could be analyzed to determine if there were certain features (such as tree canopies) that were causing the variations in the DEMs. This was achieved by creating shapefile layers out of the each of the three classes and using an orthophoto of the area to determine areas where these major, moderate and minor differences were occurring (Figure 3.10). The transparency of the layers could be set and the orthophoto could visually be inspected to determine other factors which may have had an impact on the accuracy of these elevation datasets (Figure 3.11).

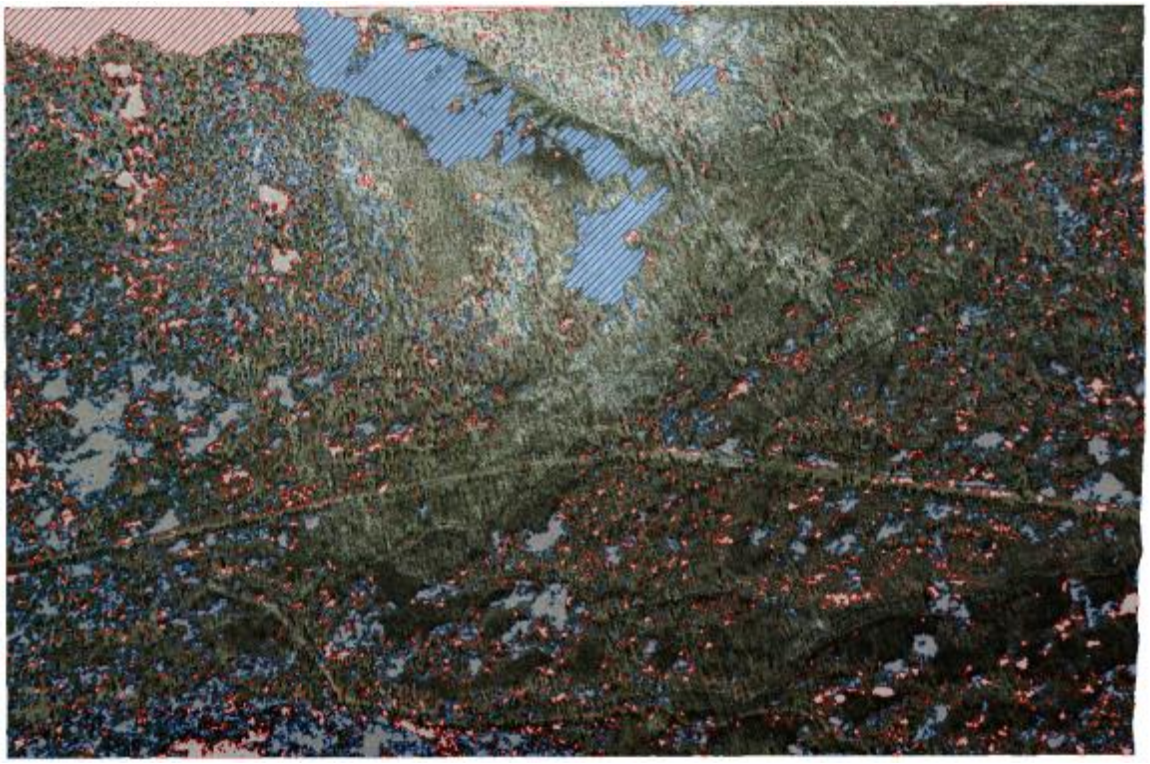

Figure 3.10 Orthophoto with major differenced areas (red and blue hatch mark) and moderate differenced areas (red and blue with gray transparency). Areas where minimum/no differences occurred where left clear.

Based on these results, it was determined that the moderate difference elevation locations tended to be focused over unburned areas which contained a lot of tree canopies. This indicated that the DEM generated by PCI was picking up the tree canopies while ERDAS was not, resulting in a negative differenced value. In contrast, the minimum/no difference elevation locations tended to be focused over highly burned terrain. These areas tended to be more open due to the loss of tree canopy. These areas also contained higher contrast areas which may have caused both systems to overall pick up the same elevation information resulting in little differences. Lastly, although there is no real indication as to why the major blunder areas were occurring where they did, overall they tended to be on sleeper slopes in areas of low contrast.

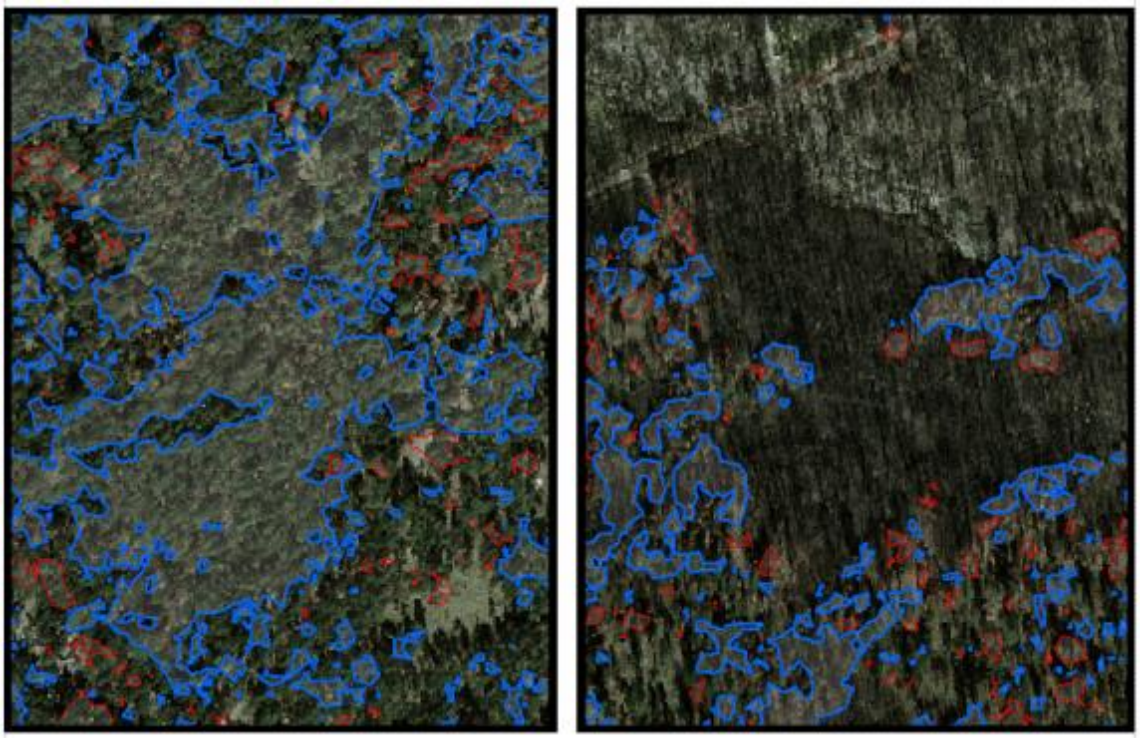

Figure 3. 11 A close up view highlighting that for the moderate difference elevation, the DEM generated by PCI tended to be picking up tree canopies (left), while areas of minimum/no difference elevations tended to be focused over highly burned terrain (right).

Profile graphs over some of these selected ground features of interest were also analyzed as a way to further assess the accuracies of these elevation datasets (Figure 3.12). These features included a gully (location #1), ridge-to-ridge (location #2), a severely burned wash (location #3) as well a flat, shadowed area along the pipeline (location #4). Additionally, four more areas were selected using specific features from the differenced data set (Figure 3.13). These locations were selected to include areas over negative differenced values (location #5), positive differenced values (location #6), negative and positive differenced values (location #7) as well as a known blunder area (location #8). All three DEMs were included in this data and the results were graphed to visually represent the selected feature (Figure 3.14 and 3.15)

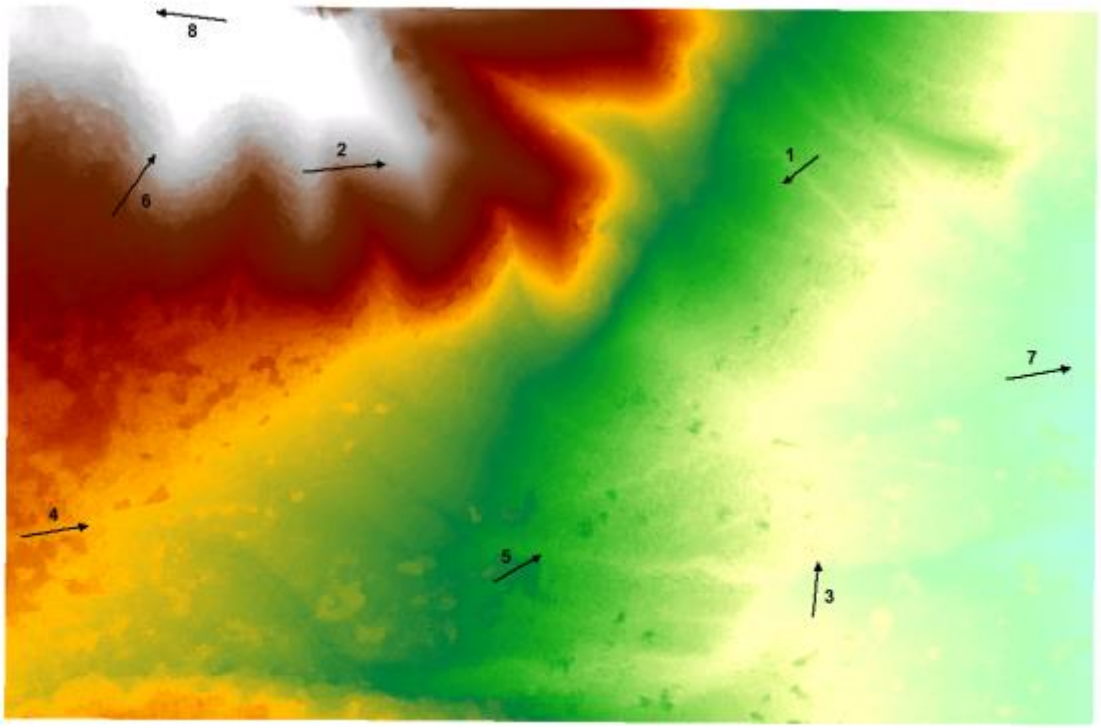

Figure 3.12 Profile graph locations viewed using the PCI DEM. These locations were selected based on specific features such as over a gully (1) and across a ridge (2).

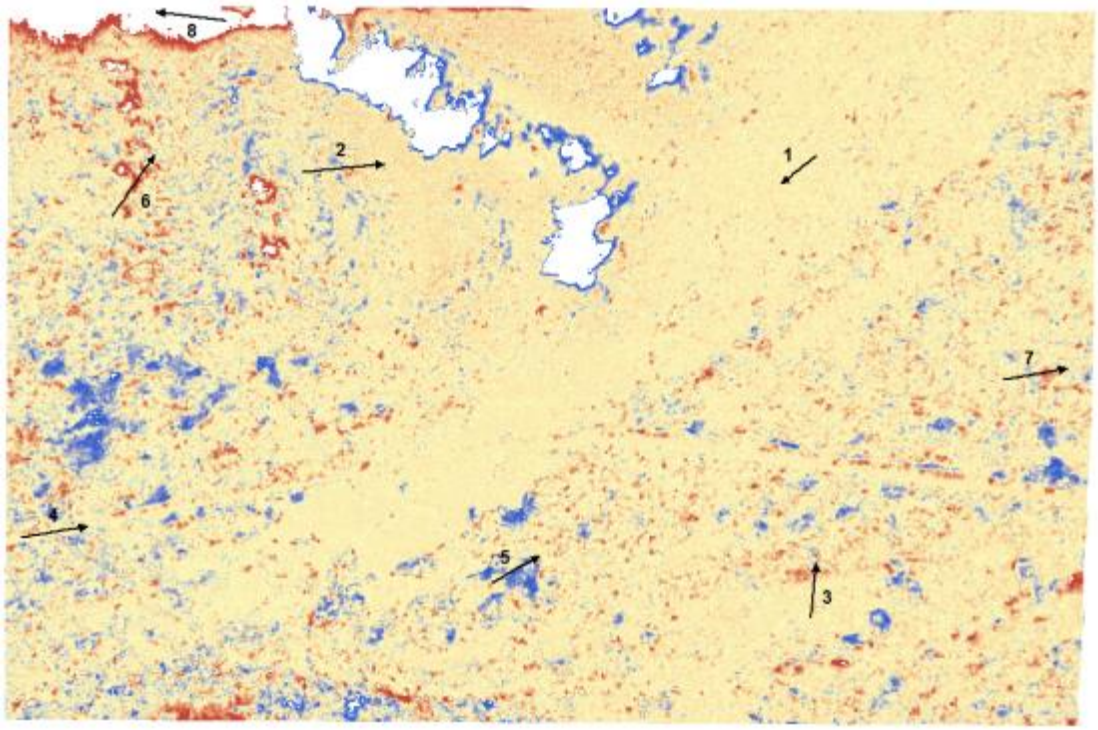

Figure 3.13 Profile graph locations viewed using the differenced dataset. These locations were selected to inspect certain areas where these differences occurred.

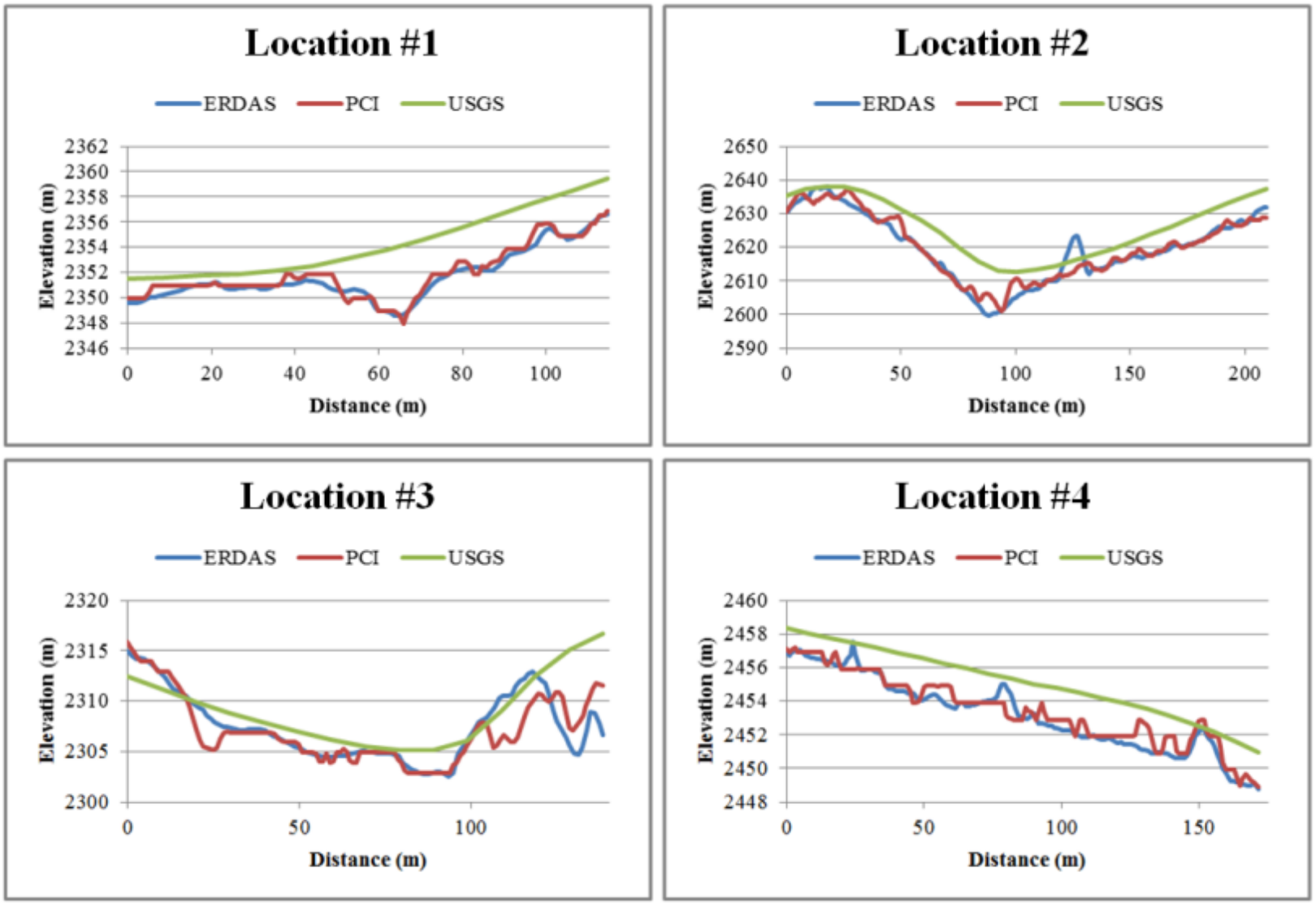

Figure 3.14 Profile graphs over selected features of interest. These included a gully (location #1), ridge-to-ridge (location #2), a severely burned wash (location #3) as well a flat, shadowed area along the pipeline (location #4).

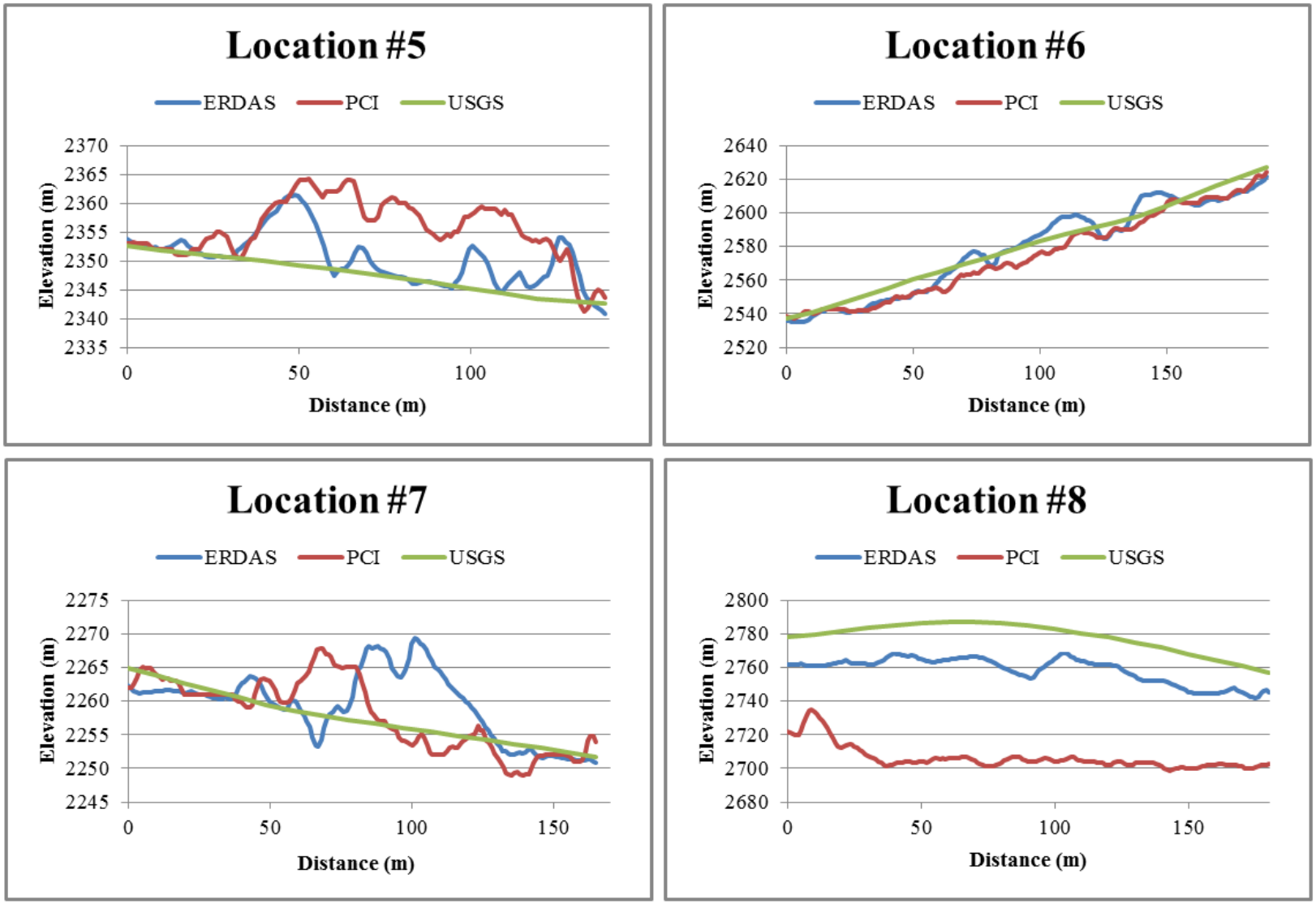

Figure 3.15 Profile graphs over feature locations. These locations were selected to include areas over negative differenced values (location #5), positive differenced values (location #6), negative and positive differenced values (location #7) as well as a known blunder area (location #8).

3.5 Discussion

Although limited in area, results indicate that both digital photogrammetric software programs (ERDAS LPS and PCI OrthoEngine) can be used to generate complex terrain affected by fire and flooding. However, there were benefits and limitations to both software programs, all of which must be taken into consideration when choosing a program for future photogrammetric projects.

For LPS, there seemed to be a tradeoff between accuracy and flexibility. Although the software was more flexible (did not require a minimum number of GCPs to be located in the overlap), the overall accuracy of the DEM was not as good as the DEM generated by OrthoEngine. This included more areas of obvious blunders located throughout the DEM, especially in the areas of more complex terrain. It also appeared to have a built-in smoothing effect (did not pick up tree canopies) which could not be adjusted. In contrast, OrthoEngine was much more limited in its abilities (required a minimum of three GCPs to be located in the overlap), but the overall accuracy of the DEM contained slightly better data when compared to LPS. It also tended to pick up more tree canopies, which unlike LPS, could be adjusted if you didn't want to include these features.

Looking at the various profile graphs, both software programs seem to be picking up the same details for the selected features. There are obvious areas where both programs seemed to be picking up more noise (or possibly tree canopies), but both DEMs generally were able to pick up much more detail when compared to the reference DEM. However, greater detail in the ERDAS and PCI DEMs was not just a function of difference between the DEM resolutions (Figure 3.16). There are still obvious

differences between the two generated DEMs and the reference DEM, most likely due to differences in collection and generation dates between the data sets.

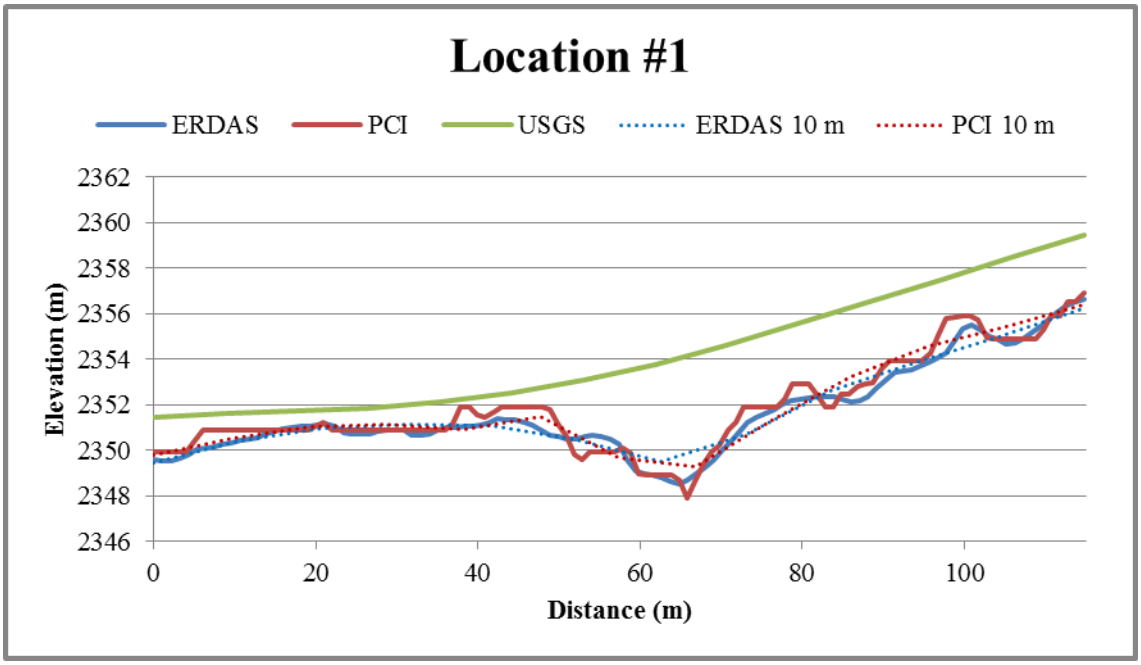

Figure 3.16 Profile graph over location #1 which also includes degraded (10 m) DEMs from ERDAS and PCI.

When looking at differences between the two generated DEMs, the highest amount of difference occurred in densely forested, unburned areas, while the smallest amount of difference occurred in highly burned areas. This may have been a result of OrthoEngine picking up more tree canopies in the unburned areas. These areas tended to produce elevation values that were higher than those produced by LPS. However, in the highly burned areas, there was less tree canopy cover, and as a result, both software programs were picking up the details in the ground so there was less of a difference.

Finally, it is important to mention that while additional studies are needed, it appears that future software selection may depend on specific study requirements or preferences. This study was based on a very a limited study area (the overlap of two images) as well as a limited time period to work with the data (30 day trial). As a result,

more studies are needed to understand the full capabilities of OrthoEngine, especially in more complex terrain affected by fire. However, it is also important to remember that adequate GCP cover may not be achievable in this type of terrain, and as a result, OrthoEngine may not be suitable for these types of studies even though overall it produced DEMs with less blunder areas. However, if the focus is over a small area where adequate ground control is available, OrthoEngine may be more beneficial than LPS.

3.6 Conclusion

Based on the results, it was determined that although LPS was more flexible (did not require a minimum number of GCPs in the overlap), it also tended to produced more errors (obvious blunders) throughout the DEM. On the other hand, OrthoEngine was much more limited in its capabilities (required at least three GCPs in the overlap), but also contained less errors throughout the DEM.

OrthoEngine also tended to pick up more tree canopies than LPS, especially in heavily forested (unburned) areas of the fire. However, these differences were not consistent, and tended to be more spread out and random throughout the study area. These areas also contained the most amount of difference between the two DEMs while highly burned areas contained the least amount of difference.

This study also involved data collected over a limited area (two images) as well as over a limited time period (30 day trial). As a result, additional studies are needed to produce more comprehensive results. This includes exploring additional terrain conditions (different slopes, elevations, aspects, and burn severities) as well as a larger area to determine if different factors have an effect on the accuracy of the DEM generated by PCI.

4. Conclusions

- Digital photogrammetry provides a feasible way of analyzing high accuracy terrain data following a high severity wildfire.
    - Automated procedures greatly increased rates in which high-resolution DEMs could be generated.
    - Once obvious blunder areas were removed from the data, the overall accuracy of the DEMs significantly increased.
- Widespread GCP cover is important, if not crucial, in the generation of accurate DEMs in areas affected by fire and flooding. This is especially important to consider for future studies on wildfires.
    - For some photogrammetric software programs (such as PCI OrthoEngine), it is impossible to proceed unless a minimal amount of control is measured in the overlap area of the aerial imagery.
    - Wildfires typically occur in areas of complex terrain (steep slopes, dense vegetation, areas that are isolated and inaccessible) and it may not be feasible to collect adequate GCPs in the affected areas after a fire.
    - It was determined that the greatest proportion of blunders typically occurred in areas where there was limited GCP cover. These areas were predominantly located on steeper slopes and in higher elevations where abundant GCP coverage was difficult to obtain.
    - It can become very time consuming to collect GCPs (pre-marked and/or post-marked) using DGPS equipment, especially if the area is as extensive as the Schultz Fire.

- Some expertise is still required to derive accurate data when generating DEMs.
  - User inexperience and error may have played a role in DEM inaccuracies. This could have included incorrect data entry or defining improper image rotations.
  - There is a degree of control over certain strategy parameters when generating a DEM and wrong choices can have a significant detrimental effect on the accuracy of the DEM.
  - A 30-day license trial of OrthoEngine was too limited, and more time was needed to explore further capabilities. This included DEM editing capabilities as well as testing different parameters to achieve more accurate results.
- Choosing the correct software program based on overall capabilities is important.
  - There are benefits and limitations to all the available software programs, and users must select the best ones for their specific needs.
  - LPS was found to be more flexible (no minimal amount of GCPs in the overlap), but tended to produce more systematic errors. OrthoEngine was much more limited, but seemed to produce more accurate results. However, it is also important to keep in mind that this area was very limited, and more studies are needed to further explore the capabilities of OrthoEngine.
  - OrthoEngine was much more user friendly (required less steps), but LPS had a much clearer work-flow when compared to OrthoEngine.
  - OrthoEngine seemed to pick up more tree canopies than LPS. This is important to consider when choosing the best software program based on the results you are looking to obtain.

- Current research suggests that has been a shift away from photogrammetry to applications that utilize LiDAR.
    - Benefits of LiDAR include the ability to see through canopies, instantaneous results, and higher accuracies when compared to photogrammetric applications.
    - However, these applications are more expensive, and cannot be used with historical data. All these factors are important when considering methods of obtaining high-resolution DEMs.
- Future studies using photogrammetric techniques on terrain affected by fire and flooding are needed.
    - Results from this study are very specific to the Schultz Fire. Future studies would be beneficial to see how other results conform or differ.
    - The study area was very limited to eastern facing slopes, so additional studies looking at western facing slopes may indicate different results.

5. Literature Cited

Acharya, B., Chaturvedi, A. 1997. Digital terrain model: elevation extraction and accuracy assessment. Journal of Surveying Engineering 123, 71-76.

Adams, J.C., Chandler, J.H. 2002. Evaluation of Lidar and medium scale photogrammetry for detecting soft-cliff coastal change. Photogrammetric Record 17, 405-418.

Baily, B., Collier, P., Farres, P., Inkpen, R., Pearson, A. 2003. Comparative assessment of analytical and digital photogrammetric methods in the construction of DEMs of geomorphological forms. Earth Science Processes and Landforms 28, 307-320.

Baldi, P., Bonvalot, S., Briole, P. Coltelli, M., Gwinner, K., Marsella, M., Puglis, G., Rémy, D. 2002. Validation and comparison of different techniques for the derivation of digital elevation models and volcanic monitoring (Vulcano Island, Italy). International Journal of Remote Sensing 23, 4783-4800.

Baltsavias, E.P., Li, H., Stefanidis, A., Sinning, M., Mason, S. 1996. Comparison of two digital photogrammetric systems with emphasis on DTM generation: case study glacier measurement. International Archives of Photogrammetry and Remote Sensing 31, 104-109.

Brown, D.E. 1994. Biotic communities: Southwestern United States and northwestern Mexico. Salt Lake City: University of Utah Press.

Brown, D.G., Arbogast, A.F. 1999. Digital photogrammetric change analysis as applied to active coast dunes in Michigan. Photogrammetric Engineering and Remote Sensing 65, 467-474.

Chandler, J. 1999. Effective application of automated digital photogrammetry for geomorphological research. Earth Surface Processes and Landforms 24, 51-63.

Fabris, M., Pesci, A. 2005. Automated DEM extraction in digital aerial photogrammetry: precisions and validation for mass movement monitoring. Annals of Geophysics 48, 973-988.

Ghosh, S.K. 1988. Analytical photogrammetry (2nd edition). New York: Pergamon Press.

Gong, J., Li, Z., Zhu, Q., Sui, H., Zhou, Y. 2000. Effects if various factors on the accuracy of DEMs: an intensive experiment investigation. Photogrammetric Engineering and Remote Sensing 66, 1113-1117.

Gooch, M.J., Chandler, J.H., Stojic, M. 1999. Accuracy assessment of digital elevation models generated using the erdas imagine orthomax digial photogrammetric system. Photogrammetric Record 16, 519-531.

Grahame, J.D, Sisk, T.D. 2002. Canyons, cultures and environmental change: An introduction to the land-use history of the Colorado Plateau. [10/26/2013] <http://www.cpluhna.nau.edu/>

Habib, A., Ghanma, M., Morgan, M., Al-Ruzouz, R. 2005. Photogrammetric and LiDAR data registration using linear features. Photogrammetric Engineering and Remote Sensing 71, 699-707.

Kääb, A. 2002. Monitoring high-mountain terrain deformation from repeated air- and spaceborne optical data: examples using digital aerial imagery and ASTER data. ISPRS Journal of Photogrammetry and Remote Sensing 57, 39-52.

Kerle, N. 2002. Volume estimation of the 1998 flank collapse at Casita Volcano, Nicaragua: a comparison of photogrammetric and conventional techniques. Earth Surface Processes and Landforms 27, 759-772.

Lane, S.N., James, T.D., Crowell, M.D. 2000. Application of digital photogrammetry to complex topography for geomorphological research. Photogrammetric Record 16, 793-821.

Lascelles, B., Favis-Mortlock, D., Parsons, T., Boardman, J. 2002. Automated digital photogrammetry: a valuable tool for small-scale geomorphological research for the non-photogrammetrist? Transactions in GIS 6, 5-15.

Leica Geosystems Geospatial Imaging, 2006. Leica Photogrammetry Suite Automatic Terrain Extraction. Leica Geosystems Geospatial Imaging, LLC., pp. 7-162.

Leica Geosystems Geospatial Imaging, 2009. LPS Project Manager User's Guide. Leica Geosystems Geospatial Imaging, LLC., pp. 3-401.

Marzolff, I., Poesen, J. 2009. The potential of 3D gully monitoring with GIS using high-resolution aerial photography and a digital photogrammetry system. Geomorphology 111, 48-60.

Mathew, S., Davidson-Arnott, R.G.D., Ollerhead, J. 2010. Evolution of a beach-dune system following a catastrophic storm overwash event: Greenwich Dunes, Prince Edward Island, 1936-2005. Canadian Journal of Earth Sciences 47, 273-290.

Mora, P., Baldi, P., Casula, G., Fabris, M., Ghirotti, M., Mazzini, E., Pesci, A. 2003. Global positioning systems and digital photogrammetry for the monitoring of mass movements: application to the Ca' di Malta landslide (northern Apennines, Italy). Engineering Geology 68, 103-121.

Neary, D.G., Koestner, K.A., Youberg, A., Koestner, P.E. 2012. Post-fire rill and gully formation, Schultz Fire 2010, Arizona, USA. Geoderma 191, 97-104.

PCI Geomatics, 2003. Geomatica OrthoEngine Users Guide. PCI Geomatics Enterprises Inc., Richmond Hill. pp 1-158.

PCI Geomatics, 2006. Extracting elevation from air photos. PCI Geomatics Enterprises Inc., Richmond Hill. pp. 1-8.

Pulighe, G., Fava, F. 2013. DEM extraction from archive aerial photos: accuracy assessment in areas of complex topography. European Journal of Remote Sensing 46, 363-378.

Rayburg, S., Thoms, M., Neave, M. 2009. A comparison of digital elevation models generated from different data sources. Geomorphology 106, 261-270.

Ruzgiene, B. 2007. Comparison between digital photogrammetric systems. Geodesy and Cartography 33, 75-79.

Ruzgiene, B., Alekniene, E. 2007. Analytical and digital photogrammetric geodata production systems (a comparison test). Geodesy and Cartography 33, 50-54.

Schiefer, E., Gilbert, R. 2007. Reconstructing morphometric change in a proglacial landscape using historical aerial photography and automated DEM generation. Geomorphology 88, 167-178.

Sefercik, U.G. 2007. Comparison of dem accuracies generated by various methods. International Conference on Recent Advances in Space Technologies, pp. 379–382.

Torlegard, K. 1988. Transference of methods from analytical to digital photogrammetry. Photogrammetria 42, 197-208.

U.S. Forest Service. 2010. Burned Area Emergency Response Report, July 8, 2010. Coconino Notional Forest, Flagstaff, Arizona, 1-167.

Youberg, A., Koestner, K., Neary, D. 2010. Wildfire, rain and floods: a case study of the June 2010 Schultz Wildfire, Flagstaff, Arizona. Arizona Geology 40(3).

Zomrawi, N., Hussien, M.A., Mohamed, H. 2013. Accuracy evaluation of digital aerial triangulation. International Journal of Engineering and Innovative Technology 2, 7-11.

6. Appendix

Appendix 6.1 Acronyms and abbreviations

ALS	Airborne Laser Scanning
ATE	Automatic Terrain Extraction
AZGS	Arizona Geological Survey
BAER	Burned Area Emergency Response
DDPS	Desktop Digital Photogrammetry System
DEM	Digital Elevation Model
DGPS	Differential Global Positioning System
DPW	Digital Photogrammetric Workstation
DSM	Digital Surface Model
DTM	Digital Terrain Model
ERDAS	Earth Resources Data Analysis System
GIS	Geographic Information System
GCP	Ground Control Point
InSAR	Interferometric Synthetic Aperture Radar
LiDAR	Light Detection and Ranging
LPS	Leica Photogrammetry Suite
NAU	Northern Arizona University
NED	National Elevation Dataset
RMRS	Rocky Mountain Research Station
RMSE	Root Mean Square Error
SAR	Synthetic Aperture Radar
SRTM	Shuttle Radar Topography Mission
USGS	United States Geological Survey

Appendix 6.2 USGS Camera Calibration Report

USGS Report No. OSL/3490

United States Department of the Interior

U.S. GEOLOGICAL SURVEY
Reston, Virginia 20192

REPORT OF CALIBRATION
of Aerial Mapping Camera

December 08, 2009

Camera type:	Zeiss RMK Top 15*	**Camera serial no.:**	145849
Lens type:	Zeiss Pleogon A3/4	**Lens serial no.:**	145910
Nominal focal Length:	153 mm	**Maximum aperture:**	f/4
		Test aperture:	f/4

Submitted by: Aerial Mapping Company, Inc.
Phoenix, Arizona

Reference:

These measurements were made on Agfa glass plates, 0.19 inch thick, with spectroscopic emulsion type APX Panchromatic, developed in D-19 at 68° F for 3 minutes with continuous agitation. These photographic plates were exposed on a multicollimator camera calibrator using a white light source rated at approximately 5200K.

I. Calibrated Focal Length: 152.994 mm

II. Lens Distortion

Field angle:	7.5°	15°	22.7°	30°	35°	40°
Symmetric radial (μm)	0	0	0	-1	0	1
Decentering tangential (μm)	0	0	1	1	2	3

Symmetric radial distortion		Decentering distortion		Calibrated principal point	
K_0 =	0.3834E-05	P_1 =	-0.1445E-06	x_p =	-0.010 mm
K_1 =	0.1057E-08	P_2 =	-0.6979E-07	y_p =	0.010 mm
K_2 =	-0.9316E-13	P_3 =	0.0000		
K_3 =	0.0000	P_4 =	0.0000		
K_4 =	0.0000				

The values and parameters for Calibrated Focal Length (CFL), Symmetric Radial Distortion (K_0,K_1,K_2,K_3,K_4), Decentering Distortion (P_1,P_2,P_3,P_4), and Calibrated Principal Point [point of symmetry] (x_p,y_p) were determined through a least-squares Simultaneous Multiframe Analytical Calibration (SMAC) adjustment. The x and y-coordinate measurements utilized in the adjustment of the above parameters have a standard deviation (σ) of ±3 microns.

* Equipped with Forward Motion Compensation

III. Lens Resolving Power in cycles/mm

Area-weighted average resolution: 98

Field angle:	0°	7.5°	15°	22.7°	30°	35°	40°
Radial Lines	134	159	113	113	113	95	95
Tangential Lines	134	134	113	95	80	80	80

The resolving power is obtained by photographing a series of test bars and examining the resultant image with appropriate magnification to find the spatial frequency of the finest pattern in which the bars can be counted with reasonable confidence. The series of patterns has spatial frequencies from 5 to 268 cycles/mm in a geometric series having a ratio of the 4th root of 2. Radial lines are parallel to a radius from the center of the field, and tangential lines are perpendicular to a radius.

IV. Filter Parallelism

The two surfaces of the USGS TOP 15 test filter KL-F (60%) No. 142399 and KL-F (36%) filter No. 148625 are within 10 seconds of being parallel. The USGS TOP 15 test filter, in conjunction with the internal "B" filter, was used for the calibration.

V. Shutter Calibration

Indicated Time (sec)	Rise Time (µ sec)	Fall Time (µ sec)	½ Width Time (ms)	Nom. Speed (sec)	Efficiency (%)
1/100	2503	2732	12.99	1/90	87
1/200	1229	1278	6.09	1/190	87
1/300	793	814	4.07	1/280	88
1/400	563	569	2.81	1/410	87
1/500	447	456	2.20	1/520	87

The effective exposure times were determined with the lens at aperature f/4. The method is considered accurate within 3 percent. The technique used is described in International Standard ISO 516:1999(E).

VI. Magazine Platen

The platen mounted in Zeiss T-MC film magazine No. 151625 does not depart from a true plane by more than 13 µm (0.0005 in).

The platen for this film magazine is equipped with an identification marker that will register "151770" in the data strip area for each exposure.

VII. Principal Point and Fiducial Mark Coordinates

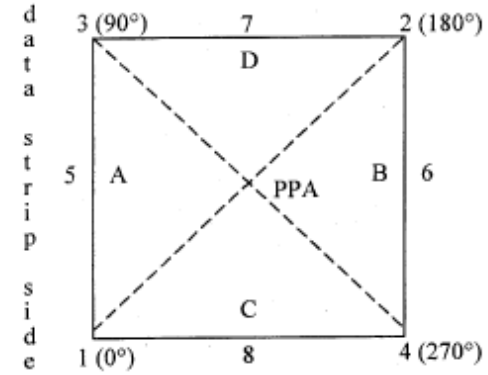

data strip side

Positions of all points are referenced to the principal point of autocollimation (PPA) as origin. The diagram indicates the orientation of the reference points when the camera is viewed from the back, or a contact positive with the emulsion up. The data strip is to the left.

	X coordinate (mm)	Y coordinate (mm)
Indicated principal point, corner fiducials	-0.003	0.010
Indicated principal point, midside fiducials	-0.004	0.006
Principal point of autocollimation (PPA)	0.000	0.000
Calibrated principal point (point of symmetry)	-0.010	0.010
Fiducial Marks		
1	-113.013	-112.996
2	113.004	113.012
3	-112.992	112.994
4	113.008	-112.996
5	-113.002	0.000
6	113.015	0.011
7	0.004	113.007
8	-0.011	-112.999

VIII. Distances Between Fiducial marks

Corner fiducials (diagonals)	1-2:	319.630 mm	3-4:	319.605 mm
Lines joining these markers intersect at an angle of 90° 00' 10"				
Midside fiducials	5-6:	226.017 mm	7-8:	226.006 mm
Lines joining these markers intersect at an angle of 89° 59' 36"				
Corner fiducials (perimeter)	1-3:	225.989 mm	2-3:	225.997 mm
	1-4:	226.021 mm	2-4:	226.007 mm

The Method of measuring these distances is considered accurate within 0.003 mm

Note: For GPS applications, the nominal entrance pupil distance from the focal plane is 254mm with a 10 mm filter thickness. Additional filter thickness will increase entrance pupil distance by 0.34 X added thickness.

IX. Stereomodel Flatness

FMC Magazine No: 151625 **Base/Height ratio:** 0.6

Platen ID: 151770 **Maximum angle of field tested:** 40°

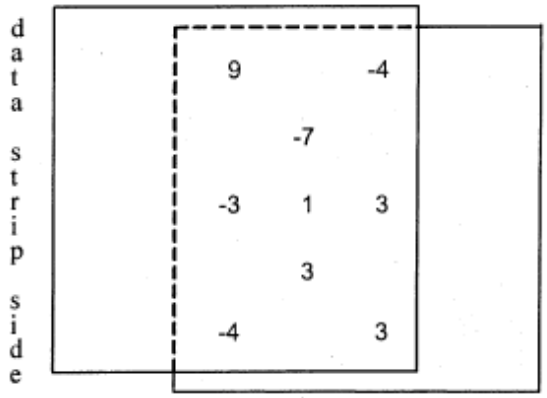

Stereomodel Test Point Array
(values in micrometers)

The values shown on the diagram are the average departures from flatness (at negative scale) for two computer-simulated stereo models. The values are based on comparator measurements on Agfa Avitone P3P copy film made from Kodak 2405 film exposures. These measurements are considered accurate to within 5 µm.

X. System Resolving Power on film in cycles/mm

Area-weighted average resolution: 47 **Film:** Type 2405

Field angle:	0°	7.5°	15°	22.7°	30°	35°	40°
Radial Lines	57	57	48	48	48	48	48
Tangential Lines	57	57	48	48	48	40	40

This aerial mapping camera calibration report supersedes the previously issued USGS Report No. OSL/3276, dated December 5, 2006.

Michael G. Benson
Remote Sensing Technologies Project Manager
Geography Discipline

Appendix 6.3 Exterior orientation associated with the imagery (red triangles represent GCP locations).

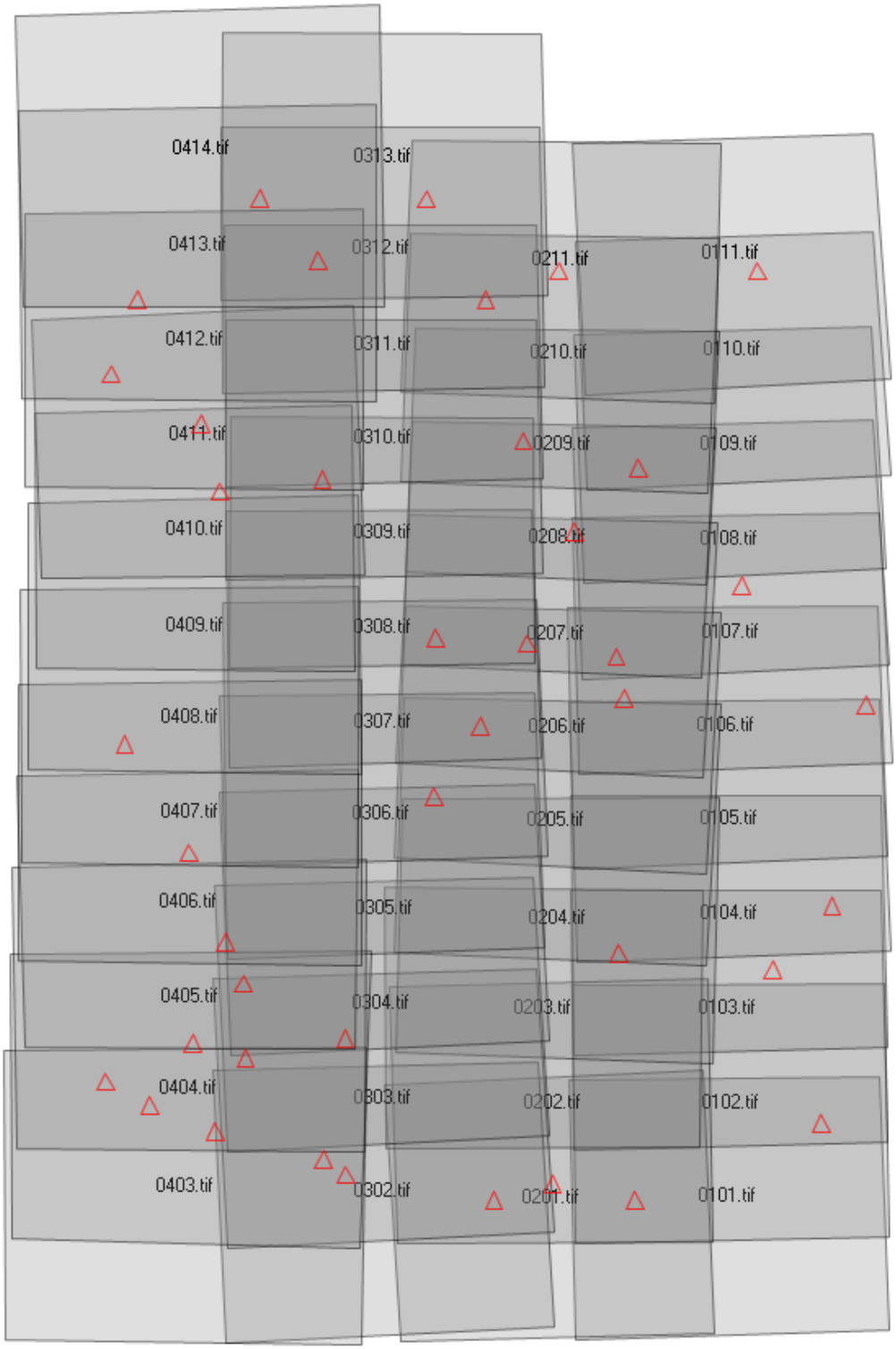

Appendix 6.4 Horizontal and vertical precision associated with the locatable GCPs collected with the DGPS equipment. These precision values ranged from 0.002 m to 0.051 m (horizontal) and 0.004 m to 0.074 m (vertical).

GCP ID	Horizontal Precision (m)	Vertical Precision (m)
x001	0.011	0.022
x002	0.013	0.027
x003	0.005	0.016
x004	0.006	0.008
x005	0.003	0.004
x006	0.022	0.037
x008	0.01	0.017
x009	0.007	0.009
x01	0.018	0.033
x010	0.004	0.012
x011	0.025	0.072
x012	0.006	0.014
x013	0.051	0.074
x02	0.006	0.009
x03	0.008	0.015
x04	0.008	0.015
x041R	0.005	0.015
X044R	0.008	0.012
x045R	0.012	0.024
x05	0.002	0.004
x06	0.003	0.007
GC01	0.003	0.005
GC03	0.002	0.004
GC04	0.004	0.007
GC05	0.005	0.011
GC06	0.01	0.02
GC07	0.004	0.009
1	0.007	0.011
2	0.01	0.021
3	0.009	0.021
4	0.01	0.018
6	0.013	0.021
8	0.01	0.021
9	0.013	0.027
10	0.014	0.021
12	0.015	0.047
13	0.012	0.027
14	0.01	0.019
16	0.023	0.057
17	0.012	0.021
20	0.008	0.012